ProQuest Number: 10183502

LABORATORY STUDIES OF PEROXY RADICAL REACTIONS WITH NO$_X$ SPECIES USING TURBULENT FLOW CHEMICAL IONISATION MASS SPECTROSCOPY

ASAN DEVRIM BACAK

A thesis submitted in partial fulfilment of the
Requirements of The Nottingham Trent
University for the degree of
Doctor of Philosophy

April 2004

Acknowledgments

Okumakta oldugunuz sayfada yazili olan her sey bitirilmis bir surecin tesekkur dilekleri degil, yeni baslayan bir surecin heyecan cigliklaridir. Yurdumuz icten ice kendisini kemirmekte olan egitimsizlik ve gericilik hastaliklarina ragmen gelecege umitle ilerleyebilecek aydin bireyler yetistirme becerisine sahiptir. Buyuk hedef ve cok guzel emellerle kurulan cumhuriyeti korumak ve gelecege guclendirerek tasimak sahsim adina hayatimin en buyuk hedefidir.

Oncelikle o haziran gecesi beni ugurlamak icin Samsun meydanina gelen her bireye hayatimda oynadiklari rolun buyuklugunu anlatamayacagimi soylemek isterim. Dostlarim her birinizin o temiz ve saf kuvveti beni hayatimin her asamasinda destekledi ve kuvvet verdi.

Simdi gelelim o cok uzun isim listesine, tesekkur siralamasini yapmanin en kolay yolunun yilar itibari ile olduguna karar verisimden oturu liste cocuklugumdan baslayacak en bastan listedeki herkese gelisimimdeki katkilarindan dolayi minnettarim.

Umran Akdagcik, Haydar Mohur, Emrah Poyraz ve Bahri Akgul isimlerinizi yazarken gulumsememek elde degil Anadolunun guzel insanlari. herbiri yagiz delikanli, saf, temiz ayrica hayatimin ayni doneminde yollarimizin kesistigi Giresun yoresinin mert cocugu Ahmet Rahman Savas sizlerle gecirdigim her saniyeden inanilmaz tadlar aldim.

Ardindan annemin telefonu ve Samsun gunlerinin baslangici babamin beni ilk adim yurduna birakisini hic unutmayacagim ve insanlar Niyazi Sari, Dincer Esitgin, Dincer Nas, Ercument Uncu, Saim baba, Coskun Dursunoglu, Osman Ucdirhem, Rizeli Atilla, Samsunlu Cumhur ve Artvinli Mete, Veysel Celik, Murat Vargul, Beyhan Akata, Tolga Pala, Serdar Tavas, Mehmet Anik, Alpaslan Ergunay, Sinoplu Bulent, Adananin bagrindan kopup gelen Soner, Sindirgili Memet, Riza Kosef, Bas hekim Ramiz Gokmen ve Doktor Nuray Ogutcu, Ezgin Tan, Ozhan Unverdi, Aykut Sezer ve su an isimleri aklima gelmedigi icin yazamadigim ama beni affedeceklerini bildigim bir cok dostum herbirinize tesekkur ederim bazilarinizla su an gorusemesekte size cok sey borcluyum.

Tabiiki tesekkur edilecek isimler yukaridaki liste ile bitmiyor birde yuksek saygi duyulacak insanlar listesi varki cok yazilasi bu insanlar bir sekilde egitimimde veya yasantimda onemli rol aldilar oncelikle dayim ile baslamaliyim bu listeye. Mehmet Bilgay Akhan dayi buraya senin ayak izlerini takip ederek geldim. Hocalarin hocasi Fevzi Ozkan siz olmadan analiz dersi nasil gecilir Fizik bolumu nasil biterdi bilemiyorum. Teyzelerim Semra ve Mualla ve tabiiki esleri Nihat ve Cengiz. Elmadagdan Semiha teyzeeeee ve Cerkez Beyhan amca, Ipek ve Cengiz Togur birisi ingilizce calistirdi digeri fizik bende Ingilterede Fizik ve Kimya doktoru oldum. Ardindan yine Samsun ve Ayla teyze cok ama cok tesekkurler. Universite hayatima gelince bir kac hocama tesekkur borcluyum Prof. Nazmi Turan Okumusoglu sonsuz sabrinizdan ve bir kis gecesi ofisinizdeki kisa konusmamizdan dolayi; Prof. Ahmet Erdonmez, Prof. Ismet Senel, Prof. Hasan Gumus, Dr. Metin Yavuz, onurlu insan Ali Albay ogrettiklerinizden ve yardimlarinizdan dolayi sonsuz tesekkurler.

Ardindan hayatimin su ana kadarki olan bolumunun son duragi Ingiltere yillarina geliyoruz ki; Kralicenin topraklari yurdumdan insan manzaralarina, yurdumdan cok sahit oldugum topraklardir. Heatfiled yoresinde LSE mezunu donerci Ertan abi ile baslayan manzaralara en son olarak Turk konsoslugunun onunde Erzurumlu Suat eklendi, simdi sadece arada cok onemli olan isimleri hatirlayacagim bazi isimleride burada hatirlamasamda unutmayacagimda, mesela bir senedir Uskup uzeri Londraya gelmekte olan arkadasimizi hala beklemekteyim.

Hakan Altan bir kere daha ayni seyleri yasamam soz konusu olsa yahu o donem birazcikta zor oldu diye hic dusunmezdim seninle lokanta yapmak cok zevkliydi ihtiyar ozelliklede tavanlar. Her ne kadar bu satirlari anlamayacak olsalarda hocam Dr. Carl Percival grup arkadasim Dr. Max Bardwell guzel dostum Dr. Simon Stanley ve Sifu Philip Jones zannimca doktora sureci siz olmadan bu kadar guzel olamazdi ayrica Clifton yoresinin tek cay ikrami olan pizza dukkanin sahibi Ali Ozturk ve kardesi Huseyin Ozturk her birinize cok cok ama cok tesekkurler hayatimin bu gune kadar olan bolumunde ogrendigim onemli derslerden birisi olan dunya kucuktur savina dayanarak tekrar gorusmek umidi ile diyorum ve sabirsizlikla o gunu bekleyecegim hepinize sevgiler.

Son satirlar ise anneme babama ve kardesime ait, sonsuz sabriniz, destekleriniz ve bitmez sevginiz hayatta elde ettigim butun basarilarin en buyuk sebebidir ve bu tez babama ve anneme ithaf edilmistir.

Ve tabiiki birtanecik sevgilim Celine Grand hani her basarili erkegin arkasinda cok buyuk bir kadin vardirya iste bu tezin arkasindaki kadin Celinedir tesekkur ederim askim.

Asan BACAK

bir kivilcim düser önce , büyür yavas yavas
bir bakarsin volkan olmus, yanmissin arkadas
dolduramaz boslugunu ne baci ne kardas
bu en güzel,bu en sicak duygudur arkadas
ortak olmak her sevince,her derde, kedere
ve yürümek ömür boyu, beraberce, el-ele
olmasin hiç o ta içten gülen gözlerde yas
birgün gelip ayrilsak bile seninle arkadas...

evet arkadas kim oldugumu, ne oldugumu,
nereden gelip - nereye gittigimi sen ögrettin bana
elimden tutup karanliktan aydinliga sen çikardin
bana yürümeyi ögrettin yeniden el-ele ve daima ileriye!
birgün; birgün birbirimizden ayri düssek bile biliyorum
hiçbir zaman ayri degil yollarimiz; ve ayni yolda yürüdükçe
gün gelir ellerimiz yine dostça birlesir ayrilsak bile kopamayiz
Olmayacak o ta içten gülen gözlerde yas
Birgün gelip ayrilsak bile seninle arkadas

Susarlar sesini bogmak isterler
Yarimdir kiriktir sirça yüregim
çiglik çigliga yar geceler
Kardesin duymaz eloglu duyar

Yikilir engeller yürür gidersin
yüregin tasiyip götürür seni
Nice selden sonra bundan ötede
Kardesin duymaz eloglu duyar

üzülme bunlari duydugun zaman
ümidi kesipte incinme sakin
Aç yüregini bir merhabaya
Kardesin duymaz eloglu duyar.

Abstract

LABORATORY STUDIES OF PEROXY RADICAL REACTIONS WITH NO$_X$ SPECIES USING TURBULENT FLOW CHEMICAL IONISATION MASS SPECTROSCOPY

by

Asan Devrim BACAK

Nottingham Trent University   Nottingham 2004

Submitted for the degree of Ph.D.

The importance of peroxy radical reactions in the upper troposphere and lower stratosphere (UTLS) region are well known. The reaction between peroxy radicals and NO$_x$ species is a notable example, influencing as it does ozone (O$_3$) concentrations within this region. Previous kinetic studies have been performed over small ranges of temperature and pressure and have thus been very limited. The result of these studies is a wealth of data that needs extrapolation to UTLS region parameters before it can be compared accurately with atmospheric conditions.

The main target of this work was the development of a unique analytical tool for the study of peroxy radical reactions, a chemical ionisation mass spectrometer (CIMS) turbulent flow system, capable of the detection and identification of both the reactant and product species. The system was designed and became operational. Experimental work has the focused on laboratory studies of reaction kinetics, data reported in this work representing the reactions of hydroperoxy and methylperoxy radical reactions with NO$_2$ and the reaction between HO$_2$ and NO over wide temperature and pressure ranges (190 − 298 K and 70 − 760 Torr).

The reaction of the hydro peroxy radical with NO was studied using the TF-CIMS system over a temperature range of 190 − 298 K at three different pressures 75, 100 and 200 Torr. The rate coefficient was found to display a negative temperature dependence, determined with Arrhenius type analysis to yield the expression $k = (3.98^{+0.29}_{-0.27}) \times 10^{-12} \exp{[(223 \pm 16.5) / \text{T}]}$ cm^3 molecules^{-1} s^{-1}. The rate coefficient was determined as a function of pressure, however, there was no effect of pressure on the measured rate coefficient. The product study and atmospheric implications of this reaction are discussed.

The reaction of the hydroperoxy radical with NO$_2$ was also studied using the same system; at three different temperatures 298, 223 and 200 K over a pressure range of 150 − 700 Torr. The rate coefficient was found to be pressure dependent. For the reaction, the temperature dependent low-pressure rate coefficient can be described by the equation $k_0 \text{(T)} = (1.8 \pm 0.3) \times 10^{-31} \text{(T/300)}^{-(0.2 \pm 0.3)}$ cm^6 molecule^{-2} s^{-1} and the temperature dependent high pressure rate coefficient can be described by the equation $k_\infty \text{(T)} = (4.7 \pm 1.0) \times 10^{-12} \text{(T/300)}^{-(0.5 \pm 0.3)}$ cm^3 molecule^{-1} s^{-1} The atmospheric implications of this reaction are also discussed.

The reaction of the methylperoxy radical with NO$_2$ was also examined with the TF-CIMS system, at two different temperatures 298, 223 K over a pressure range of 100 − 700 Torr. The rate coefficient found to be pressure dependent. For the reaction, the temperature dependent low-pressure rate coefficient can be described by the equation $k_0 \text{(T)} = (1.5 \pm 0.8) \times 10^{-30} \text{(T/300)}^{-(4.0 \pm 2.0)}$ cm^6 molecule^{-2} s^{-1} and the temperature dependent high pressure rate coefficient can be described by the equation $k_\infty \text{(T)} = (6.5 \pm 3.2) \times 10^{-12} \text{(T/300)}^{-(2.0 \pm 2.0)}$ cm^3 molecule^{-1} s^{-1} The results described in this thesis are concordant with previous recommendations.

Chapter 1

Introduction

Chapter 2

Flow tube theory and experimental set – up

Chapter 3

Kinetics of the Reaction Between HO_2 and NO

Chapter 4

Kinetics of the Reaction Between HO_2 and NO_2

Chapter 5

Kinetics of the Reaction Between CH_3O_2 and NO_2

Chapter 6

Conclusions and Future Work

Chapter 1

Introduction

1.1 Evolution of the Earth's Atmosphere

The Earth was formed from a cloud of dust consisting of debris remaining from a huge explosion known as the big bang, which occurred 15 billion years ago. Around 1 million years after the big bang it was cool enough for the first atoms to form (hydrogen atom is the primordial element) and after a further billion years the atoms began to congeal to form the first galaxies. The approximate age of the earth is 4.5 – 5 billion years. The evolution of the atmosphere can be divided into 4 stages, which span this time period.

>4.5 billion years ago

The earth was still hot. Gravitational fields are weak and the primary atmosphere was lost into space.

~4.5 billion years ago

The outgassing of volatile gases, as a result of volcanic and meteoric action, forms a thin atmosphere. The atmosphere had a similar content to current volcanic eruptions, consisting of CO_2, H_2O, SO_2 and N_2. At this point there is no free oxygen. This CO_2-rich atmosphere was more dense and warmer than the current atmosphere, even though the solar irradiance was less than the modern day.

<u>~4 billion years ago</u>

A cooling of the planet lead to water condensing and the consequent formation of clouds, rain and eventually oceans. This resulted in a reduction of atmospheric H_2O and CO_2 and N_2-rich atmosphere.

<u>~3.5-2.5 billion years ago</u>

An atmosphere similar in composition to that of the "modern day" atmosphere was formed during this period. Existence of life forms leads to photosynthesis and subsequent removal of CO_2 and release of O_2. As a result O_2 becomes the atmosphere's second most dominant gas. The interaction of UV (ultra violet) light and O_2 molecules develops an Ozone layer and which provides protection from UV radiation and allows life to flourish.

1.2 Composition of the Earth's Atmosphere

The atmosphere we breathe is a relatively stable mixture of several hundred types of gases of different origin. This gaseous envelope surrounds the planet and revolves with it. It has a mass of about 5.15×10^{15} tons and is held to the planet by gravitational attraction. The majority of atmospheric research focuses on the region < 80 km where the atmospheric composition is relatively constant. At altitudes > 80 km, the composition of the atmosphere varies with height. The focus of this work will be the section of the atmosphere < 80 km.

Within this region, air is comprised mainly of nitrogen (N_2) ~ 78.08 %, oxygen (O_2) ~ 20.95 % and argon (Ar) ~ 0.93 %. The composition of these gases makes 99.93% of the atmosphere but these gases are generally not the focus of significant research. More important are the interactions of the trace gases such as water vapour (H_2O) < 0.25%, carbon dioxide (CO_2) ~ 0.036% (360 ppm.), methane (CH_4) ~ 0.00015% (1.5 ppm.), ozone (O_3) ~ 0.01% (100 ppm.) and aerosols where ppm = parts per million and ppb = part per billion.

1.3 Structure of the Earth's Atmosphere

The pressure of the atmosphere varies with height, z, above the Earth's surface. The pressure of the terrestrial atmosphere alters in an exponential manner as described by Equation 1.1 Wayne (2000).

$$P \quad = \quad P_0 \exp [-mgz/kT] \quad\quad\quad \text{E.1.1}$$

Where P_0 is the pressure at ground level, g is the gravitational acceleration and m is the relative molecular mass of the gas. There is no gravitational separation of the individual components of the Earth's atmosphere below the tropopause as a result of mixing through the action of molecular diffusion being less important than mixing through eddy diffusion processes such as convection.

The temperature of the atmosphere does not vary so smoothly with altitude, as it is affected by the absorption and re-emission of solar radiation by atmospheric species. The Earth's effective temperature, T_e, can be calculated, assuming that it is a black body radiator obeying the Stefan-Boltsmann law:

$$E \qquad = \qquad \sigma T_e^4 \qquad\qquad\qquad \text{E.1.2}$$

where E is the radiated flux per unit area and σ is the Stefan - Boltsmann constant (5.67×10^{-8} $Wm^{-2}K^{-4}$). The total emitting area of the Earth is $4\pi R_e^2$ (R_e is the radius of the Earth), whereas the area of the absorbing disc presented to the solar flux is πR_e^2 assuming that the Earth's atmosphere is totally transparent to incoming and outgoing radiation (Wayne, 2000)

$$4\pi R_e^2 \sigma T_e^4 \qquad = \qquad \pi R_e^2 (1-A) F_s \qquad\qquad \text{E.1.3}$$

where A is the albedo (reflectivity) of the Earth and F_s is the solar flux (the total amount of radiation of all wave lengths intercepted in unit time by unit surface area) at the edge of the Earth's atmosphere. For the Earth A $\approx$ 0.29, Fs $\approx$ 1368 Wm^{-2} and from Equation 1.3 the Earth's temperature (T_e) is calculated to be 256 K. This is 32 K lower than the actual temperature of the Earth. The reason for this discrepancy is largely due to the fact that the Earth's atmosphere is not transparent to radiation. The wavelengths of the radiation emitted by the Earth and the Sun differ, as they produce electromagnetic radiation associated with black body radiators with temperatures of 256 K and 5780 K respectively.

Emission from the Sun is centred at 0.5 μm (visible) while the emitted radiation from the Earth is centred at 15 μm (infrared radiation). The Earth's atmosphere is partially transparent to radiation from the Sun, except for wavelengths less than 310 nm, which are absorbed by the ozone layer, as shown in Figure 1.1.
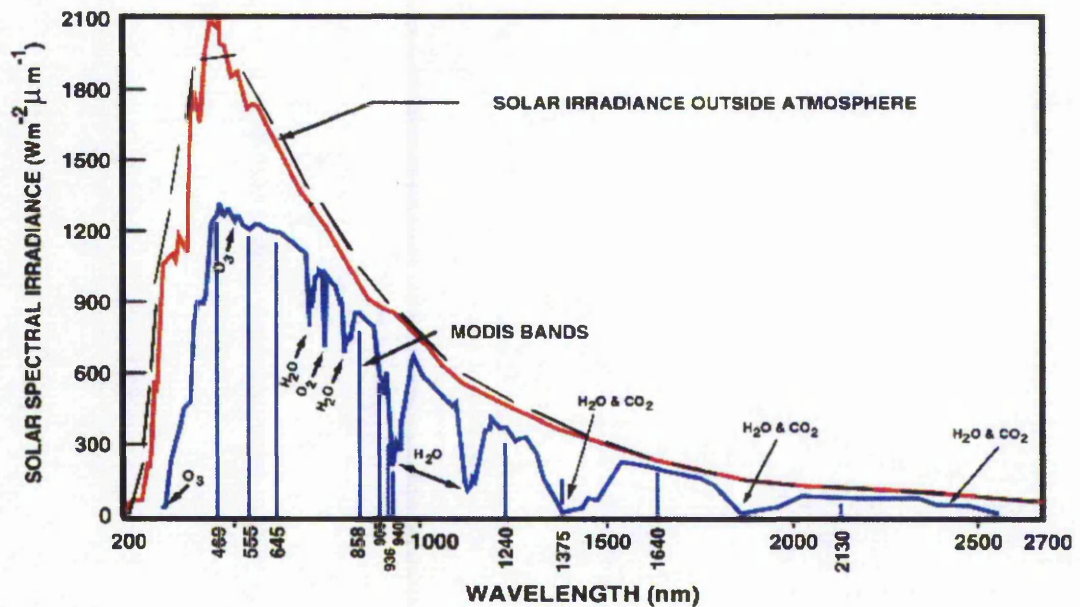
Figure 1.1: Solar flux outside the atmosphere and at the sea level. The emission of a black body at 5800 K is represented by dashed line (adapted from Wayne, 2000).

The infrared radiation emitted from the Earth is absorbed in the lower atmosphere, particularly by water and carbon dioxide, as shown in Figure 1.1 and Figure 1.2, re-emitted and then immediately absorbed again by neighbouring molecules, so in effect trapping the radiation. At higher altitudes there are fewer absorbing species and the re-emitted radiation has greater chance of escaping into space. This leads to a net warming effect of the Earth's surface, which is known as the "greenhouse effect".
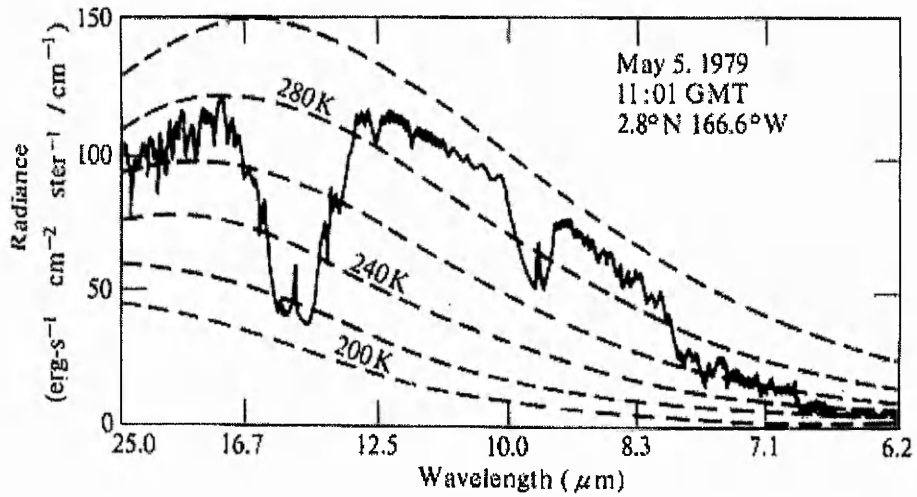
Figure 1.2: Spectrum of infrared emission escaping to space, as observed from outside the Earth's Atmosphere. Dashed lines represent the spectrum expected from a black body at different temperatures (taken from Wayne, 2000).

The temperature profile of the Earth's atmosphere, shown in Figure 1.3, divides it into distinct regions. The lowest region of the atmosphere is called the troposphere and contains $80 - 90\%$ of the mass of the atmosphere. The temperature drop with altitude can be explained in terms of a radiative transfer model. In principle, one then expects the hot air to rise. The effect of the heating is to reduce the temperature gradient at the Earth's surface. However, as hot air rises it does work on the surroundings and consequently cools down. If it were to cool less than its surroundings, the air would not rise and the system would be conventionally stable (the troposphere is unstable yet the stratosphere is stable).
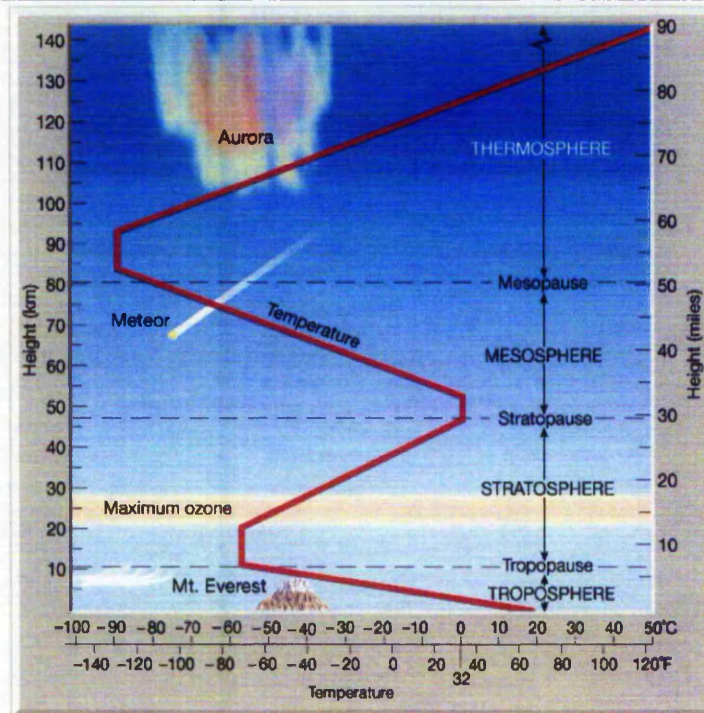
Figure 1.3: Temperature profile of the Earth's atmosphere (taken from Lutgens and Tarbuck, 2001).

The criterium used to separate stable and unstable atmosphere is the adiabatic lapse rate. Vertical mixing within the troposphere occurs relatively quickly (~ one day), but horizontal mixing is slow taking approximately one year for an entire hemisphere. The boundary between the troposphere and the stratosphere (the tropopause) is indicated by a change in the temperature gradient. The temperature of the tropopause is 220 K and acts as a cold trap causing the observed dryness of the air above it. The stratosphere has typically $2 - 3$ ppm of water while the troposphere has in the order of a few thousand parts per million. Latitude and meteorological conditions vary, but for example, the typical tropopause height is 15 km.

In the stratosphere the temperature rises with altitude, due to the photolysis of molecular oxygen, which forms ozone.

$$O_2 \quad + \quad h\nu\ (\lambda = 240nm) \quad \rightarrow \quad O \quad + \quad O \qquad\qquad R.1.1$$

$$O \quad + \quad O_2 \quad + \quad M \quad \rightarrow \quad O_3 \quad + \quad M \qquad\qquad R.1.2$$
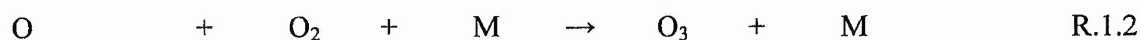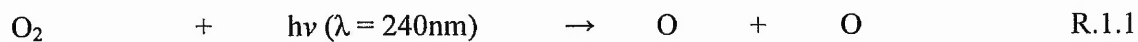
The photolysis of both O_2 and O_3 generates heat, which leads to a rise in temperature. As a consequence of the reversal of the temperature gradient, warmer air lies on top of colder air and so the air mass is stable with respect to vertical mixing. At 50 km the temperature of the atmosphere starts to fall with altitude. The point at which temperature starts to fall is called the stratopause. The region above it is called the mesosphere. Eventually the atmosphere becomes so thin that the collisional frequency between gaseous species is so small that all the energy is not equilibrated between all the available degrees of freedom. As a consequence the translational temperature exceeds that of rotational and vibrational temperatures resulting in a temperature rise again. This region is called the thermosphere and the boundary between the mesosphere and the thermosphere is called the mesopause.

1.4 Atmospheric Circulation

Differences in air pressure are a major cause of atmospheric circulation. Because heat excites the movement of atoms, warm temperatures cause air expansion. Since those molecules now occupy a larger space, the pressure that their weight exerts is decreased. Air from surrounding high-pressure areas is pushed toward the low-pressure areas, creating circulation.

This process causes a major pattern of global atmospheric movement known as meridional circulation. In this form of convection, or vertical air movement, heated equatorial air rises and travels through the upper atmosphere toward higher latitudes. Air just above the equator heads towards the North Pole and air just below the equator moves southward. This air movement fills the gap created where increased air pressure pushes down cold air. The cold air moves along the surface back toward the equator replacing the air masses that rise there. Wind flows and atmospheric convection cells around the globe are shown in Figure 1.4.

Another influence on atmospheric circulation is the Coriolis force. Because of the Earth's rotation, large-scale wind currents move in the direction of this axial spin around low-pressure areas. Wind rotates counter clockwise in the Northern Hemisphere and clockwise in the Southern Hemisphere.

Just as the Earth's rotation affects airflow, so too does its surface. In the phenomenon of orographic lifting, elevated topographic features such as mountain ranges lift air as it moves up their surface.
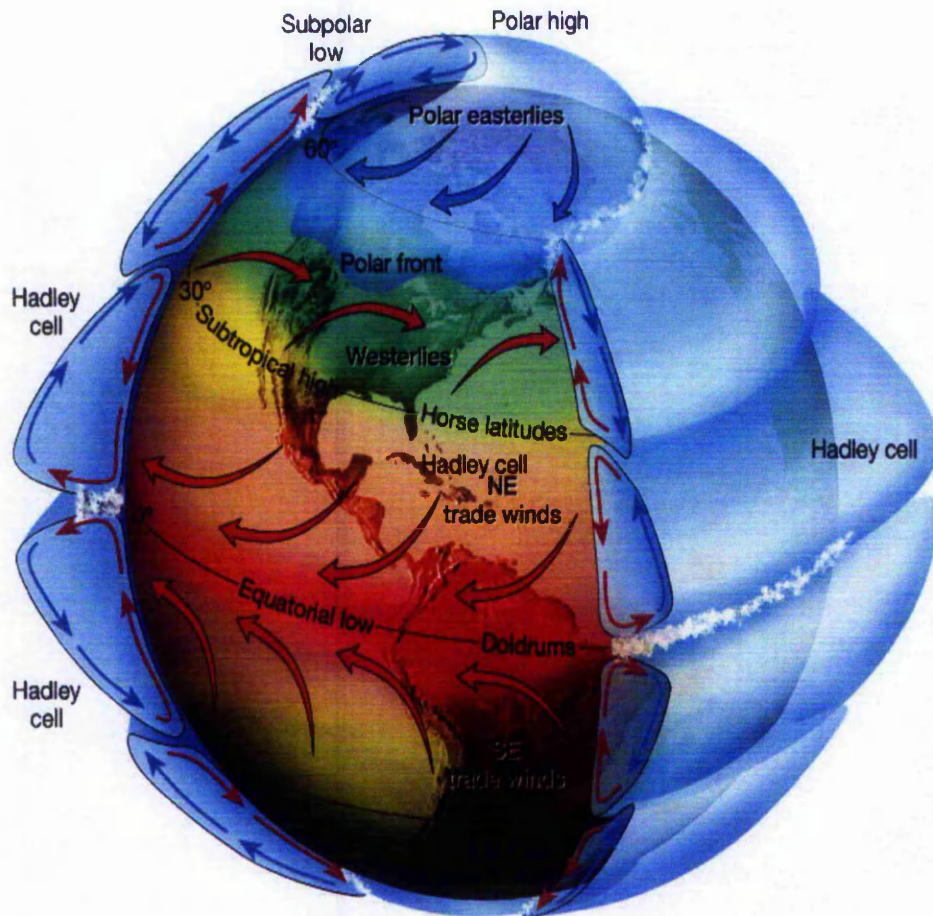
Figure 1.4: Wind flow around the globe and three-cell model of atmospheric convection in a rotating Earth. The Coriolis force causes the deflections of the winds within each cell (taken from Lutgens and Tarbuck, 2001).

As a consequence of all these phenomena, air can cross between the troposphere and stratosphere through the tropopause. The term Stratospheric-Tropospheric Exchange (STE), refers to the transport of material across the tropopause. STE has direct implications on the distribution of atmospheric ozone, in particular the decrease of lower stratospheric ozone and the increase of tropospheric ozone. STE also impacts on the distribution of aircraft emissions and the vertical structure of aerosols and greenhouse gases.

The transport of anthropogenic gases, like chlorofluorocarbons, from the troposphere into the stratosphere affects the chemical balance in both regions and provides the catalysts necessary for stratospheric ozone destruction. Stratospheric-tropospheric exchange also controls the rate of transport between source and sink regions for both tropospheric and stratospheric source gases. A consequence of this is the long pause time between the release of tropospheric trace gases and stratospheric ozone reduction.

One of the most important mechanisms for STE is a tropopause-folding event. A stratospheric intrusion of air that sinks into the baroclinic zone beneath the upper tropospheric jet stream is known as a tropopause fold. as shown in Figure 1.5. Tropopause folds are the dominant and most efficient form of STE in the middle latitudes. Folds usually occur off the western flank of cut-off low systems. Clean, dry stratospheric air, rich in ozone is transported downward to tropospheric levels. Observations of the circulation near folding events reveal that tropospheric air is being advected upwards as well (Lutgens and Tarbuck, 2001).
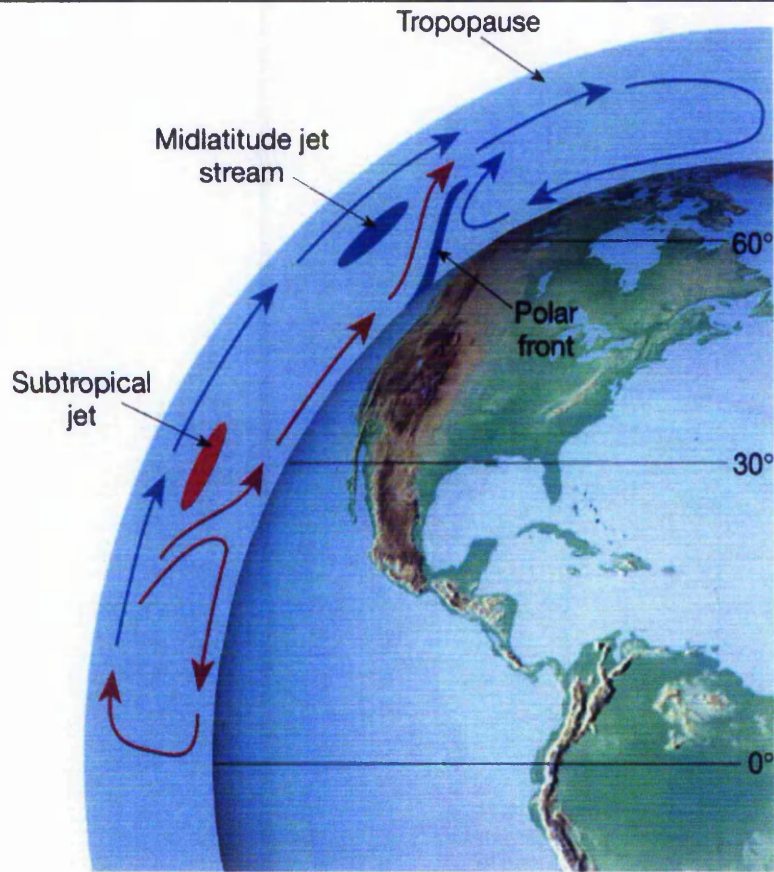
Figure 1.5: A schematic diagram of general meridional circulation (taken from Lutgens and Tarbuck, 2001).

This tropospheric air contains large amounts of water vapour, carbon monoxide and aerosols. However the extent of the contribution to tropospheric ozone budget by STE is hotly debated (Penkett, 1995; Cox, 1988; and Madronich and Hess, 1994).

1.5 Daytime Chemistry in the Clean Troposphere

The hydroxyl (OH) and nitrate (NO_3) radicals and O_3 are the main tropospheric oxidants. They "cleanse" the air by initiating oxidation chain reactions that lead to the formation of secondary pollutants that are eventually removed from the atmosphere. The homogeneous daytime chemistry is dominated by the hydroxyl radical despite its relatively low concentration of approximately 10^6 molecule cm^{-3} (Dubey *et al.*, 1996). The most important source of OH is from the photolysis of O_3.

$$O_3 \quad + \quad h\nu \, (\lambda < 320 \, nm) \rightarrow \quad O \, (^1D) \quad + \quad O_2 \, (^1\Delta_g) \qquad \text{R.1.3}$$

$$O \, (^1D) \quad + \quad H_2O \quad \rightarrow \quad OH \quad + \quad OH \qquad \text{R.1.4}$$
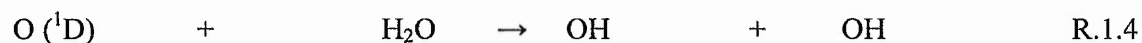
H_2O is a minor component of the atmosphere so reaction (1.4) has a minor impact on O (^1D) atoms destruction compared to physical quenching.

$$O \, (^1D) \quad + \quad M \quad \rightarrow \quad O \, (^3P) \quad + \quad M \qquad \text{R.1.5}$$

$M = N_2, O_2$.

However, all ground state O (^{3}P) atoms generated by reaction (1.5) will regenerate ozone *via* reaction (1.2). So this chain reaction does not destroy odd oxygen (the sum of O_3 and O (^{3}P) and O (^{1}D)) but simply recycles the atomic oxygen and alters the mass balance of odd oxygen. Therefore, the production of OH does depend on relative rates of reaction (1.3) and reaction (1.5).

Other sources of OH radicals are the photolysis of HONO and indirectly the photolysis of HCHO as shown in reactions (1.6 and 1.7).

$$HONO \quad + \quad h\nu\,(\lambda < 390\ nm) \quad \rightarrow \quad OH \quad + \quad NO \qquad R.1.6$$

$$HCHO \quad + \quad h\nu\,(\lambda < 340\ nm) \quad \rightarrow \quad H \quad + \quad HCO \qquad R.1.7$$
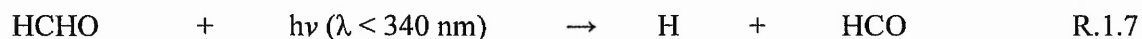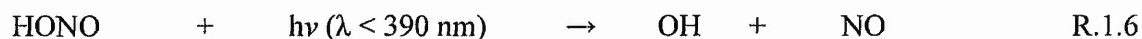
HONO is produced in the atmosphere *via* the termolecular reaction of OH with NO, as shown in reaction (1.8).

$$OH \quad + \quad NO \quad + \quad M \quad \rightarrow \quad HONO \quad + \quad M \qquad R1.8$$
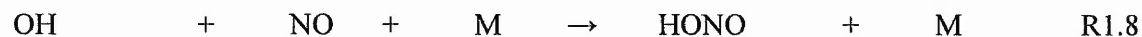
If there are no other sources of HONO, reaction (1.6) does not effect the overall net production of OH. It can be seen that the production of OH is photo-chemically driven and the levels of OH are expected to drop below the minimum detectable limit of 10^5 molecule cm^{-3} at night (Wayne, 2000).

The sinks of the hydroxyl radical differ according to the ambient air quality, which in turn depends on the geographical location (i.e. rural, urban or coastal) over which the air is situated.

The remote rural region is the simplest and best describes the action of OH chemistry on trace species within the troposphere. The remote rural areas have much lower hydrocarbon concentrations, with the exceptions of methane, CFCs and halomethanes. The two main reactions of the OH radical in this unpolluted area are reaction with methane or CO.

$$OH \quad + \quad CH_4 \quad \rightarrow \quad CH_3 \quad + \quad H_2O \quad\quad\quad R.1.9$$

$$OH \quad + \quad CO \quad \rightarrow \quad CO_2 \quad + \quad H \quad\quad\quad R.1.10$$
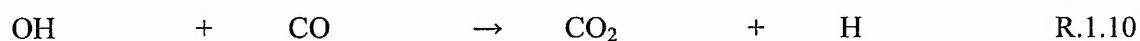
Roughly 70% of the OH reacts with CO, and 30% with CH_4, in the unpolluted atmosphere. Reaction (1.9) is the start of an important oxidation pathway (Wayne, 2000), which leads to tropospheric breakdown of volatile organic compounds (VOC's). Reactions (1.9 and 1.10) produce highly reactive species, which react with oxygen to yield peroxy species.

$$CH_3 \quad + \quad O_2 \quad + \quad M \quad \rightarrow \quad CH_3O_2 \quad + \quad M \quad\quad\quad R.1.11$$

$$H \quad + \quad O_2 \quad + \quad M \quad \rightarrow \quad HO_2 \quad + \quad M \quad\quad\quad R.1.12$$

In rural areas, where NO_x species are low, the peroxy radicals produced *via* reaction (1.11) and reaction (1.12) are destroyed mainly through self or cross reactions as shown in reactions (1.13 and 1.14).

$$HO_2 \quad + \quad HO_2 \quad \rightarrow \quad HOOH \quad + \quad O_2 \quad\quad\quad R.1.13$$

$$CH_3O_2 \quad + \quad HO_2 \quad \rightarrow \quad CH_3OOH \quad + \quad O_2 \quad\quad\quad R.1.14$$

Further reactions or photolysis of these products can lead to the formation of radical species, which can re-enter the oxidation chain. However, the hydroperoxides produced in reactions (1.13 and 1.14), while being labile with respect to photolysis or reaction with the hydroxyl radical, are also very soluble in water. Thus a major loss process for these species is by incorporation into cloud droplets where upon they can be rained out (Finalyson-Pitts and Pitts, 1986).

1.5.1 Daytime Chemistry in the Polluted Troposphere

NO_x represents the oxides of nitrogen, which are namely nitrogen monoxide (NO) or nitrogen dioxide (NO_2). The main source of NO_x in the atmosphere is from anthropogenic emission, a ratio of roughly 90% NO and 10% NO_2 is emitted from the high temperature combustion process from industrial sources, car or plane exhausts. Natural sources of NO_x include forest fires or lightning. When concentrations of NO_x in the troposphere become higher than a threshold concentration of $\sim 3 \times 10^{11}$ molecules^{-1} cm^3, alternative reactive pathways to reactions (1.13 and 1.14) become available.

NO reacts rapidly with the HO_2 and the methyl peroxy radical CH_3O_2 to form NO_2, as shown in reactions (1.15 and 1.16).

$$HO_2 \quad + \quad NO \quad \rightarrow \quad OH \quad + \quad NO_2 \qquad R.1.15$$

$$CH_3O_2 \quad + \quad NO \quad \rightarrow \quad CH_3O \quad + \quad NO_2 \qquad R.1.16$$
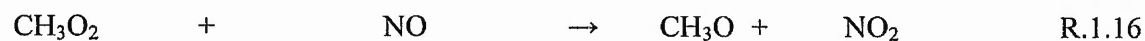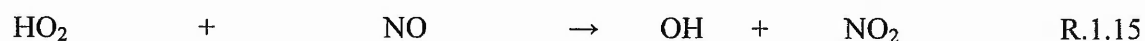
The formation of NO_2 from these reactions potentially results in the formation of ozone through photolysis of the NO_2 molecule as shown in reaction (1.17)

$$NO_2 \quad + \quad h\nu \, (\lambda < 410 \, nm) \quad \rightarrow \quad NO \quad + \quad O \qquad R.1.17$$
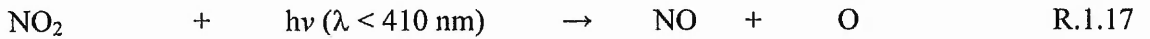
The atomic oxygen produced as a result of reaction (1.17) can react rapidly with molecular oxygen to form ozone, as shown in reaction (1.2). The photolysis of NO_2 is the only known *in situ* source of ozone within the troposphere. So as long as NO_x is present in the troposphere in high enough concentrations, ozone is produced *via* cyclic reactions involving NO and peroxy radicals (RO_2 where R = organic hydrocarbon) and the oxidising potential of the atmosphere increase. A summary of the daytime tropospheric reactions is shown in Figure 1.6.
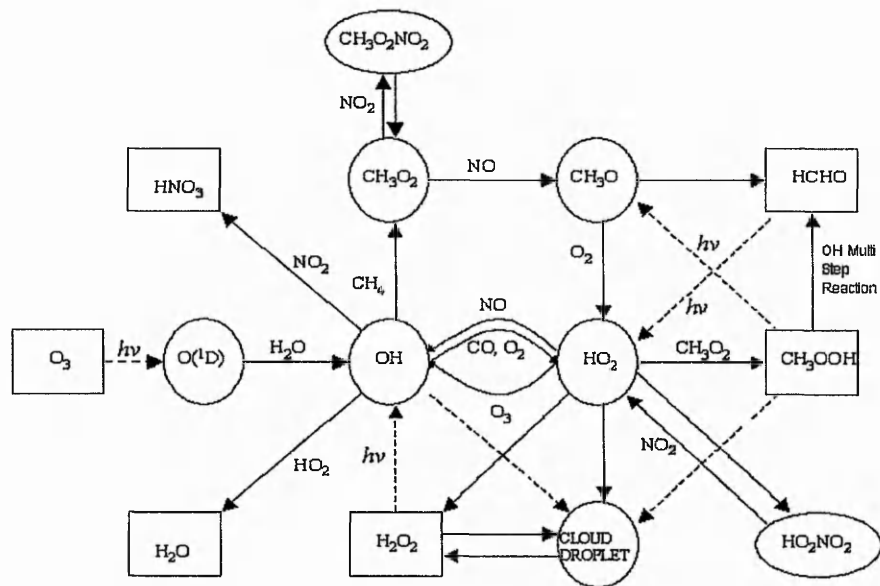
Figure 1.6: A schematic diagram of the chemistry of the daytime troposphere (taken from Wayne, 2000).

1.6 The Influence of VOC's and NO_x on O_3 Production

The tropospheric formation of ozone is almost always initiated by the reaction of various VOCs or CO with the OH radical, as shown in reaction (1.18) and reaction (1.19). This is followed by the conversion of NO to NO_2 (through reaction with HO_2 or RO_2 radicals), *via* the reaction (1.20) and reaction (1.15) (which also regenerates OH). NO_2 is then photolysed to generate atomic oxygen, which combines with O_2 to create O_3 as shown in reactions (1.17 and 1.2).

$$VOC \quad + \quad OH \quad \xrightarrow{[O_2]} \quad RO_2 \quad + \quad H_2O \qquad\qquad R.1.18$$

$$CO \quad + \quad OH \quad \xrightarrow{[O_2]} \quad HO_2 \quad + \quad CO_2 \qquad\qquad R.1.19$$

$$RO_2 \quad + \quad NO \quad \xrightarrow{[O_2]} \quad VOC_{secondary} \; + HO_2 + \quad NO_2 \qquad R.1.20$$

$$HO_2 \quad + \quad NO \quad \rightarrow \quad OH \quad + \quad NO_2 \qquad\qquad R.1.15$$

$$NO_2 \quad + \quad h\nu \quad \rightarrow \quad NO \quad + \quad O \qquad\qquad R.1.17$$

$$O \quad + \quad O_2 \quad + \quad M \quad \rightarrow \quad O_3 \quad + \quad M \qquad\qquad R.1.2$$

The reaction cycle is initiated by the reaction of OH reaction (1.18) and the subsequent reactions of HO_2 and RO_2 leading to the formation of NO_2 reaction (1.15) and reaction (1.20). Therefore, ozone chemistry is strongly dependent on the levels of HO_x (the sum of OH and HO_2) and the levels of peroxy radicals (RO_2). The ozone production rates depend on the relative source and sink strengths of HO_x and RO_2. Sources of HO_x and RO_2 are not just confined to the oxidation scheme initiated by reaction with OH but also include photolysis, e.g. photolysis of ozone, formaldehyde, and other secondary VOCs.

$$O_3 \quad + \quad h\nu \quad \xrightarrow{[H_2O]} \quad 2OH \quad + \quad O_2 \qquad \text{R.1.21}$$

$$HCHO \quad + \quad h\nu \quad \xrightarrow{[2O_2]} \quad 2HO_2 \quad + \quad CO \qquad \text{R.1.22}$$
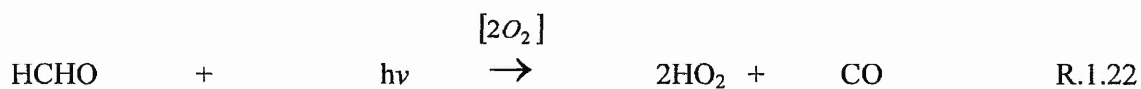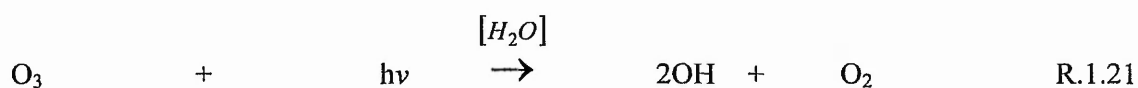
Radical sinks include formation of hydrogen peroxide reaction (1.13) and organic peroxides reaction (1.14), formation of nitric acid reaction (1.23) and the formation of peroxy radical nitrates reaction (1.24).

$$HO_2 \quad + \quad HO_2 \quad \longrightarrow \quad HOOH \quad + \quad O_2 \qquad \text{R.1.13}$$

$$CH_3O_2 \quad + \quad HO_2 \quad \longrightarrow \quad CH_3OOH \quad + \quad O_2 \qquad \text{R.1.14}$$

$$OH \quad + \quad NO_2 \quad + \quad M \quad \longrightarrow \quad HNO_3 \quad + \quad M \qquad \text{R.1.23}$$

$$RO_2 \quad + \quad NO_2 \quad + \quad M \quad \rightleftharpoons \quad RO_2NO_2 \quad + \quad M \qquad \text{R.1.24}$$

The production of ozone can be split into distinct regimes, dependent on the levels on NO_x and VOCs. A NO_x-sensitive regime occurs when peroxides formed *via* reaction (1.13) and reaction (1.14) represents the dominant radical sink. In this case, ambient concentrations of HO_2 and RO_2 radicals will be determined by the balance between radical sources reaction (1.18) and reaction (1.22) and the radical sink peroxide-forming reactions reaction (1.13) and reaction (1.14). As the rate of ozone formation is determined by the reaction of HO_2 and RO_2 with NO reaction (1.20) and reaction (1.15), increasing NO_x will increase O_3 production.

A NO_x-saturated (VOC-sensitive) regime occurs when nitric acid reaction (1.23) represents the dominant radical sink. In this case, ambient the balance between radical sources will determine the concentrations of OH reaction (1.21) and reaction (1.22) and the reaction of OH with NO_2 reaction (1.23). Under NO_x saturated conditions, the rate of ozone formation is determined by the rate of the reaction of VOC and CO with OH reaction (1.18) and reaction (1.19) and thus increases with increasing VOCs. Figure 1.7 shows a typical O_3 isopleth and also the relationship between NO_x and VOCs levels on tropospheric ozone production.

In addition to the relative concentrations of NO_x and VOCs, the composition of the VOCs is important, as the rate of ozone production is dependent on the oxidation of the VOC and will therefore be dependent on the reactivity of that compound. For example, isoprene (C_5H_8) drives the production cycle of ozone approximately 10000 times faster than methane (Atkinson, 2000). There are thousands of examples of naturally emitted VOCs, most are

simple hydrocarbons but there are smaller quantities of partially oxidised VOCs such as alcohols, ketones and acids. They vary from compounds such as ethane (C_2H_6) to complex terpenes such as camphor ($C_{10}H_{16}$). The diversity and complexity of VOCs makes a detailed explanation of their chemistry far beyond the scope of this thesis.
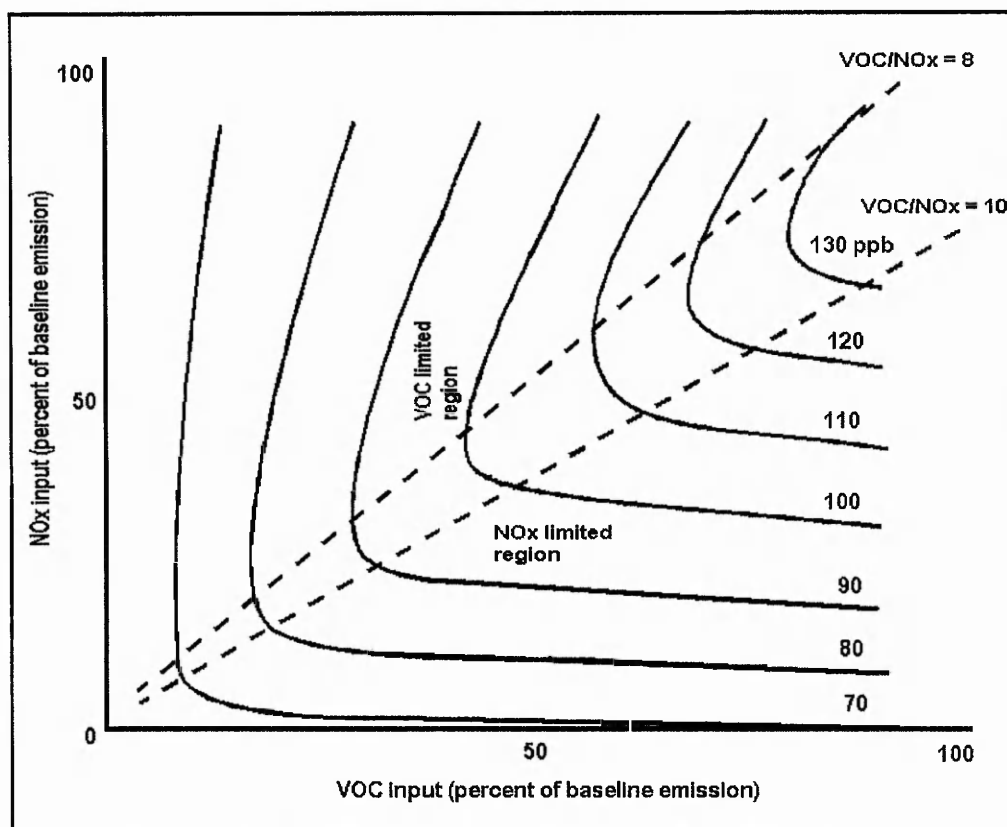
Figure 1.7: A Schematic diagram of the ozone isopleth (EKMA), illustrating the relationship between the initial concentrations of VOC and NO_X and the resulting maximum ozone concentration (Taken from Finalyson-Pitts, B.J. and Pitts, J.N., 1986)

1.7 Formation of PAN

Tropospheric NO_x is rapidly removed *via* the loss process shown in reaction (1.23) unless stored in a reservoir species. One of the most stable reservoir species for NO_x is peroxyacetylnitrate (PAN). PAN can extend the lifetime of NO_x within the atmosphere and provide a source of NO_x where no others are present such as in remote or rural areas. The oxidation of CH_3CHO leads to the formation of PAN by the reactions

$$CH_3CHO \quad + \quad OH \quad \rightarrow \quad CH_3CO \quad + \quad H_2O \qquad R.1.25$$

$$CH_3CO \quad + \quad O_2 \quad + \quad M \quad \rightarrow \quad CH_3COO_2 \quad + \quad M \qquad R.1.26$$

$$CH_3COO_2 \quad + \quad NO_2 \quad + \quad M \quad \rightleftharpoons \quad CH_3COO_2NO_2 \quad + \quad M \qquad R.1.27$$
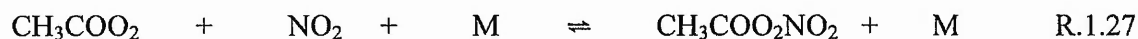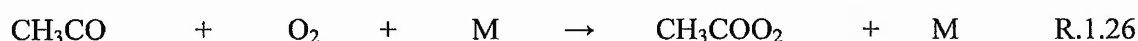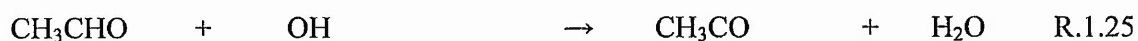
PAN is relatively stable with a lifetime of about one hour (Singh *et al.,* 1986) at the earth's surface. However, PAN can transport to higher regions of the troposphere where due to the low temperatures PAN has a lifetime of years. As a consequence of the air mass circulation patterns within the troposphere, PAN will be transported back to the lower (warmer) regions where it can decompose to yield NO_2. This circulation has an important role on NO_x lifetime and regional NO_x concentration. If the PAN returns to unpolluted areas, where it can decompose, it will enhance the concentration of NO_x species in the area, which has a knock-on effect with regards to ozone by increasing the VOC: NO_x ratio.

1.8 Chemistry in the Stratosphere

1.8.1. Oxygen Only Chemistry

The first attempt at an explanation of the existence of the ozone layer was the theoretical work of Chapman (1930). He developed a reaction scheme based on the reactions of odd oxygen, namely O_3 and O atoms. The reactions involved in Chapman's model are as follows:

$$O_2 \quad + \quad h\nu \quad \rightarrow \quad O\,(^1D) \quad + \quad O\,(^1D) \qquad \text{R.1.1}$$

$$O\,(^1D) \quad + \quad O_2 \quad + \text{ M} \rightarrow \quad O_3 \quad + \quad M \qquad \text{R.1.2}$$

$$O_3 \quad + \quad h\nu \quad \rightarrow \quad O\,(^3P) \quad + \quad O_2 \qquad \text{R.1.3}$$

$$O\,(^1D) \quad + \quad O_3 \quad \rightarrow \quad O_2 \quad + \quad O_2 \qquad \text{R.1.28}$$

$$O\,(^3P) \quad + \quad O\,(^3P) + \text{ M} \rightarrow \quad O_2 \quad + \quad M \qquad \text{R.1.29}$$
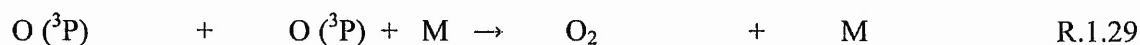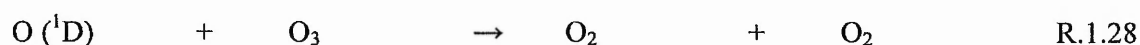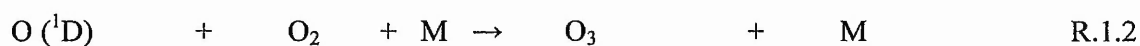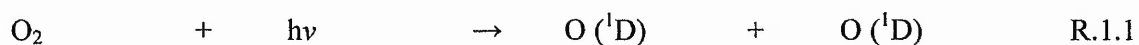
In this scheme there are two photolysis reaction (1.1) and reaction (1.3). Both of these photolysis reactions produce oxygen atoms. These oxygen atoms are either $O\,(^3P)$ or $O\,(^1D)$ where $O\,(^1D)$ is an excited oxygen atom and $O\,(^3P)$ is a ground state oxygen atom. The $O\,(^1D)$ deactivates to $O\,(^3P)$ through collisions.

$O\,(^1D)$	+	M	$\rightarrow$	$O\,(^3P)$	+	M		R.1.5
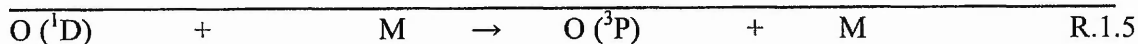
In this oxygen only scheme, reaction (1.2) becomes slower with altitude due to smaller O_2 mixing ratio. On the other hand, the reaction the photolysis of ozone shown in reaction (1.3) becomes faster at high altitudes due to the availability of photons. These two rate constraints lead to the formation of an O_3 layer.

1.8.2 Catalytic Atmospheric Loss Processes

Until around the mid 1960s it was thought that Chapman's oxygen only chemistry could explain the stratospheric ozone chemistry. However improvements of laboratory measurements have shown that the reaction rate for reaction (1.28) is too slow to destroy ozone at the rate observed in the atmosphere. The idea of catalytic atmospheric loss processes, which is based on Bates and Nicolet`s work in 1950, resolved the discrepancy between the modelled and observed stratospheric ozone levels by including extra odd oxygen removal processes.

X	+	O_3	$\rightarrow$	XO	+		O_2	R.1.30
XO	+	O	$\rightarrow$	X	+		O_2	R.1.31

Net reaction:

O	+	O_3	$\rightarrow$	O_2	+		O_2
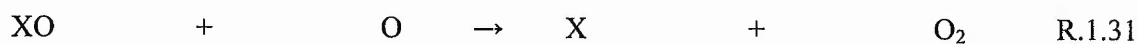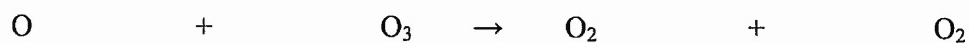
Different species have been suggested for the catalytic X in the atmosphere but the three most important amongst them for the natural stratosphere are H, OH and NO so the catalytic cycles involve HO_x and NO_x species means X can be H, OH or NO. Especially the NO_x cycle has a major impact on the destruction of odd oxygen in the lower stratosphere while HO_x cycles are more important in the upper stratosphere.

The naturally emitted compounds that are involved in stratospheric ozone loss help to keep the ozone abundance balanced. However anthropogenic emissions through the industrial activities of man augment these natural processes and can result in depletion of the ozone layer, involving catalytic ozone destruction cycles via ClO_x and BrO_x species (where ClO_x and BrO_x are the sum of Cl and ClO containing compounds and the sum of Br and BrO containing compounds respectively). Most of the chlorine and bromine in the stratosphere has come from mans emissions of stable chlorine and bromine containing compounds, such as CFCs and halons. As a consequence of their inertness many of these halogen compounds reach the stratosphere intact; where they are dissociated by solar radiation and release their halogen atom, thereby initiating ozone destruction.

1.9 Upper Troposphere Lower Stratosphere

The upper troposphere lower stratosphere (UTLS) region of the Earth's atmosphere is unique in many ways and has been the focus of a large number of research activities in recent years. This interest stems from a desire to understand the observed trends in ozone

abundances (as well as the vertical distributions of these trends), polar stratospheric ozone depletion, the oxidation mechanisms that impact the delivery of short-lived tropospheric compounds to the stratosphere, the oxidative capacity of the troposphere, and the possible impacts of aviation on UT and LS.

The UTLS region is defined as the region between the lower troposphere and middle stratosphere at mid-latitudes. Traditionally, the upper troposphere and lower stratosphere have been treated as separate entities. New insights into the dynamics of the lower stratosphere and upper troposphere, combined with an increase in constituent measurements, have forced a revision of earlier simple ideas of the structure and composition of this region and it is no longer satisfactory to think of the tropopause as a sharp boundary (Rao *et al.,*2003). This has important consequences for composition and chemistry. New measurements have shown that the composition of the lower stratosphere has, on different occasions, characteristics of either the troposphere, the stratosphere or a mixture of both. Accordingly, the dominant chemical processes in this region are not necessarily those normally associated with either the stratosphere or the troposphere, making it difficult to correctly model the chemistry of the region.

1.10 Thesis Overview

There still remains considerable uncertainty in the kinetic database, particularly for conditions of lowest temperature (200 – 250 K) and pressure (*ca* 100 mbar) that pertain to the UTLS region and thus our understanding of the chemistry within this region is also undermined by the lack of relevant kinetic data on the chemistry of the pollutants under the prevalent conditions there. The major focus of the research presented in this thesis was to undertake laboratory studies of key peroxy radical reactions at temperatures and pressures that pertain to the UTLS region.

The data reported in this thesis was collected over a period of three years. The aim of the project was to construct a turbulent flow chemical ionisation mass spectrometer system (TF-CIMS) and use it to perform laboratory studies of peroxy radical reactions with NO_x species.

Chapter 2 is intended to provide background information on (TF-CIMS) instruments and focuses on flow tube theory, gas behaviour in a flow tube system and rate coefficient determination from experiments. Also the experimental set-up and operation principles are outlined.

Chapter 3 focuses on the kinetic study of:

$$HO_2 \quad + \quad NO \quad \rightarrow \quad OH \quad + \quad NO_2 \qquad R.1.15$$

The experimental procedures used in the study of this reaction are described and the results of the experiment summarised. The data obtained has been used to make inferences about the mechanism of reaction, which is described and a section on the atmospheric implications of the results is included.

The focus of chapter 4 is the reaction:

$$HO_2 \quad + \quad NO_2 \quad + \quad M \quad \rightleftharpoons \quad HO_2NO_2 \quad + \quad M \qquad R.1.31$$
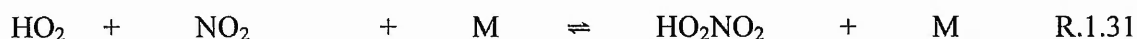
Pressure dependent rate constants are determined over an extended pressure and temperature regime. Experimental parameters and procedures are described and the data obtained compared to previous studies. Finally the data is assessed for its atmospheric implications.

In the final chapter the kinetics of reaction

$$CH_3O_2 \quad + \quad NO_2 \quad + \quad M \quad \rightleftharpoons \quad CH_3O_2NO_2 \quad + \quad M \qquad R.1.32$$
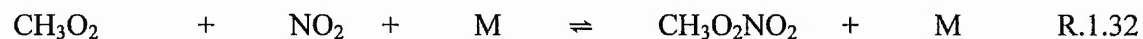
Is studied. As previously seen, methane is the dominant organic emission found in the atmosphere. In this chapter, the kinetics of its reaction with NO_2 are determined and reported. Experimental procedures are described and a comparison of these data with previous studies is performed.

References

Andrews, D.G., Holton, J.R. and Leovy, C.B., *Middle atmosphere dynamics,* Academic Press Inc., London, 1987

Atkinson R., *Atmos. Environ.*, 2000, **34**, 2063

Chapman, S., *Mem. Roy. Meteo. Soc.*, 1930, **3**, 103

Campbell, I.M., *Energy and the Atmosphere*, John-Wiley and Sons, New York, 1986

Cox, R.A., *Tropospheric Ozone*, D. Reidel Publishing Company, Holland, 1988

Dubey, M.K.; Mohrschladt, R.; Demerjian, K.L.; Donahue, N.M., and Anderson, J.G.; *J. Geophys. Res.*, 1997, **102**, 6153

Finalyson-Pitts, B.J. and Pitts, J.N., *Atmospheric Chemistry*, John-Wiley and Sons, New York, 1986

Kasting, J. F., *Science,* 2001, **293**, 819

Lutgens F.K. and Tarbuck E.J., *The Atmosphere*, **8**th edn. Prentice Hall, Englewood Cliffs, New Jersey, 2001

Madronich, S. and Hess, P., *Proceedings of the 6*th *European Symposium on Physico-Chemical Behaviour of Atmospheric Pollutants*, Varese, 1994

McElroy, M.B. and Salawitch, R.J., *Science*, 1989, **243**, 763

Penkett, S.A.; Bandy, B.J.; Reeves, C.E. and Hignett, P., *Faraday Discuss.*, 1995, **100**, 10

Rao, T.N.; Kirkwood, S.; Arvelius, J.; von der Gathen, P.; Kivi, R., *J. Geophys. Res.*, 2003, **108**, art. No. 4703

Singh, H.B. and Salas, L.J., *Geophys. Res. Lett.*, 1982, **9**, 842

Wayne, R. P., *Chemistry of Atmospheres*, **3**rd edn., Oxford University Press, Oxford, 2000

Wiechert, U., *Science*, 2002, **298**, 2341

Chapter 2

Flow Tube Theory and Experimental Set - Up

2.1 Flow Tube Theory

A schematic diagram of a typical flow tube system is shown in Figure 2.1. Flow tubes are usually made out of Pyrex tubing 80 – 100 cm in length with an internal radius about 2.2 cm. The operational idea behind the discharge flow technique is based on the relation between reaction time and reactant concentration. The reaction starts at point *a* and ends at the point of detection point *b*. The time of reaction can be calculated if the velocity of gas mixture in the flow tube is known.
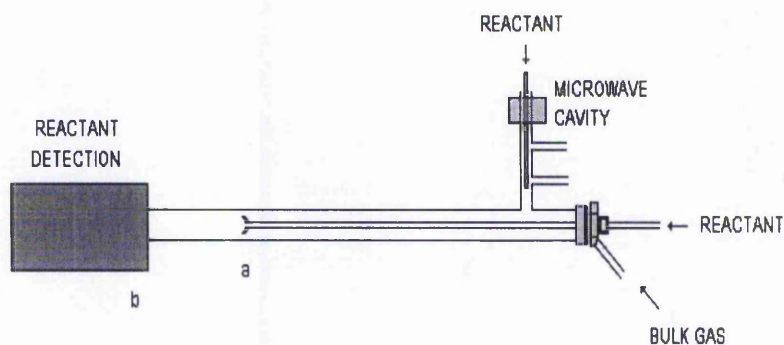
Figure 2.1: A schematic diagram of a typical flow tube system.

Radicals are typically generated using a microwave discharge in a side arm, which is at the rear end of the discharge flow tube system. Radicals are introduced into the main bulk flow and are well mixed as they reach the point *a* where the reaction starts. As they reach the point *b* reaction finishes and products enter the detection system.

Reaction time is varied by altering the position of a sliding injector. Concentration can then be plotted against reaction time and the experiment repeated. By examining decay profile of the relative radical concentration as a function of injector positions and hence reaction time, the pseudo-first-order rate coefficient can be evaluated. The use of the discharge flow technique has several advantages. The steady state conditions employed in a flow system readily permit signal accumulation. A huge variety of methods can be used to detect reactants and products. The steady-state nature of the flow system means that there is no time limitation for the detector speed.

The second major advantage of the flow tube method is the great versatility it provides for working with a wide variety of reactants within the flow tube. Separate radical generation enables two different labile reactants to be produced and thus radical-radical reaction can be studied as seen in reaction (2.1) Reimann and Kaufman, (1978).

$$HO_2 \quad + \quad ClO \quad \rightarrow \quad HOCl \quad + \quad O_2 \qquad R.2.1$$
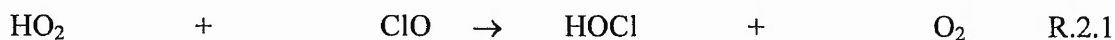
Titration reactions play an important role in the reaction versatility of the flow tube, since they make it possible to produce accurately known concentrations of labile reactants.

However, flow tubes have been limited by the need to work at low pressures (P = 1 – 20 Torr). There are inherent drawbacks to operating at such low pressures. First, the narrow pressure range severely hampers the study of termolecular reactions. Second, the collision frequency of trace species with the flow tube walls is very high, so that reactions at the walls interfere with measurements, particularly at low temperatures (T < 250 K). As a consequence, there is a lack of high quality kinetic data below 250 K. The focus of the research presented in this thesis will be on the use of flow tubes over extended temperature and pressure ranges and the following sections will discuss the theory and operation of flow tube techniques for the study of radical reactions.

2.1.1 Fluid Dynamics Within Flow Tubes

Gas flow down the tube is caused by an axial pressure gradient, which is created by bulk amount of carrier gas (typically He, Ar or N_2) injected at one end of the tube. One of the reactants is generally introduced through a sliding injector, which is able to move in and out along the length of the flow tube without breaking the seal or affecting the observed signal. The other reactants usually enter the flow tube from the rear end through a side arm inlet. Trace amounts of reactants are continuously added to the flow. The other end of the tube is generally where the detection system and pumping equipment are accommodated.

A viscous retarding force originating at the flow tube walls opposes the force pushing the gas down the flow tube. At the entrance of the flow tube, only the molecules adjacent to the

walls experience a viscous retardation. As the gas travels down the region under the influence of the viscous forces, the boundary layer increases. While the boundary layer builds up, a velocity profile develops, which is zero at the flow tube walls and maximum at the centre of the tube. The axial distance needed for the boundary layer to reach the centreline of the tube is known as the entrance length. Downstream of the entrance length, the fluid dynamics do not vary greatly with axial position and hence the flow is considered to be fully developed.

The motion of a fluid as it travels in the tube is dependent on the ratio of convective momentum to viscous dissipation. Convective momentum transport is proportional to $\rho \bar{v}^2$, where ρ is the density of the gas, $\bar{v}$ is the average velocity of the gas flow inside the flow tube system. The viscous dissipation of momentum is proportional to $\mu \bar{v} / 2\, a$, where μ is the viscosity coefficient of the gas and a is the internal radius of the flow tube. The type of flow along the flow tube can be estimated using the dimensionless ratio known as the Reynolds number, *Re* given by Equation 2.1:

$$\mathrm{Re} = \frac{2a\rho\bar{v}}{\mu} \qquad \text{E.2.1}$$

where a is the internal diameter of the flow tube, $\bar{v}$ is the average velocity of the carrier gas, ρ is the density of the carrier gas and μ is the viscosity of the carrier gas. For the low values of *Re,* the viscosity dissipation dominates creating laminar flow. For large values of *Re,* viscous dissipation is unable to cut out the fluid movement and turbulent flow results. Empirically it has been found that laminar flow is generally stable at *Re* < 2000 and that turbulent flow is stable at *Re* > 3000.

Laminar flow is characterized by streamlined fluid convection. The velocity profiles for fully developed laminar flow can be calculated using Equation 2.2:

$$v_r = 2\bar{v}\left[1 - \left(\frac{r}{a}\right)^2\right]$$
E.2.2

where v_r is the velocity in the axial direction, $\bar{v}$ is the velocity of the bulk gas and r is the radial coordinate and a is the internal diameter of the flow tube. Turbulent flow is characterized by a multitude of eddies with rapidly oscillating trajectories. Unlike laminar flow, the fully developed velocity profile for turbulent flow cannot be exactly determined from simple theoretical considerations. However, a good empirically derived approximation is given by:

$$v = v_c\left(1 - \frac{r}{a}\right)^{1/n}$$
E.2.3

where v_c is the velocity at $r = 0$ (centre of flow tube), r is the radial coordinate and a is the internal diameter of the flow tube and n is a parameter which depends on Re. Figure 2.2 shows fully developed laminar and turbulent flow velocity profiles within a flow tube and it can clearly be seen that the turbulent flow velocity profile is flatter than the laminar velocity profile in the centre of tube.

Within the turbulent flow regime, random motion occurs at the molecular level and at a larger size scale due to eddy motion. In turbulent flow, the region near the wall ($r < 0.9\ a$)

is commonly called the Laminar sub-layer since it is relatively free of eddy motion. The region in the central portion of the tube is commonly called the turbulent core.
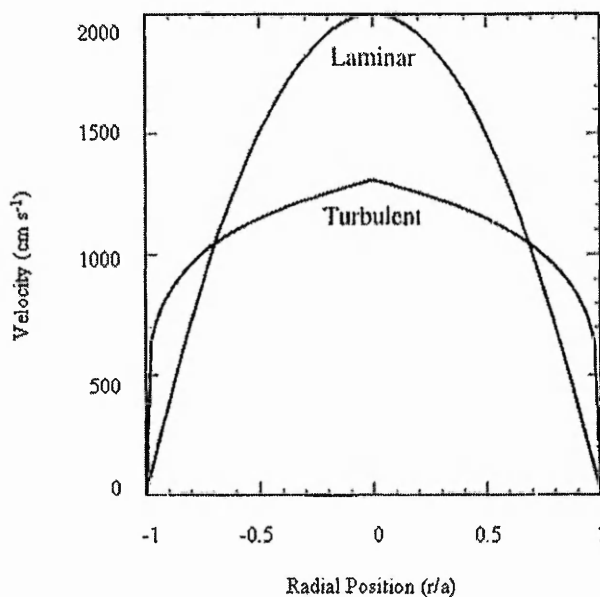
Figure 2.2: Fully developed velocity profiles for the laminar and turbulent flow regimes.

2.2 Kinetic Studies Using the Flow Tube Technique

The concentration of labile species in a flow tube depends on several processes, namely convection, diffusion, heterogeneous reactions (reactions between radicals and reactors inner surface) and homogeneous reactions processes. All these terms can be mathematically modelled using the continuity equations, which are derived from mass conservation principles.

$$\nabla(E_i\nabla C_i) - \nabla(vC_i) + K_i = 0 \qquad\qquad \text{E.2.4}$$

Equation 2.4 can be created under the assumption of isothermal and constant density conditions, where i is a reactive species in a steady state flow reactor and C_i is the concentrations of i species, E_i is the diffusivity of reactants in the flow tube, v is convective velocity and K_i is the total rate of chemical production of i species.

Assuming that only one type of homogeneous reaction can occur within the flow tube, *i.e.* $A + B \rightarrow products$, it can be shown that the continuity equation for the flow tube system reduces to:

$$\nabla(E_A\nabla C_A) - \nabla(v\,C_A) - kC_AC_B = 0 \qquad\qquad \text{E.2.5}$$

$$\nabla(E_B\nabla C_B) - \nabla(vC_B) - kC_AC_B = 0 \qquad\qquad \text{E.2.6}$$

where k is the bimolecular reaction rate coefficient. In order to calculate k Equation 2.5 and Equation 2.6 need to be solved and for the solution v, C_A, C_B, E_A and E_B must be known. Experimentally, such measurements can be made, however, collecting the data for every different point of flow tube system requires a large number of measurements. However, if some of the operating conditions are optimised accurate predictions can be made and the solution of the continuity equation becomes much easier.

Creating and operating under pseudo-first-order conditions is one such solution. Pseudo-first-order conditions assumes that the concentration of one of the reactants is constant with respect to time and space, *e.g.* B must be thoroughly mixed and not substantially depleted

by chemical reactions. The effect of homogenous removal on C_B is minimized by injecting an excess amount of B. Experiments have determined that minimal errors occur when the amount of B is at least an order of magnitude greater than the amount of A (Howard, 1979).

Under pseudo-first-order conditions in the flow tube, C_B can be considered independent of position. Under these conditions the continuity equation for limiting reactant A is,

$$\nabla\left((E_A \nabla C_A) - \nabla(v\,C_A) - k^1 C_A = 0\right) \qquad \text{E.2.6}$$

where k^1 is the pseudo-first-order reaction rate coefficient given by $k^1 = kC_B$.

In flow tube studies it is typically assumed that the concentration of the limiting reactant, C_A, depends only on axial position and that reactant transport in the axial direction is exclusively due to convection (*i.e.* axial diffusion can be neglected). Under these assumptions the continuity equation of the limiting reactant becomes:

$$-\bar{v}\frac{\partial C_A}{\partial z} - k^1 C_A = 0 \qquad \text{E.2.7}$$

where z is the axial position of reagent C_A, k^1 is the pseudo-first-order rate coefficient for the reactive loss of C_A and $\bar{v}$ is the bulk gas velocity. Inspection of the Equation 2.7 shows that the approximations made to derive the equation are the equivalent of stating that each molecule travels at a velocity $\bar{v}$; which is commonly called the plug flow approximation.

The plug flow approximation is only accurate when axial diffusion and radial concentration gradients are negligible.

The relationship between C_A and k^I can be determined by integrating the Equation 2.7.

$$C_A(z) = C_A(z_0) \exp\left(-\frac{k^1(z - z_0)}{\bar{v}}\right) \qquad \text{E.2.8}$$

Thus by using the Equation 2.8 the bimolecular rate constant can be determined.

2.2.1 Limitations of Laminar Flow

Axial diffusion effects are significant below 3 Torr, but can easily be accounted for by adding an axial diffusion term into the continuity equation. However, radial concentration gradients cannot easily be accounted for and represent the major limiting factor for the use of laminar flow systems.

There are two main sources of radial concentration gradients in the laminar flow regime. First, radial concentration gradients are formed when the radial transport of C_A is much slower than the rate of chemical removal. This confines the reactive molecules to their original radial positions. Reactants at the centre of the tube experience a shorter reaction times than those at the walls as a consequence of the peaked laminar velocity profile. Subsequently, the degree of homogeneous chemical depletion becomes more pronounced

near the flow tube walls. Second, radial concentration gradients become more pronounced with increasing pressure because the diffusive transport correspondingly decreases. It has been found that rate constants using the plug flow approximation are unreliable when the pressure is above 10 Torr (Howard, 1979).

Under low-pressure conditions the reactant molecules experience many collisions with the flow tube walls, which cause heterogeneous interferences. Radial concentration gradients are also formed if heterogeneous reactions occur to an appreciable extent on the flow system walls. For many species the heterogeneous loss at the walls has been found to increase dramatically as the temperature decreases. Although the reactivity of walls can be reduced by the use of coatings, the heterogeneous loss becomes prohibitively large at temperatures below 250 K (Howard, 1979).

A number of groups have attempted to determine rate coefficients under high-pressure laminar flow conditions (P > 10 Torr). One approach involves solving the continuity equation for fully developed laminar flow conditions by adding the axial and radial diffusion terms into the continuity equation (Walker, 1961; Ogren, 1965; Poirer and Carr, 1971; Brown, 1978; Keyser, 1984), there are two main difficulties with this approach, namely:

1) uncertainties in retrieved rate coefficients with increasing pressure or as wall loss processes increase;

2) creating fully developed laminar flow in high pressure.

More recently, for example, Abbatt *et al.*, (1990) have created a flow tube reactor in which the values of v and C_A can be experimentally determined as functions of radial and axial position. Rate constants are determined by substituting the values of C_A and v into the continuity equation and numerically solving for k. With this method, they have determined rate constants under both laminar and turbulent flow conditions at pressures ranging from 7 to nearly 400 Torr. Although this approach can generate accurate rate constants, the experimental simplicity of the conventional flow tube technique has been sacrificed. Furthermore, the approach of Donahue and Anderson has so far been limited to the study of OH, HO_2 and H atom reactions (Donahue *et al.*, 1996; Clarke *et al.*, 2000).

2.2.2 Turbulent Flow Conditions

The main problems associated with the use of laminar flow conditions at high pressures are:

- Molecules experiencing different reaction time due to peaked shape velocity profile under laminar flow conditions;

- Creating homogeneous mixing in the flow tube system;

- Wall loss process may well have a huge impact on determining the rate constant;

- Accuracy unknown;

- Creating fully developed laminar flow at high pressures.

As we have seen before in Figure 2, a fully developed velocity profile for turbulent flow conditions is much flatter than a laminar flow velocity profile, thus the plug flow approximation holds regardless of pressure. A further advantage of using turbulent flow conditions is that wall loss is greatly reduced.

Seeley (1994) expressed the reactant wall loss as a first order decay constant, k_w and calculated the dependence of k_w on pressure (and hence Reynolds number) for a prescribed set of P (pressure) and γ (collision efficiency for wall loss), as shown in Figure 2.3.
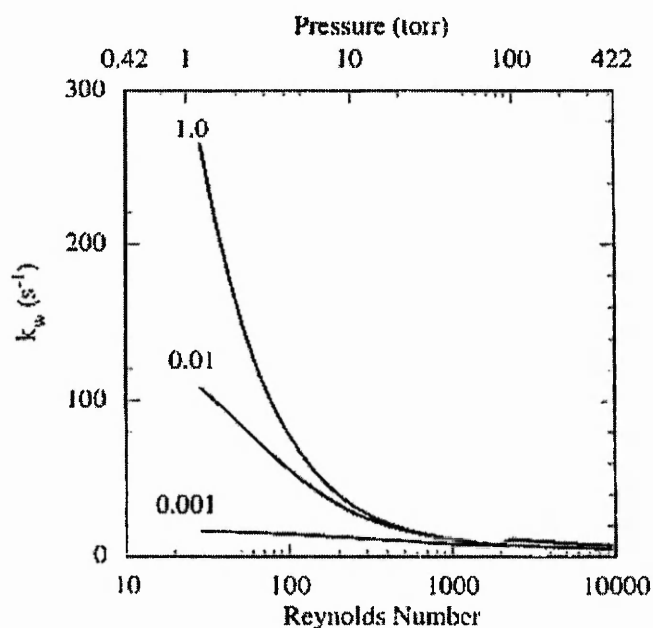
Figure 2.3: A plot of wall loss as a function of pressure, taken from Seeley (1994).

In Figure 2.3 it can be seen that the wall loss is greatly reduced as turbulent flow conditions are achieved. In the transitional regime where 2000 < Re < 3000 there is small increase in k_w as a consequence of increased radial mobility from Eddy diffusion.

The greatly reduced wall loss using turbulent flow conditions enables the study of reaction

kinetics at much lower temperatures than were previously accessible using laminar flow.

Therefore, the use of turbulent flow conditions greatly increases the operating regimes so

that the flow tube can be employed without sacrificing experimental simplicity. For

example, Percival *et al.,* 1997 have studied the reaction $ClO + NO_2$ over the pressure range

$150 - 600$ Torr and the temperature range of $213 - 298$ K.

2.3 Experimental Set-Up

2.3.1 Flow Tube

A schematic diagram of the experimental system used in this work is shown in Figure 2.4.

The flow tube was constructed from Pyrex tubing with a 22 mm internal diameter (id), the

walls of the flow tube were coated with Halocarbon wax (Halocarbon Products Inc.).
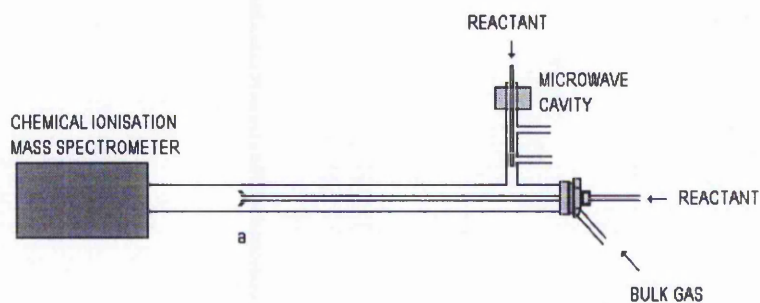
Figure 2.4: A schematic diagram of the flow tube system.

A large flow of nitrogen (ranging from 40 to 150 STP litre min^{-1}) (standard litres per minute) was injected into the flow tube from the rear end. The flow tube system was pumped by a rotary pump (Varian, DS1602). Reactants were injected either through a moveable injector or *via* the side arm inlets. The sliding injector was constructed from Pyrex 3 mm (id). A propeller-like Teflon piece (a 'turbulizer') designed to enhance turbulent mixing was fixed to the end of the moveable injector, in order to ensure rapid mixing of reactants with the bulk N_2 flow.

A series of flow visualization experiments were performed to observe mixing characteristics of reactants in the flow tube. The Chemiluminescent reaction,

$$O \qquad + \qquad NO \quad \rightarrow \quad NO_2 \qquad + \qquad h\nu \qquad R.2.2$$

was used to visualize the mixing patterns in the flow tube system. Oxygen atoms were produced by microwave cavity and NO was added into flow through a sliding injector. Mixing pattern visualization study results can be seen in Figures 2.5 and 2.6.
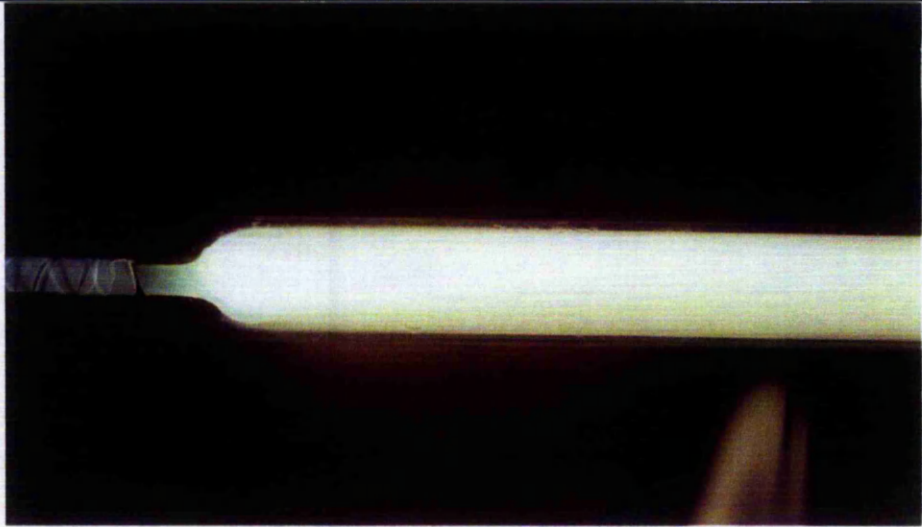
Figure 2.5: A picture of mixing under turbulent flow conditions with a turbulizer fixed onto the sliding injector.
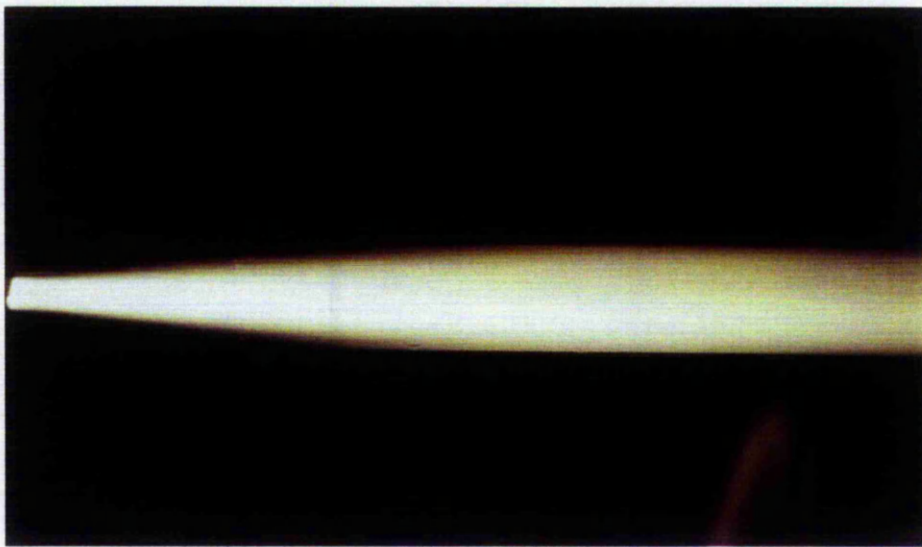
Figure 2.6: A picture of mixing under turbulent flow conditions without a turbulizer fixed onto the sliding injector.

For the accurate determination of rate parameters using flow tube systems the mixing of reactants with the bulk N_2 flow should ideally occur within a distance of $2R$ from the point of injection. In Figure 2.5 it can be seen that mixing occurs almost instantaneously when a turbulizer is placed on the end of the sliding injector. However, if the turbulizer is removed, as shown in Figure 2.6, "jet streaming" of reactants occurs and the mixing length is much greater than $2R$. Therefore, the addition of a turbulizer ensures rapid mixing and ensures that the contact time of reaction can be estimated accurately.

2.3.2 Temperature Control

Accurate flow tube temperature control is necessary for sub-ambient kinetic experiments to enable the temperature dependence of a reaction to be studied. To ensure correct determination of reaction rates uniform temperature is needed along the length of the flow tube. The temperature in the flow tube was monitored and controlled using the system shown in Figure 2.7.

THERMOCOUPLES

PRE COOLED
BULK GAS

TEMPERATURE
CONTROL UNIT
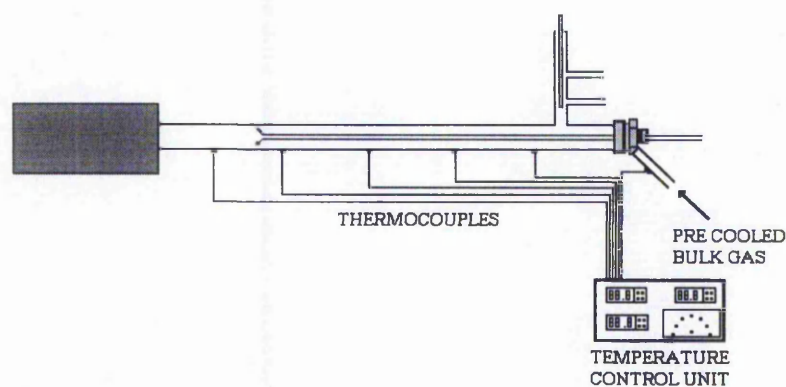
Figure 2.7: A schematic diagram of the flow tube temperature control system.

All temperatures were monitored using type K thermocouples connected to electronic controllers (Carel Universal Infrared control type W). Maintenance of temperature was achieved using resistive heating tape (Omega, Heavy duty) regulated by the electronic controllers. Before entering the flow tube the bulk nitrogen flow was passed through a copper coil immersed in liquid nitrogen, which pre-cooled the bulk gas flow to approximately 78 K. Then the bulk gas carrier line was resistively heated to the desired temperature. The bulk gas flow temperature was checked and controlled by a thermocouple at the flow tube entry point.

The flow tube temperature was monitored along its length by five thermocouples attached to the surface of the flow tube and in order to keep the desired temperature stable, the flow tube placed into an insulated chamber filled with dry ice. The temperature of the flow tube was controlled by heavy duty heating tape also underneath the heating tape a layer of thin copper foil wrapped around the flow tube in order to reduce "hot spots" as shown in Figure 2.8.
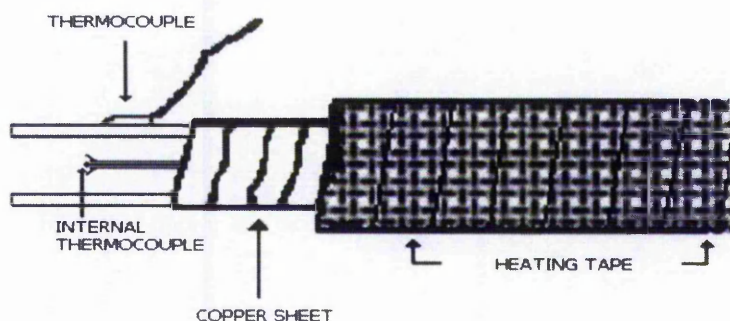
Figure 2.8: A cutaway diagram of the flow tube heating levels.

The internal temperature profile was determined by placing a thermocouple on the tip of the sliding injector. The heating tape controllers were set to the desired temperature using the surface thermocouples. The desired internal temperature profile was characterized using the sliding injector thermocouple. By changing the axial position of the sliding injector the internal temperature profile can be measured by plotting the axial position of the internal thermocouple against temperature as shown in Figure 2.9. The temperature within the flow tube can be altered by changing the heating tape set points. The control parameters were recorded along with the response of the five external thermocouples along the flow tube walls to enable the temperature to be re-attained at a later date in the absence of the sliding injector thermocouple.
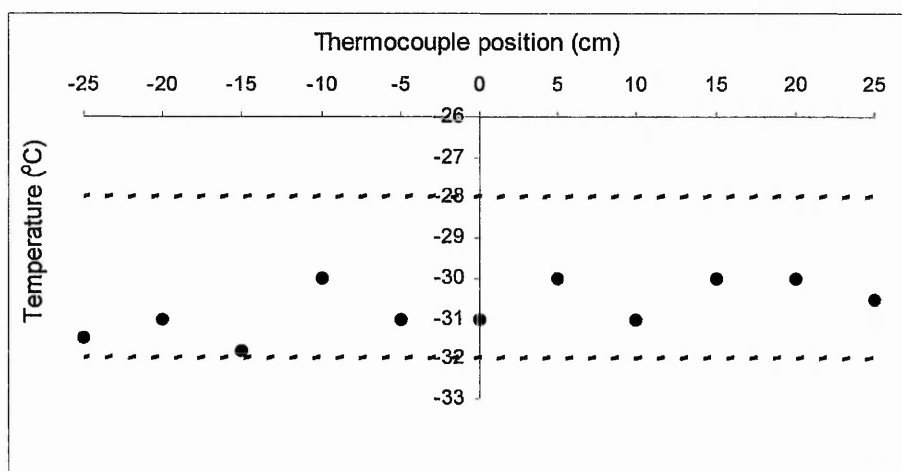
Figure 2.9: The axial temperature profile was obtained for 243 K. The centre of the flow tube was used as the reference point. Axial changes were made 5 cm in either way backwards and forwards.

By using this method of temperature control it was possible to set the internal temperature of the flow tube to within ± 2 K over the temperature range T = 193 – 298 K.

2.4 Production of Peroxy Radicals

The work presented in this thesis will focus on the reactions of HO_2 and CH_3O_2. The peroxy radicals were generated in the side arm, located at the rear of the flow tube, *via* a set of titration reactions as summarised in Table 2.1

Radical	Chemical source							
CH_3O_2	F_2					$\rightarrow$	2F	
	F	+	CH_4			$\rightarrow$	CH_3	+	HF
	CH_3	+	O_2	+	M	$\rightarrow$	$\mathbf{CH_3O_2}^+$	+	M
HO_2	H_2					$\rightarrow$	2H	
	H	+	O_2	+	M	$\rightarrow$	$\mathbf{HO_2}$	+	M

Table 2.1: Radical source chemistry.

Atomic species, either H or F, were generated *via* the action of a microwave discharge produced by a Surfatron (Sairem) cavity, then injected into the side arm *via* a moveable quartz inlet as shown in Figure 2.10. The side arm was constructed of 8.4 mm id Pyrex and was 9 cm long and had two orthogonal inlets of 3 mm id Pyrex to enable the addition of suitable titrants to convert the atomic species into peroxy radicals as outlined in Table 2.1.
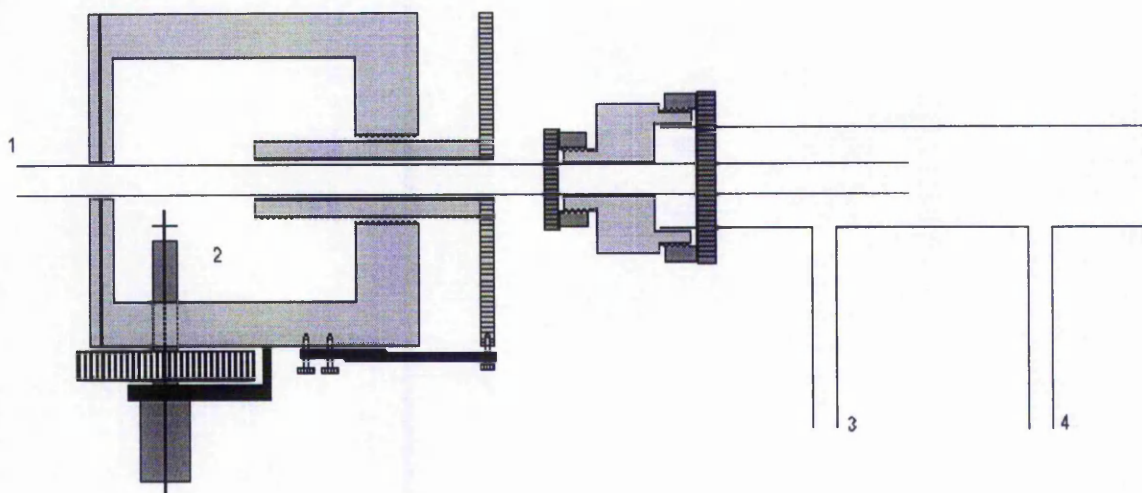
Figure 2.10: A schematic diagram of microwave cavity and side arm where:

1   Inlet for atomic precursor quartz made tube with a 3 mm internal diameter;

2   Microwave cavity that can operate from 0 to 300 Watts;

3   Inlet for the first titrant gas;

4   Inlet for the second titrant gas.

The specific conditions used for the generation of radicals relevant to each studied reaction will be explained in detail in the following chapters.

2.5 Sampling of Gases Into the Detection Region.

To enable the study of peroxy radical reactions at a pressure greater than 200 Torr an expansion region was attached to the end of the flow tube. The expansion region was constructed from Teflon and it was machined with a conical shape head, in order to minimise dead space, with a 2 mm hole in the centre as shown in Figure 2.11.
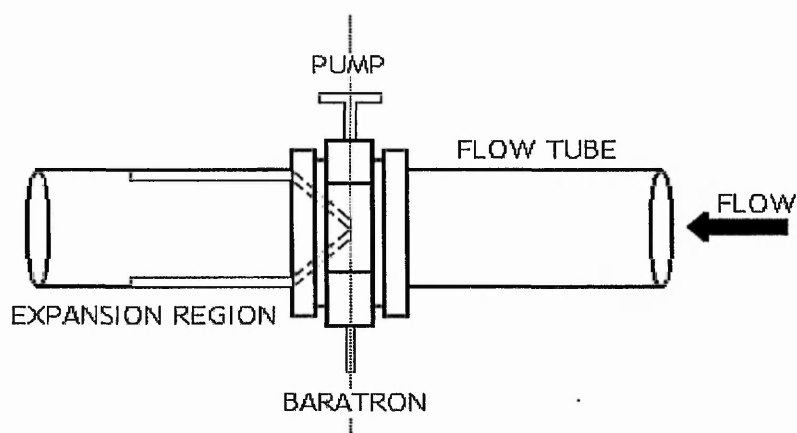
Figure 2.11: A schematic diagram of the expansion region.

The pressure in the expansion region was held at approximately 45 – 55 Torr using a rotary pump (Varian, DS1602). The pressure in the region was monitored using a 0 – 1000 Torr capacitance manometer (MKS, Baratron). Throughout this work the end point of the reaction was considered to be the tip of the conical Teflon piece.

2.6 Chemical Ionisation Mass Spectroscopy (C.I.M.S.)

The turbulent flow system was coupled to a CIMS for the detection of transient species within the flow tube. A portion of the gases within the flow tube was sampled *via* the expansion region into an ion molecule region. A schematic diagram of the chemical ionisation region is shown in Figure 2.12. The ion molecule region was constructed from Pyrex tube with a 22 mm id.
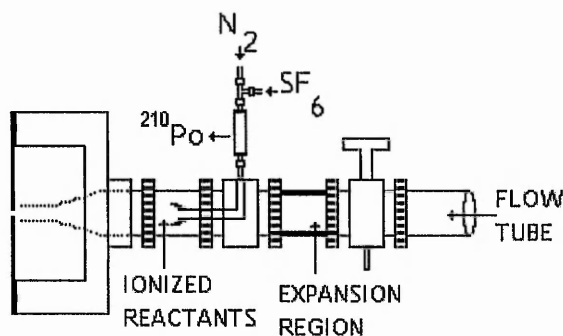
Figure 2.12: A schematic diagram of the ion molecule region.

All transient species within the flow tube were chemically ionised using SF_6^- as the reagent ion. SF_6^- was generated by combining a 10 STP litre min^{-1} flow of N_2 and a 2.5 STP cm^3 min^{-1} flow of SF_6 and passing it through a ^{210}Po Nuclecel ionizer (NRD Inc.). The radioactive source (^{210}Po) emits α particles, which then ionise the N_2 bulk gas creating secondary electrons that rapidly react with SF_6 to produce precursor ion SF_6^-. Precursor

ions then react selectively with the transient species within the flow tube *via* either electron transfer reaction, fluoride ion exchange reaction or complex reactions as shown below.

$$SF_6^- \quad + \quad NO_2 \quad \rightarrow \quad NO_2^- \quad + \quad SF_6 \qquad R.2.3$$

$$SF_6^- \quad + \quad CH_3O_2 \quad \rightarrow \quad CH_3O_2^- \quad + \quad SF_6 \qquad R.2.4$$

$$SF_6^- \quad + \quad HO_2 \quad \rightarrow \quad SF_4O_2^- \quad + \quad prods \qquad R.2.5$$

$$SF_6^- \quad + \quad HNO_3 \quad \rightarrow \quad NO_3.HF^- \quad + \quad SF_5 \qquad R.2.6$$

The ions are then sampled into a quadrupole mass spectrometer and detected. The main advantages of CIMS are that it is a soft ionisation process and unlike conventional electron impact mass spectrometers, CIMS produces ions at high pressures (20 – 760 Torr). The main benefit of creating ions at high pressures is that ions can be focused by electrostatic lenses at each pumping stage and thus minimise the loss of ion signal.

2.7 Ion Detection

Mass spectrometry is a technique used to determine the value of the mass/charge ratio and the experimental set up is easy to use and has a relatively high sensitivity for detection. Applications of the technique to the reaction kinetic studies give scientists the opportunity to monitor every species individually and simultaneously as a function of time.

Successful sampling has been a major obstacle in the application of mass spectrometry for detecting radicals in discharge-flow reactors. The sensitivity of detection can greatly be improved by the use of a multistage sampling system. The reaction mixture expands out of the first sampling region at super sonic velocity in the forward direction (Anderson *et al.*, 1965) and focus lenses select the portion of this sample for onward transmission to the quadrupole. Because of the high degree of collimation and the supersonic velocity of the sample gas, collisions between radicals themselves and between radicals and the stainless steel walls of the mass spectrometer inner walls are insignificant.

Ions generated in the ion molecule region were detected with a quadrupole mass spectrometer in a three-stage differentially pumped vacuum chamber, as shown in Figure 2.13.
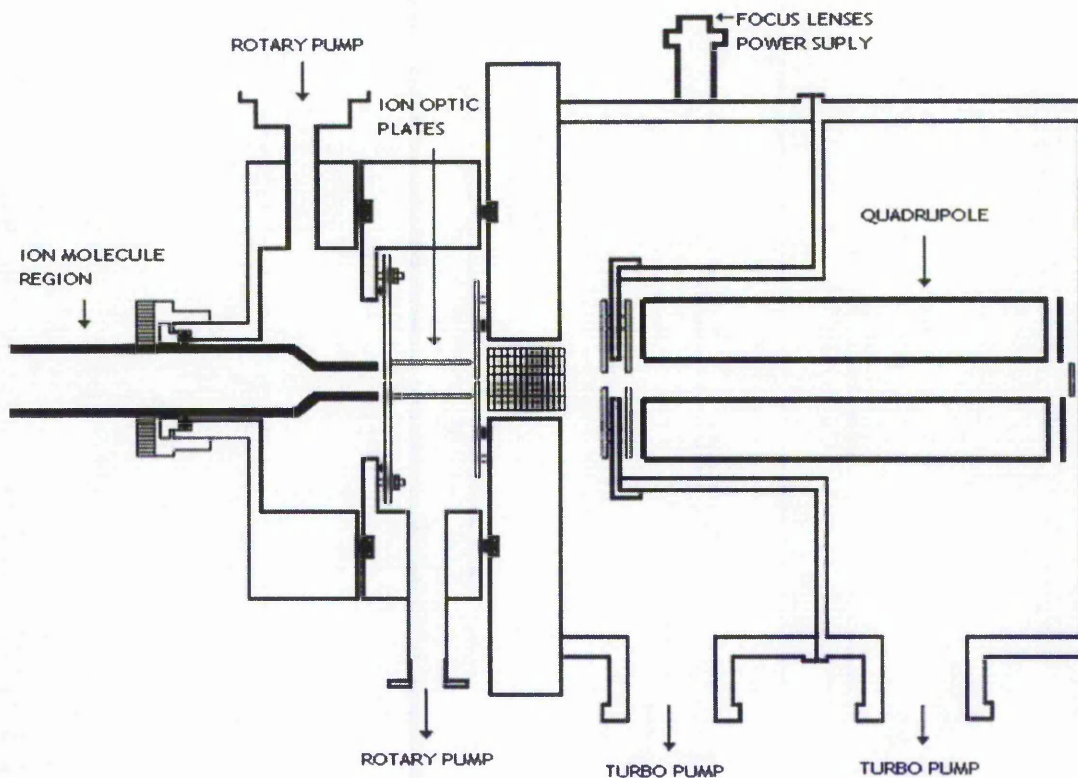
Figure 2.13: A schematic diagram of CIMS interface.

Ion-molecule gases (neutrals and ions) were drawn into the front chamber through a 0.6 mm aperture, which was electrically charged. The front vacuum chamber was pumped by a mechanical pump (Varian, DS402) and held at approximately 2 Torr.

The ions were further focused by a 3 cm od and 0.2 mm id charged stainless steel plate and passed into a second chamber containing the quadrupole mass filter (ABB Extrel, Merlin). The second chamber was pumped by a turbo molecular pump (Varian, V250) backed by a rotary pump (Edwards, E2M8). The rear chamber, which held the multiplier assembly, was pumped by a further turbo molecular pump (Varian, V250) backed by a rotary pump (Edwards, E2M2). Under typical operating conditions the rear chamber was at a pressure of approximately 9×10^{-6} Torr. A complete TF—CIMS system is shown in Figure 2.14.
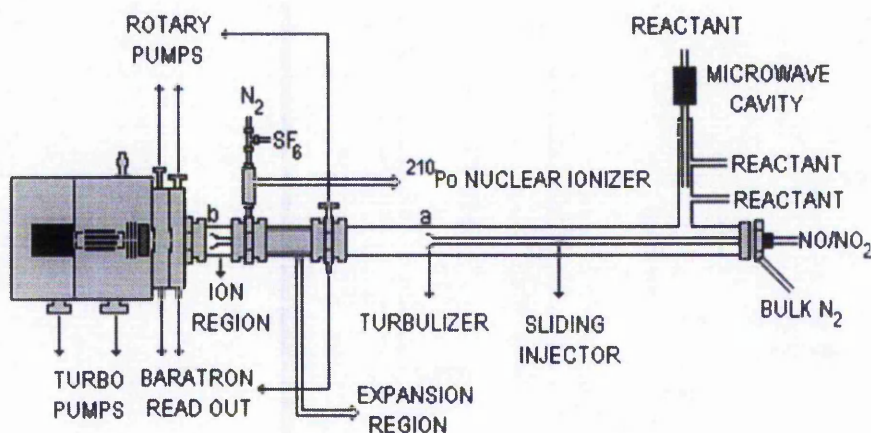
Figure 2.14: A schematic diagram of a complete Turbulent Flow Chemical Ionisation Mass Spectrometer.

The following experimental results chapters will describe the application of the TF—CIMS system to the study of peroxy radical reactions. Each chapter will be self-contained, in that each chapter will describe the specific experimental set up and explain the operating procedures for each reaction studied in detail.

References

Abbatt, J. P. D.; Demerjian, K. L.; Anderson, J. G., *J. Phys. Chem.*, 1990, **94**, 4566

Anderson, J. B.; Andres, R. P.; Fenn, J. B., *Adv. At. Mol. Phys.*, 1965, **1**, 345

Brown, R. L., *Journal of Research of the National Bureau of Standards*, 1978, **83**, 1

Clarke, J. S.; Donahue, N. M.; Kroll, J. H.; Uncu E.; Rypkema, H. A.; Anderson, J. G.; *J. Phys. Chem.* A, 2000, **104**, 5254

Donahue, N. M.; Clarke, J. S.; Demerjian, K. L.; Anderson, J. G., *J. Phys. Chem.*, 1996, **100**, 5821

Howard, C. J., *J. Phys. Chem.*, 1979, **83**, 3

Keyser, L.F., *J. Phys. Chem.*, 1984, **88**, 4750

Ogren, P. J., *J. Phys. Chem.*, 1975, **79**, 1749

Percival, C.J.; Smith G.D.; Molina L.T. and Molina M.J., *J. Phys. Chem. A*, 1997, **101**, 8830

Poirier, R. V.; Carr, R. W. Jr., *J. Phys. Chem.*, 1971, **75**, 1593

Reimann, B.; Kaufman, F., *J. Chem. Phys.*, 1978, **69**, 2925

Seeley, J.V., *Experimental Studies of Gas Phase Reactions Using the Turbulent Flow Tube Technique*, Ph.D. Thesis, Massachusetts Institute of Technology, 1994

Walker, R. E., *Phys. Fluids*, 1961, **4**, 1211

Chapter 3

Kinetics of the Reaction Between HO_2 and NO

3.1 Introduction

In the troposphere the primary source of HO_2 is through the reaction sequence shown below. Photolysis of ozone at wavelengths less than ~ 310 nm produces an excited singlet oxygen atom capable of reacting with atmospheric water. The resulting hydroxyl radicals react with CO to produce atomic hydrogen that then go on to react with oxygen to produce the HO_2 radical (Wayne, 2000).

O_3	+		$h\nu$	$\rightarrow$	$O\,(^1D)$	+	$O_2\,(^1\Delta_g)$	R.3.1
$O\,(^1D)$	+		H_2O	$\rightarrow$	OH	+	OH	R.3.2
OH	+		CO	$\rightarrow$	H	+	CO_2	R.3.3
H	+ O_2 +	M		$\rightarrow$	HO_2	+	M	R.3.4
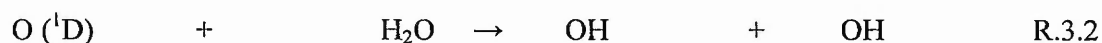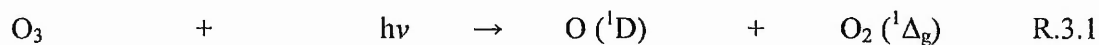
The fate of the HO_2 radical in the upper troposphere is dependent on ambient concentrations of NO_x. In the clean troposphere where there are very low levels of NO_x, HO_2 undergoes reaction with ozone to produce OH and O_2 as shown in reaction (3.5).

HO_2	+		O_3	$\rightarrow$		OH	+	$2O_2$	R.3.5

This results in a loss of both ozone and HO$_2$ radical. However the OH formed in reaction (3.5) can undergo further reaction with ozone to produce HO$_2$ setting up a catalytic cycle, which results in the depletion of ozone in the UTLS region. However, in the polluted troposphere where higher levels of NO$_x$ are encountered HO$_2$ reacts with NO *via* reaction (3.6)

| HO$_2$ | + | NO | $\rightarrow$ | OH | + | NO$_2$ | R.3.6 |

| NO$_2$ | + | hν ($\leq$ 410 nm) | $\rightarrow$ | NO | + | O | R.3.7 |

| O | + O$_2$ + | M | $\rightarrow$ | O$_3$ | + | M | R.3.8 |

Further reactions (3.7) and reaction (3.8) result in the production of ozone and an increase in the oxidising potential of the atmosphere (Finlayson-Pitts and Pitts, 1986). Work by Wennberg *et al.,* (1998) has shown that measurements of HO$_x$ in the upper troposphere are significantly higher than expected, this coupled with the increase in NO due to a larger volume of commercial air traffic could lead to higher levels of ozone in the UTLS region. Also, recent work by Salawitch *et al.,* (2002) has shown a discrepancy between calculated and observed levels of HO$_x$ of around 6% at mid latitudes. In order to accurately model ozone levels in the UTLS accurate data are needed for reaction (3.6) at pressures and temperatures pertaining to the UTLS region *i.e.* 180 – 300 K and 100 – 250 Torr.

3.2 Previous Experimental Studies on the Reaction of $HO_2 + NO$

Previous work on reaction (3.6) is summarized in Table 3.1. There have been numerous studies of the reaction at room temperature. These studies have been performed over a wide range of pressures and are in good agreement, therefore reaction (3.6) can be considered as being well characterized at room temperature. However, despite the importance of the reaction (3.6) for the UTLS region there have only been two experimental studies of the reaction Seeley *et al.,* (1996) and Howard (1979) at temperatures that pertain to the UTLS region. Furthermore, little attention has been focused on the pressure dependence of the reaction and Seeley *et al.,* (1996) suggested that a further study of the pressure dependence of the reaction would prove useful. This chapter reports on the results of a kinetic study of reaction (3.6) carried out over an extended temperature and pressure range.

Group	Temp. (K)	Press. (Torr)	Method	Rate coefficient
Simonaitis and Heicklen, 1973	298	800	Vis-UV Abs.	1.50×10^{-13}
Payne *et al.*, 1973	300	22.5—37.5	Theo.	3.01×10^{-13}
Simonaitis and Heicklen, 1974	298	352—900	Vis-UV Abs.	2.10×10^{-12}
Cox, 1975	300	760	GC	1.20×10^{-12}
Cox, and Derwent, 1975	296	760	Chem. Det.	1.20×10^{-12}
Glaenzer and Troe, 1975	1350—1700	760—1522	Theo.	7.47×10^{-12}
Hack *et al.*, 1975	298—670		ESR	3.55×10^{-13}
Simonaitis and Heicklen, 1976	296	640—760	Chem. Det.	1.00×10^{-12}
Howard and Evenson, 1977	296		LMR	8.10×10^{-12}
Simonaitis and Heicklen, 1977	245—328	760	Vis-UV Abs.	1.14×10^{-12}
Glaschick-Schimpf *et al.*, 1979	297	912	N-IR Det.	1.10×10^{-11}
Leu, 1979	270—425	2.5—5	Res. Flu.	8.81×10^{-12}
Burrows *et al.*, 1979	298		LMR	8.20×10^{-12}
Hack *et al.*, 1980	293	5—15	LMR	7.64×10^{-12}
Howard, 1979	232—403	1—1.5	LMR	7.71×10^{-12}
Thrush and Wilkinson, 1981	298	2	LMR	6.91×10^{-12}
Rozenshtein *et al.*, 1984	300	7—10	ESR	7.01×10^{-12}
Jemi-Alade andThrush, 1990	297	0.1—15	IR	8.50×10^{-12}
Seeley *et al.*, 1996	206—295	67—187	MS	8.03×10^{-12}
Bohn and Zetzsch, 1997	298	75—750	Vis-UV Abs.	9.60×10^{-12}

Table 3.1: Summary of the previous studies on reaction (3.6).

# 3.3 Experimental Set-Up for the Determination of the HO$_2$+NO Rate Coefficient

3.3.1 Experimental Design

A schematic diagram of the apparatus is shown in Figure 3.1. The flow tube was constructed from 22 mm id Pyrex tubing, the walls of which were coated with Halocarbon wax (Halocarbon Products inc.). A large flow of nitrogen (ranging from 50 to 130 STP litre min^{-1}) was injected at the rear of the flow tube. The flow tube was pumped by a rotary pump (Varian DS 1602). Pressure in the flow tube was in the of range 100 — 700 Torr depending on the experimental conditions.

The ion-molecule region was constructed from 22 mm id Pyrex tubing. A quadrupole mass spectrometer (ABB Extrel Merlin) was located at the end of the ion-molecule region. The TF-CIMS chamber pressure was maintained at around 2 Torr. The source region pressure in the mass spectrometer was 1×10^{-4} Torr and the analyser region pressure was held at around 9×10^{-6} Torr. All gas flows were monitored with calibrated mass flow meters (MKS). The pressures in the flow tube and the ion-molecule region were monitored using a 0 — 1000 Torr capacitance manometer (MKS Baratron).

The temperature within the flow tube was maintained within 2 K by placing the flow tube into an insulated chamber that was filled with dry ice. All temperatures were monitored by type K thermocouples. The flow tube temperature was maintained with heating tape (Omega, Heavy duty) regulated by an electronic controller (Carel Universal Infrared control type W) in conjunction with a thermocouple. The flow tube has five thermocouples along its length to monitor the temperature of the system. The nitrogen carrier gas was pre-cooled to the same temperature by passing it through a copper coil immersed in liquid nitrogen. The carrier gas temperature was maintained with heating tape (Omega, Heavy duty) regulated by an electronic controller (Carel Universal Infrared control type W) in conjunction with a thermocouple.
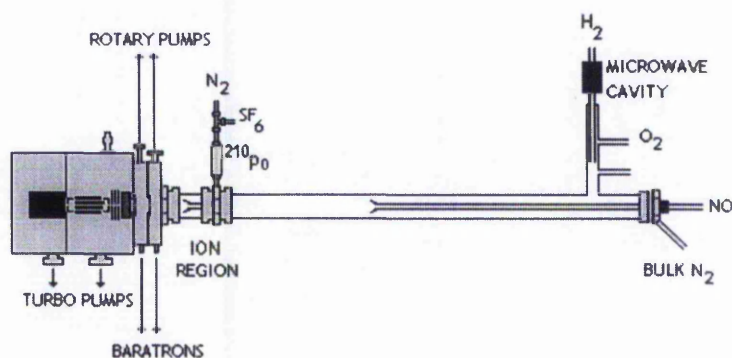
**Figure 3.1:** A schematic diagram of the TF-CIMS system.

3.2.2 HO$_2$ Generation

HO$_2$ was produced upstream of the flow tube *via* the reaction (3.9).

$$H \quad + \quad O_2 \quad + \quad M \quad \rightarrow \quad HO_2 \quad + \quad M \qquad R.3.9$$

Hydrogen atoms were produced by combining a 2.0 STP litre min^{-1} flow of He with a 0.1–3 STP cm^3 min^{-1} flow of 1% H$_2$, which was then passed through a discharge, produced by Surfatron microwave cavity (Sairem), operating at 75 W. To produce HO$_2$ radicals, the H atoms were injected into the flow tube *via* a side arm inlet located at the rear of the flow tube and mixed with a 1.0 STP litre min^{-1} flow of O$_2$. At the pressures and flow conditions used in this study, it is calculated that the H atoms have been completely titrated before entering the flow tube.

H atoms were periodically titrated with NO$_2$ to determine the concentration of H atoms produced. In the absence of oxygen, known amounts of NO$_2$ were added. The mass spectrometer signal (at m/e 46) was monitored with the microwave turned off and then turned on. Decrease in the NO$_2$ signal observed when the microwave was turned on was attributed to the reaction (3.10) as shown in Figure 3.2.

$$H \quad + \quad NO_2 \quad \rightarrow \quad NO \quad + \quad OH \qquad R.3.10$$
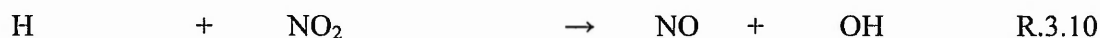
Using this method, it was found that on average 20% of H_2 was dissociated into H atoms. Under normal operating conditions the initial concentration of hydrogen atoms in the flow tube ranged from $1 - 10 \times 10^{10}$ molecules cm^{-3}
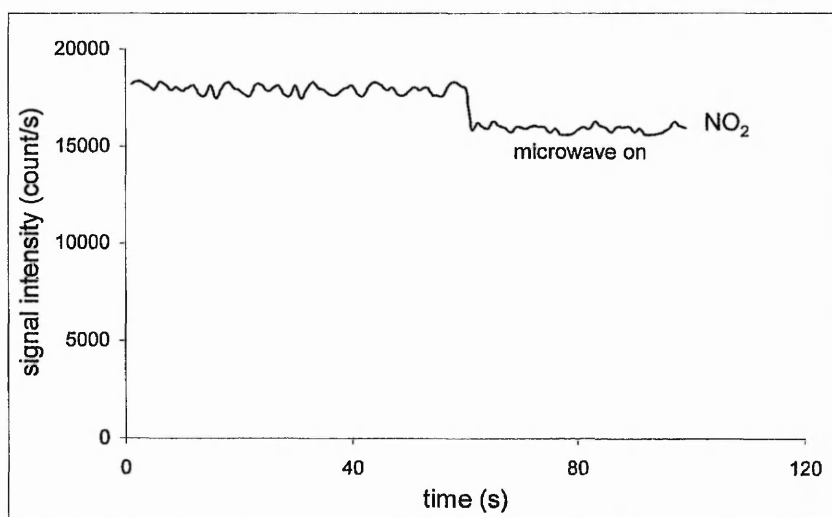
Figure 3.2: Single ion mode monitoring spectra showing the signal responses to the microwave activities.

3.3.3 Addition of NO

NO was introduced into the flow tube *via* the moveable injector by mixing a flow of 10% NO with a 1 STP litre min^{-1} flow of nitrogen. In all cases, [NO] >> [HO₂] so that pseudo-first-order conditions were maintained. Blank runs (in absence of NO) were carried out to ensure that the HO_2^- signal (m/e 140, *i.e.* $SF_4O_2^-$ Bardwell., *et al.,* 2003) was not affected by the movement of the injector.

3.3.4 Ionisation Schemes

NO_2, HO_2 and OH were chemically ionised using SF_6^- as the reagent ion. SF_6^- was generated by passing a 10 STP litre min^{-1} flow of N_2 through a ^{210}Po Nuclecel ionizer (NRD Inc.). The generated reagent ion was then carried into the ion-molecule region through an injector constructed from 6 mm od stainless steel. A fan-shaped turbulizer was attached to the end of the moveable inlet to enhance mixing of the reagent ion with the sampled flow from the flow tube. NO_2 and OH were ionised by SF_6^- *via* electron transfer enabling the species to be detected by their parent ions. HO_2 was detected as $SF_4O_2^-$ presumably through a multi step pathway, as reported by previous studies Seeley *et al.,* (1996). $SF_4O_2^-$ signal only appears when H atoms and O_2 are present, as shown in Figure 3.3.
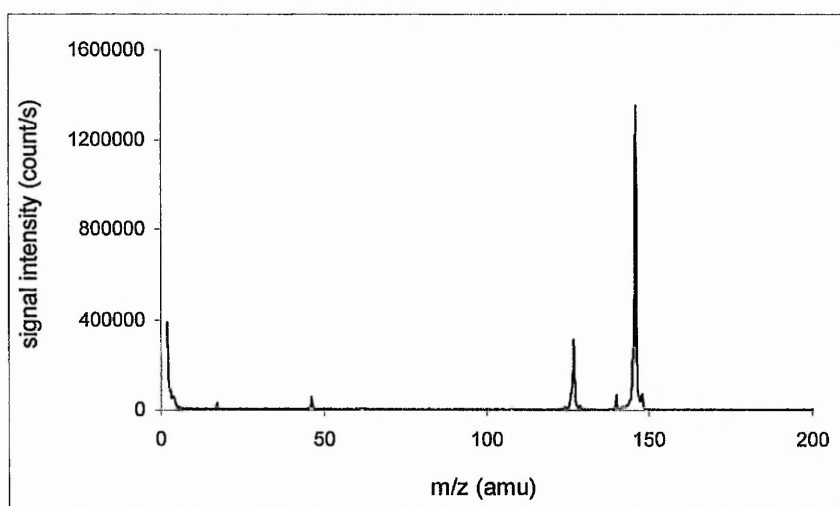
Figure 3.3: A mass spectrum of HO_2. HO_2 was detected as $SF_4O_2^-$.

As shown in Figure 3.4, the SF$_4$O$_2^-$ signal returns to background levels when any precursor gas flows (O$_2$ or H$_2$) are turned off or microwave discharge activities are stopped. This indicates that SF$_4$O$_2^-$ can only be attributed to the presence of HO$_2$ radicals.
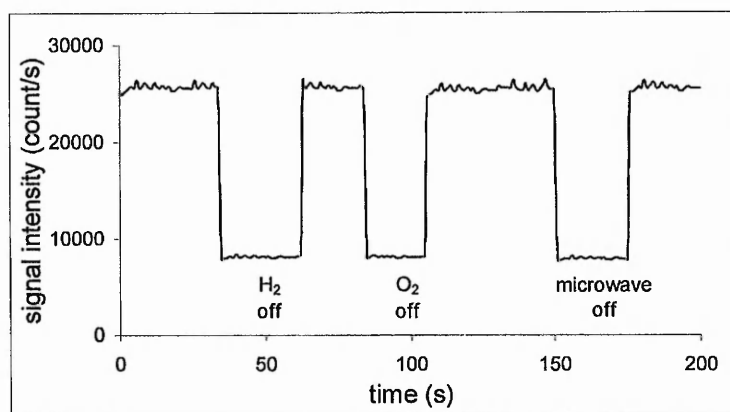
Figure 3.4: Single ion monitoring scan obtained during the peroxy radical identification experiments.

3.3.5 Materials

Nitric Oxide (NO) (Technical grade, Air Products) was purified by freeze-pump-thaw cycles, and selective freezing of Nitrogen dioxide (NO$_2$) impurities. NO$_2$ (99.9%, BOC) was purified by freeze thaw cycles in a O$_2$ rich atmosphere to remove NO impurities and gas mixtures were generated at 760 Torr pressure. Helium (CP Grade, BOC) before entering the Surfatron cavity was first passed through a gas clean oxygen filter (Chrompak) cartridge to remove traces of oxygen and then through a Gas clean moisture filter cartridge (Chrompak) to remove H$_2$O and finally a trap held at 77 K containing a molecular sieve (BDH, 4A). Hydrogen (H$_2$) (N5.0 cp grade 99.999%, BOC), Sulfurhexafluoride (SF$_6$) (99.99%, BOC) and nitrogen (N$_2$) and oxygen (O$_2$) (99.6%, BOC) were used as supplied.

3.4 Experimental Procedure

3.4.1 Detection Sensitivities

Dilute mixtures of NO$_2$ were injected *via* the moveable injector into the flow tube with no other gases present and the NO$_2^-$ signal was monitored. The sensitivity for NO$_2$ can be estimated from a linear plot of [NO$_2$] *vs.* NO$_2^-$ signal as shown in Figure 3.5. It is estimated that the sensitivity for NO$_2$ was 2×10^7 molecule cm^{-3} for a signal to noise ratio of one and a time constant of 1 s. The NO$_2$ concentrations were corrected to take into account equilibrium concentrations of N$_2$O$_4$ in the gas mixtures used. Under the experimental conditions the lifetime of N$_2$O$_4$ formed by the equilibrium as in reaction (3.11) is comparable with the time of mixing.

NO$_2$ + NO$_2$ + M $\rightleftharpoons$ N$_2$O$_4$ + M R.3.11

This assumption was corroborated by the fact that on the time scale of the experiment no change in [NO$_2$] was observed (Borrell *et al.,* 1988).
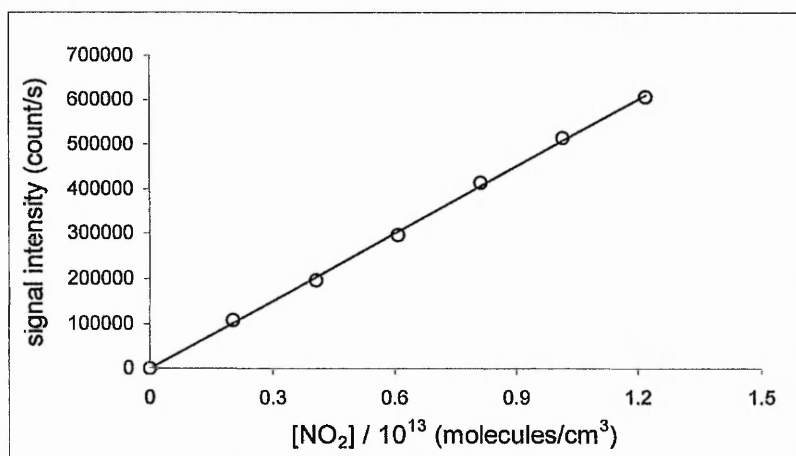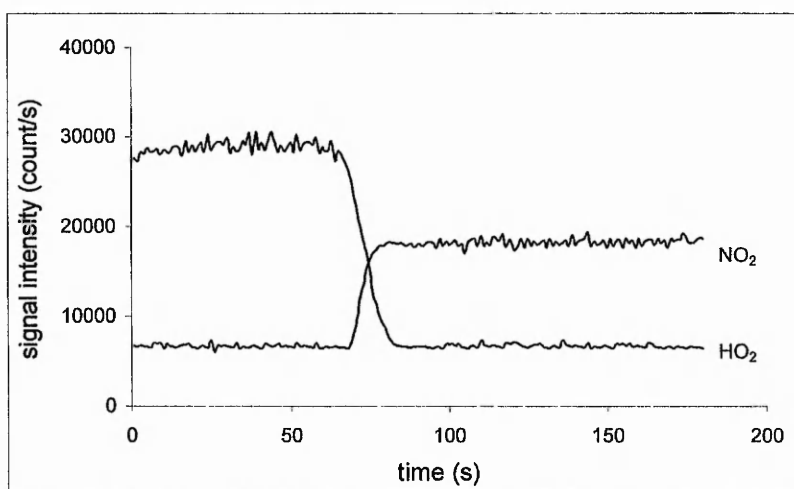

Figure 3.5: A sensitivity plot for NO$_2$ (sensitivity is equal to one over the slope).

3.4.2 Hydroperoxy Radical Calibration

Calibration of the HO$_2$ signal was achieved by adding a large excess of NO *via* the moveable injector at a constant contact time and by monitoring the resultant NO$_2$ formed by reaction with HO$_2$, as shown in reaction (3.12).

$$HO_2 \quad + \quad NO \quad \rightarrow \quad NO_2 \quad + \quad OH \qquad R.3.12$$

Sufficient NO was added to ensure complete removal of HO$_2$, confirmed by a constant NO$_2^-$ signal with further increasing [NO]. It is assumed that [NO$_2$]$_{observed}$ = [HO$_2$] as shown in Figure 3.6. This procedure was repeated for several different hydrogen atom concentrations and yielded a linear plot of HO$_2^-$ signal *vs.* [NO$_2$]$_{observed}$ as shown in Figure 3.7. It is estimated that the sensitivity for HO$_2$ was 1×10^7 molecule cm^{-3} for a signal to noise ratio of one and a time constant of 1 s.

Figure 3.6: Single ion mode monitoring spectra showing the signal responses during a HO$_2$ titration experiment.

Figure 3.7: The sensitivity plot for HO_2 (sensitivity is equal to one over the slope).

3.4.3 Hydroxyl Radical Calibration

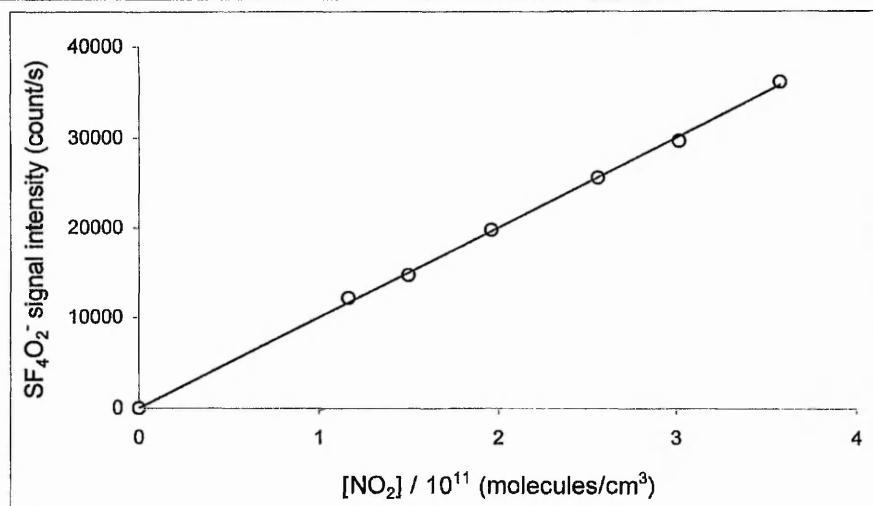To calibrate the OH sensitivity of the CIMS, hydrogen atoms were injected into the flow tube *via* a side arm inlet located at the rear of the flow tube in the absence of oxygen. Known amounts of NO_2 were added *via* the moveable injector and OH radicals were produced *via* the fast reaction (3.13) Canosa-Mas and Wayne, (1990).

$$H \quad + \quad NO_2 \quad \rightarrow \quad NO \quad + \quad OH \qquad R.3.13$$

Under the conditions where $[H] \gg [NO_2]$, the signal observed due to OH becomes independent of $[H]$. Using these conditions the mass spectrometer OH^- signal (at m/e 17) was monitored and recorded as a function of $[NO_2]$ for several different initial

concentrations of H atoms. At low concentrations of NO_2 the variation of OH signal S_{OH} is linear with $[NO_2]$ and a graph can be plotted, the slope of which is m_{exp} as shown in Figure 3.8. By carrying out the experiment at several different contact times the natural log of the m_{exp} slopes can be plotted on a graph as a function of contact time as shown in Figure 3.9. The exponential of the intercept of the ln m_{exp} against contact time graph shown in Figure 3.9 yields the calibration factor for OH. Using this method, the sensitivity for OH was detected to be 4×10^7 molecules cm^{-3} for a signal to noise ratio of one and a time constant of 1 s.
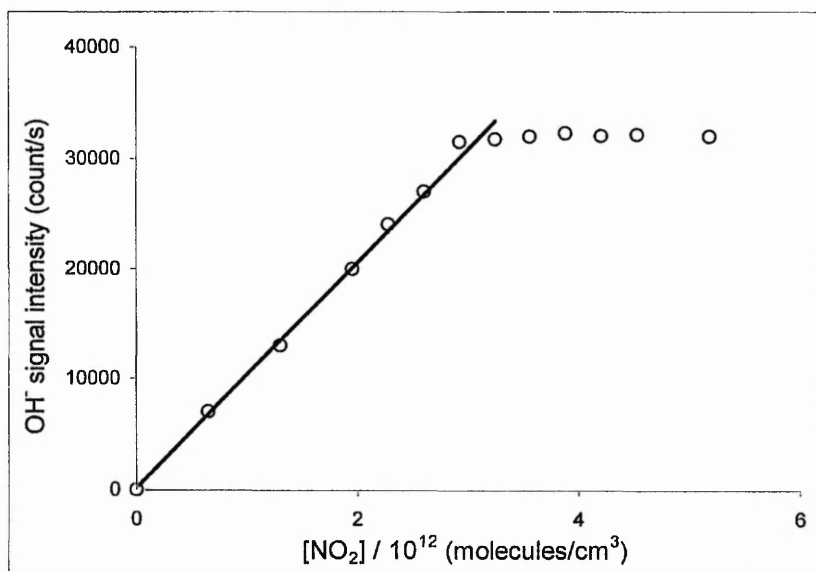
Figure 3.8: A plot of OH signal against $[NO_2]$ added the slope of which is m_{exp}.
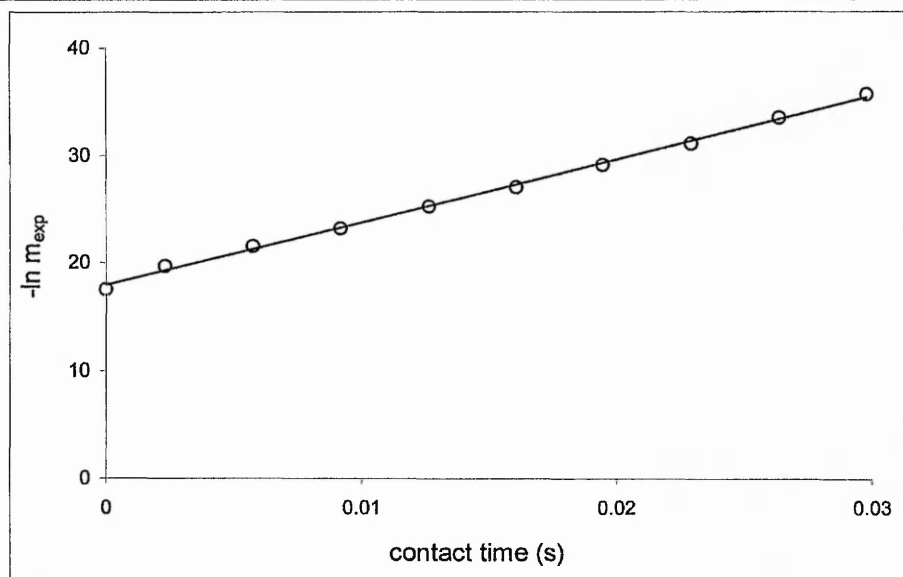
Figure 3.9: A plot of the slope of the natural logarithm of the slope of OH signal *vs.* [NO$_2$] as a function of contact time.

3.5 Room Temperature Rate Coefficient Determination

The rate coefficient for reaction (3.6) was measured by monitoring HO$_2$ concentration profiles at m/e = 140 (*i.e.* SF$_4$O$_2^-$) under pseudo-first-order conditions with [HO$_2$] = (1 – 10) × 10^{10} molecule cm^{-3} and [NO] = (1 – 12) × 10^{12} molecule cm^{-3}. First order decay rates (k_{1st}) were obtained by a linear regression of the plots of ln (HO$_2$ signal) *vs.* contact time as shown in Figure 3.10.
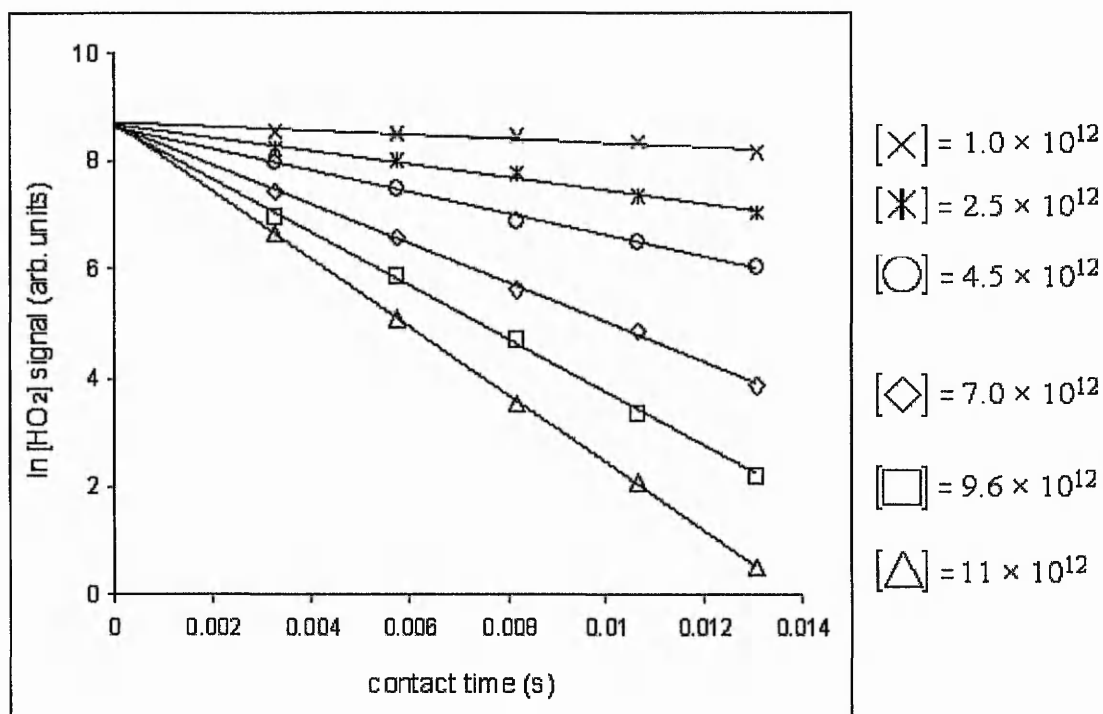
Figure 3.10: Pseudo-first-order decay profiles of SF$_4$O$_2^-$ as a function of contact time. Each slope corresponds to different concentrations of NO.

Each of these plots was essentially linear for all the experiments indicating the absence of any secondary chemistry effects. Non-linear fits of the plots of (HO$_2$ signal) *vs.* contact time were also carried out. Both methods yielded identical values of k_{1st} within experimental error. This process was repeated for at least ten different values of [NO] at each pressure studied. The values of k_{1st} were then plotted *vs.* [NO] as shown in figure 3.11.
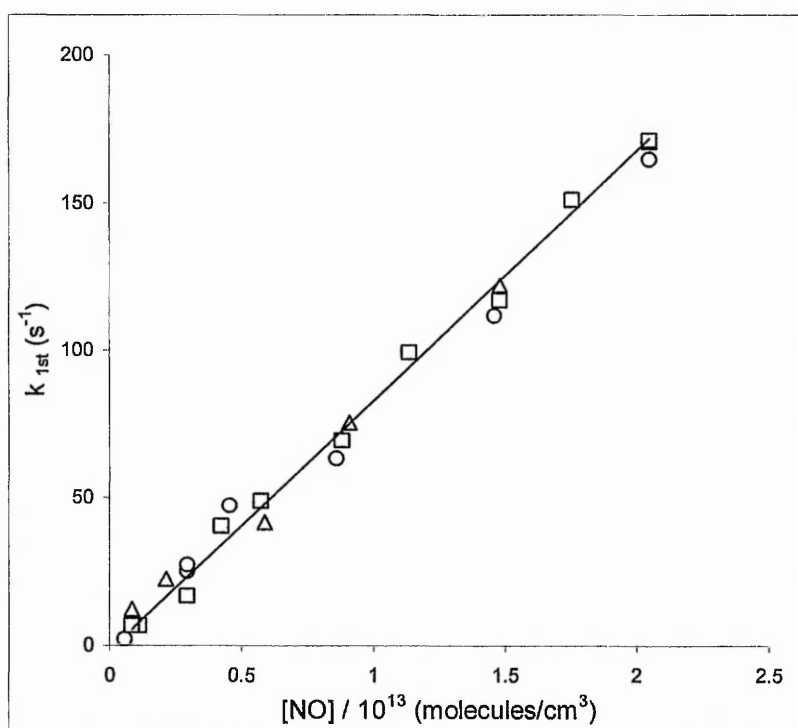
Figure 3.11: Pseudo-first-order rate coefficients plotted as a function of NO concentration. Data was obtained at 298 K and the plot presents the results of experiments at three different pressures Δ = 75 Torr $\square$ = 100 Torr $\circ$ = 200 Torr respectively.

These data points were fitted with a linear least squares routine, the slope of which provided the effective bimolecular rate coefficient, $k_{3.6}$. Table 3.2 lists the bimolecular rate coefficients obtained in this study. This approach for the determination of the effective bimolecular rate coefficient assumes that deviations from the plug flow approximation are negligible. Under the experimental conditions used, Seeley *et al.*, (1996) estimated that deviations from the plug flow approximation result in apparent rate coefficients that are at most 8% below the actual values. Hence, flow corrections were neglected, as they are smaller than the sum of other systematic experimental errors. All the data combined give an effective bimolecular rate coefficient at 298 K of $(8.44 \pm 0.15) \times 10^{-12}$ cm^3 molecule^{-1} s^{-1}, which is in agreement with previous studies by Seeley *et al.*, (1996), Howard, (1979), Howard and Evenson., (1977), Leu, (1979), Glaschick-Schimpf *et al.*, (1979), Hack *et al.*, (1980), Thrush and Wilkinson (1981) and Jemi-Alade and Thrush, (1990).

3.6 Sub - Ambient Rate Coefficient Determination

After the initial experimental studies conducted at 298 K, the rate coefficient of the reaction (3.6) was measured as a function of pressure and temperature. As the temperature was lowered from 300 K to 193 K the rate coefficient increased by approximately 65 %, which clearly indicates, that the rate of reaction (3.6) has a negative temperature dependence. The rate coefficient was determined as a function of pressure, however, there was no effect of pressure on the measured rate coefficient. Table 3.2 presents the data from temperature dependence experiments. From these data it is possible to create an Arrhenius type plot as shown in Figure 3.6 and carry out an Arrhenius type analysis of the temperature dependence of the rate coefficient.

Temperature (K)	Pressure (Torr)	$k_{3.6}$ (cm^3 molecule^{-1} s^{-1})
298	75	$(8.62 \pm 0.53) \times 10^{-12}$
298	100	$(8.57 \pm 0.11) \times 10^{-12}$
298	200	$(8.09 \pm 0.01) \times 10^{-12}$
253	100	$(9.53 \pm 0.43) \times 10^{-12}$
253	200	$(9.68 \pm 0.27) \times 10^{-12}$
223	100	$(1.04 \pm 0.31) \times 10^{-11}$
213	200	$(1.20 \pm 0.72) \times 10^{-11}$
193	100	$(1.28 \pm 0.01) \times 10^{-11}$
193	200	$(1.23 \pm 0.63) \times 10^{-11}$

Table 3.2: Experimentally determined rate coefficients for reaction (3.6) from sub-ambient studies.
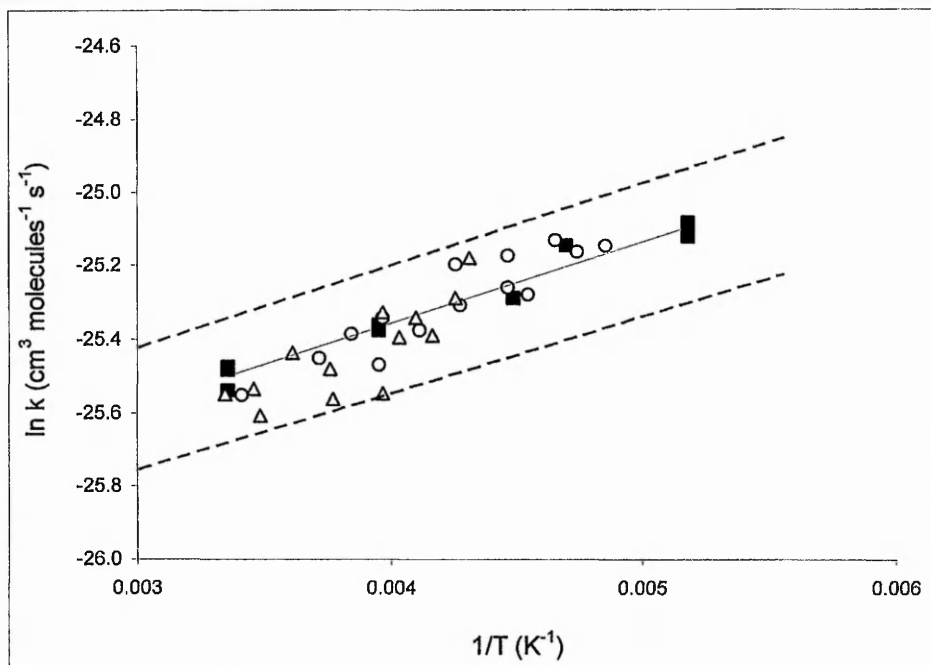
Figure 3.12: Arrhenius plot for reaction (3.6). The plot presents results from this work and those of two previous studies below 300 K. The solid line is the average of the all data points; the dashed line is equivalent to one standard deviation ■ data from this work, ○ data from Seeley *et al.,* (1996), Δ data from Howard (1979).

Arrhenius expression of k (T) = $(3.89^{+0.29}_{-0.27}) \times 10^{-12} \exp[(223 \pm 16.5)]$ cm³ molecule^{-1} s^{-1} the uncertainty is given at the one standard deviation level (apparent negative activation energy is observed). Other Two previous studies that carried out temperature dependence experiments on reaction (3.6) below 300 K are Seeley *et al.,* (1996) with a high-pressure flow tube system and Howard (1979) with a low pressure flow tube system. As it can clearly be seen in Figure 3.6 the data points show close agreement between all three studies.

3.7 Product Study

In order to assess the mass balance of reaction (3.6), product studies were performed at all temperatures and pressures studied. Under all conditions studied, even at the longest contact times, no other peaks were observed apart from SF_6^-, SF_5^-, NO_2^-, $SF_4O_2^-$ and OH^-, as shown in Figure 3.13. The curve passing through the HO$_2$ is the experimentally determined first order loss rate and NO$_2$ assumes 100 % formation of NO$_2$ and thus a first order appearance of reactants. OH signal decays as a function of contact time as a consequence of the secondary reaction with NO

$$OH \quad + \quad NO \quad + \quad M \quad \rightarrow \quad HONO \quad + \quad M \qquad R.3.14$$

The curve passing through the OH signal is based on the combination of the rate of production of OH from reaction (3.6) and the rate loss of OH from reaction (3.14). Over the temperature and pressure range studied there was no evidence, within experimental error, for the formation of any stabilised adducts or secondary product channels, *i.e.* it can be assumed that the reaction proceeds $100 \pm 5\%$ *via* the formation of OH and NO$_2$.
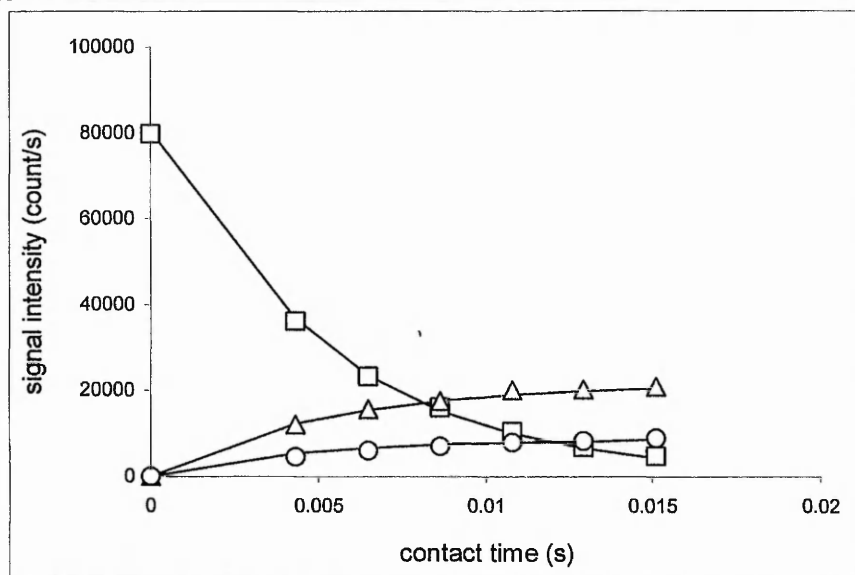
Figure 3.13: Signal intensity as a function of injector position □ HO$_2$, ○ OH and △ NO$_2$ the curve fitted to the NO$_2$ and HO$_2$ data is calculated for a first order appearance and decay of products and reactants respectively.

3.8 Mechanism

The rate coefficient of reaction (3.6) displays a significant negative temperature dependence. This implies that reaction (3.6) is an example of a complex mode reaction, *i.e.* the reaction proceeds *via* multiple transition states. The reactants pass over the energy barrier and form the intermediate reaction (3.15). The intermediate could then re-dissociate back to reactants reaction (3.16), proceed *via* a further transition state and undergo bond fission to yield products reaction (3.17) or collisional stabilization reaction (3.18).

HO$_2$	+	NO	$\rightarrow$	[HO$_2$NO]*			R.3.15
[HO$_2$NO]*			$\rightarrow$	HO$_2$	+	NO	R.3.16
[HO$_2$NO]*			$\rightarrow$	OH	+	NO$_2$	R.3.17
[HO$_2$NO]*	+	M	$\rightarrow$	HO$_2$NO	+	M	R.3.18
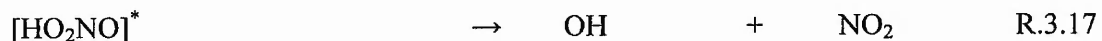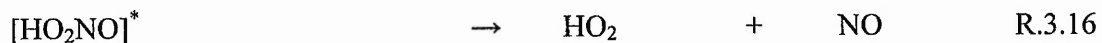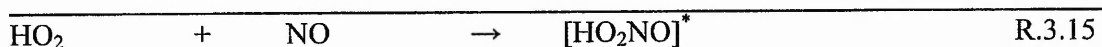
The absence of any experimentally observed pressure dependence, which is in agreement with the low pressure rate coefficients reported by Howard (1979), suggest that the [HO$_2$NO]* intermediate is too short lived to be affected by collisions with the bulk N$_2$ gas even at the extended temperatures and pressures of this study.

Chakraborty *et al.*, (1998) recently carried out an extensive theoretical study of the reaction between OH and NO$_2$ and considered both the channel forming HONO$_2$ and HO$_2$NO. These workers have also explored reaction (3.6) in detail as a result of their study and compared RRKM predictions with available kinetic data at that time. It is clear from the work of Chakraborty *et al.*, (1998) that the HO$_2$NO would not be stabilised at the pressures studied in this work.

Simple calculations based on QRRK theory using the thermodynamic data from Chakraborty *et al.*, (1998) confirm that several atmospheres pressure would be required to stabilise the adduct. These calculations show that once the energised adduct is formed; it almost exclusively decomposes *via* simple bond fission to yield OH and NO$_2$. Re-dissociation and stabilisation of the intermediate are both inefficient processes in comparison.
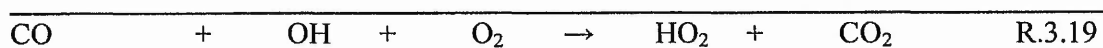
Several points should be noted. First, the product channel to form OH and NO$_2$ should dominate on thermodynamic grounds since the reaction is exothermic. Second, the calculations suggest that the rate-determining step for reaction (3.6) is actually reaction (3.14), *i.e.* how quickly the HO$_2$NO intermediate formed. Third as the re-dissociation reaction is negligible at all pressures over the temperature range studied, the rate coefficient cannot be pressure dependent for reaction (3.6); which is in good agreement with the experimentally observed rate coefficients of both this work and that of Seeley *et al.,* (1996). Fourth, the rate coefficient for reaction (3.6) might be expected to decrease with increasing temperature, because the re-dissociation of the HO$_2$NO could begin to compete with Channel 3.16; which is agreement with the experimentally observed apparent "negative" activation energy. Finally, these calculations suggest that the HO$_2$NO intermediate would not be stabilised, even at extremely high pressures; which is in agreement with the product studies carried out in this work, *i.e.* no evidence for the formation of any other products other than OH and NO$_2$.

3.9 Atmospheric Implications

The importance of reaction (3.6) for the *in situ* production of ozone in the troposphere is well known. It is therefore extremely important to characterise the rate coefficients for such reactions over a wide range of pressure and temperature. Field *et al.,* (2001) have noted the importance of reaction (3.6) in an autocatalytic production of OH.

CO	+	OH	+	O$_2$	$\rightarrow$	HO$_2$	+	CO$_2$	R.3.19
HO$_2$	+			NO	$\rightarrow$	OH	+	NO$_2$	R.3.6
NO$_2$	+			hν	$\rightarrow$	NO	+	O	R.3.7
O	+	O$_2$	+	M	$\rightarrow$	O$_3$	+	M	R.3.8
O$_3$	+			hν	$\rightarrow$	O$_2$	+	O (^{1}D)	R.3.1
O (^{1}D)	+			H$_2$O	$\rightarrow$	OH	+	OH	R.3.2

Net: CO + 2hν + H$_2$O + O$_2$ $\rightarrow$ 2OH + CO$_2$

Therefore model sensitivity studies have been performed, using CiTTy CAT, a tropospheric trajectory model. The model was run for a variety of scenarios, replicating those conditions prescribed in the Photochemistry-Intercomparison Exercise. Details of the initial conditions and model scenarios used can be found in the summary paper by Olson *et al.,* (1997) and are summarized in Table 3.3. Essentially, the model was run under three surface scenarios, clean marine, background continental and urban conditions, and two scenarios away from the surface, a polluted plume at 4 km and a clean air scenario at 8km.

Initial conditions	Marine	Continental	Free	Plume
Altitude (km)	0	0	8	4
Temperature	288.15	288.15	236.21	262.17
Pressure (m bar)	1013.25	1013.25	356.20	616.20
Number density (cm^{-3})	2.55×10^{19}	2.55×10^{19}	1.09×10^{19}	1.70×10^{19}
H$_2$O % v/v	1.0	1.0	0.05	0.25
O$_3$ ppb	30	30	100	50
NO$_x$ ppb	10	200	100	10.000
HNO$_3$ ppb	100	100	100	100
CO ppb	100	100	100	600
CH$_4$ ppb	1700	1700	1700	1700

Table 3.3: Model scenarios conditions.

These five scenarios were originally chosen for the intercomparison to cover the range of NO$_x$/VOC encountered in the troposphere and its influence on ozone production and destruction. The CiTTy CAT model contains a detailed chemistry scheme with 13 non-methane hydrocarbons and for each scenario the model was integrated forward in a box model mode for five days. Three integrations were performed for each of the five atmospheric conditions described, a base case where the central Arrhenius parameters were used, a "high" $k_{3.6}$ case, where the largest A factor and lowest E$_a$, within measurement error in this study were used and a "low" $k_{3.6}$ case, where the smallest A factor and highest E$_a$, within measurement error in this study were used. Comparisons between each set of three integrations were then made for a range of species, and those with the most significant impact being O$_3$, OH, HO$_2$, NO and NO$_2$ as shown in Figure 3.14. In all cases, within the experimental error of this study, model O$_3$ did not deviate by more than 1%. At low model NO$_x$ (less than a few ppb) OH varies by 2% (increasing with high $k_{3.6}$) and at 5 ppb NO$_x$, the variation in OH has risen to just over 4% at all altitudes. HO$_2$ is slightly more sensitive to $k_{3.6}$ as one would expect, decreasing in concentration in the model with a rise in $k_{3.6}$.
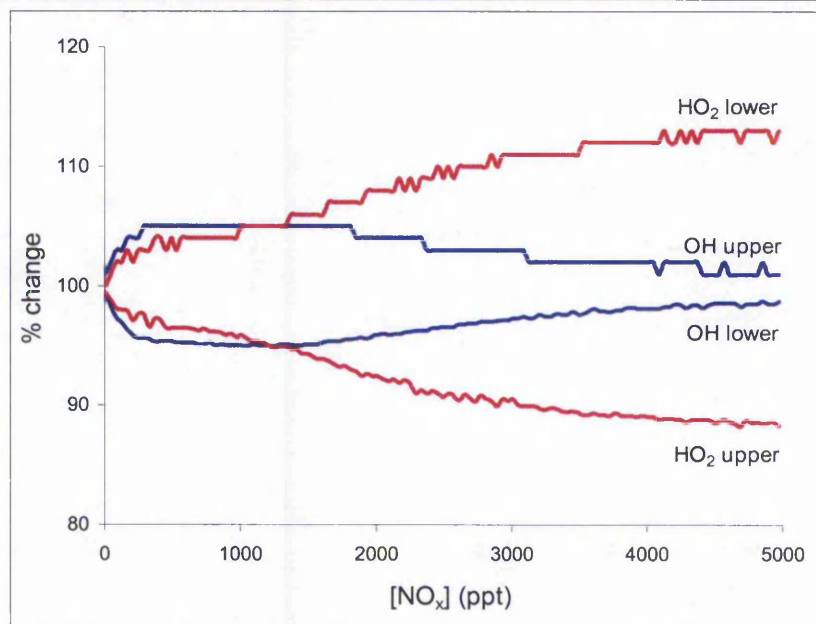
Figure 3.14: A sensitivity plot for HO$_x$ production at 8 km.

At the surface HO$_2$ varies from 1 — 5% as NO$_x$ increases up to around 5 ppb. However, at 8 km, at the very highest NO$_x$ (5 ppb), HO$_2$ varies by as much as 12%. NO itself varies (decreasing with a higher $k_{3.6}$) from 3 — 6% at the surface and up to 12% at 8 km, whilst NO$_2$ varies by 7% at most at all altitudes. It is concluded that the impact of the experimental error in the measurement of $k_{3.6}$ in this study has an insignificant effect on modelled species concentrations in the troposphere, although it is noted that at high NO$_x$ levels, both HO$_2$ and NO vary by more than 10% when using the extreme values of $k_{3.6}$ The discrepancy between model and measured HO$_x$ in the UT cannot be explained by experimental errors in $k_{3.6}$.

3.10 Conclusions

Our data indicates that reaction (3.6) has significant negative temperature dependence, as suggested by previous studies of the reaction (Seeley *et al.,* 1996; Howard, 1979). The results presented in this chapter represent an extension in the range of temperatures over which reaction (3.6) has been studied experimentally. Our results are in excellent agreement with extrapolations to 193 K based on previous higher temperature measurements extrapolated to 193 K. The negative temperature dependence of the rate coefficient for reaction (3.6) suggests that it proceeds through the formation of an energised intermediate $[HO_2NO]^*$. Over the temperature range studied, the rate coefficient for reaction (3.6) was found to be invariant with pressure. In conjunction with product studies and theoretical calculations, our results suggest that the $[HO_2NO]^*$ intermediate is too short lived to be affected by collisions and it exclusively decomposes *via* simple bond fission to yield OH and NO_2. Atmospheric model sensitivity studies, using a tropospheric trajectory model, were performed to assess the impact of the experimental errors of reaction (3.6) on tropospheric O_3 production. It was found that within the experimental error of the studies, model O_3 did not deviate by more than 1%. The model sensitivity study suggests that the uncertainty associated with the rate parameters for reaction (3.6) will have only a minor impact on the evolution of chemical species in atmospheric models.

References

Bardwell, M.W.; Bacak, A.; Raventos, M.T.; Sanchez-Reyna, G.; Shallcross, D.E.; Percival, C.J., *Phys. Chem. Chem. Phys.*, 2003, **5**, 2381

Bohn, B.; Zetzsch, C., *J. Phys. Chem.* A, 1997, **101**, 1488

Borrell, P.; Cobos C. J.; Luther, K., *J. Phys. Chem.*, 1988, **92**, 4377

Burrows, J.P.; Cliff, D.I.; Harris, G.W.; Thrush, B.A.; Wilkinson, J.P.T., *Proc. R. Soc. London* A, 1980, **368**, 463

Chakraborty, D; Park, J. and Lin, M.C., *J. Chem. Phys.*, 1998, **231**, 39

Canosa-Mas, C. E. and Wayne, R. P., *Int. J. Chem. Kinet.*, 1990, **22**, 829

Cox, R.A., *Proc. Symp. Chem. Kinet. Data Upper Lower Atmos.*, 1975, **1974**, 379

Cox, R.A.; Derwent, R.G., *J. Photochem.*, 1975, **4**, 139

Elrod, M. J.; Meads, R. F.; Lipson, J. B.; Seeley, J. V.; Molina, M. J., *J. Phys. Chem.*, 1996, **100**, 5808

Field, R.J.; Hess, P.G.; Kalachev, L.V.; Madronich, S., *J. Geophys. Res.*, 2001, **106**, 7553

Finlayson-Pitts, B.J.; Pitts, J.N., *Atmospheric Chemistry*, John-Wiley and Sons, New York, 1986

Glaenzer, K.; Troe, J., *Ber. Bunsenges. Phys. Chem.,* 1975,**79,** 465

Glaschick-Schimpf, I.; Leiss, A.; Monkhouse, P.B.; Schurath, U.; Becker, K.H.; Fink, E.H.; Dursunoglu, C.; *Chem. Phys. Lett.*, 1979, **67**, 318

Hack, W.; Hoyermann, K.; Wagner, H.G., *Proc. Symp. Chem. Kinet. Data Upper Lower Atmos.,* 1975, **1974,** 329

Hack, W.; Preuss, A.W.; Temps, F.; Wagner, H.G.; Hoyermann, K.; Nas, D., *Int. J. Chem. Kinet.,* 1980, **12**, 851

Howard, C.J., *J. Am. Chem. Soc.*, 1980, **102**, 6937

Howard, C.J., *J. Chem. Phys.,* 1979, **71**, 2352

Howard, C.J.; Evenson, K.M., *Geophys. Res. Lett.*, 1977, **4,** 437

Jemi-Alade, A.A.; Thrush, B.A., *J. Chem. Soc. Faraday Trans.*, 1990, **86**, 3355

Leu, M.T., *J. Chem. Phys.*, 1979, **70,** 1662

Olson, J.; Prather, M.; Bernsten, T.; Carmichael, G.; Chatfield, R.; Cannell, P.; Derwent, R.; Horrowitz, L.; Jin, S.; Kanakidou, M.; Kasibhatla, P.; Kotomarthi, R.; Kuhn, M.; Law, K.; Penner, J.; Perliski, L.; Sillman, S.; Stordal, F.; Thompson, A.; Wild, O., *J. Geophys. Res.*, 1997, **102**, 5979

Payne, W.A.; Stief, L.J.; Davis, D.D., *J. Am. Chem. Soc.*, 1973, **95**, 7614

Rozenshtein, V.B.; Gershenzon, Yu.M.; Il'in, S.D.; Kishkovitch, O.P., *Chem. Phys. Lett.*, 1984, **112**, 473

Salawitch, R.S.; Wennberg, P.O.; Geoffrey C.T.; Sen B.; Blavier, J.F., *Geophys. Res. Lett.*, 2002, **29**, 9

Seeley, J.V.; Meads, R.F.; Elrod, M.J.; Molina, M.J., *J. Phys. Chem.*, 1996, **100**, 4026

Simonaitis, R.; Heicklen, J., *J. Phys. Chem.*, 1973, **77**, 1096

Simonaitis, R.; Heicklen, J., *J. Phys. Chem.*, 1974, **78**, 653

Simonaitis, R.; Heicklen, J., *J. Phys. Chem.*, 1976, **80**, 1

Simonaitis, R.; Heicklen, J., *NASA Contract. Rep.*, 1977, 1

Thrush, B.A.; Wilkinson, J.P.T., *Chem. Phys. Lett.*, 1981, **81**, 1

Wayne, R. P., *Chemistry of Atmospheres*, 3rd edn., Oxford University Press, Oxford, 2000

Wennberg, P.O.; Salawitch, R.J.; Donaldson, D.J.; Hanisco, T.F.; Lanzendorf, E.J.; Perkins, K.K.; Lloyd, S.A.; Vaida, V; Gao, R.S.; Hintsa, E.J.; Cohen, R.C.; Swartz, W.H.; Kusterer, T.L.; Anderson, D.E., *Geophys. Res. Lett.*, 1998, **26**, 1373

Chapter 4

Kinetics of the Reaction Between HO$_2$ and NO$_2$

4.1. Introduction

Reaction of HO$_x$ (OH and HO$_2$) and NO$_x$ (NO and NO$_2$) affect atmospheric composition and climate by governing the global tropospheric ozone budget. The reaction of HO$_2$ with NO$_2$ leads to the formation of Peroxynitric acid (PNA), as shown in reaction (4.1).

$$HO_2 \quad + \quad NO_2 \quad + \quad M \quad \rightarrow \quad HO_2NO_2 \quad + \quad M \qquad R.4.1$$

The above reaction couples both HO$_x$ and NO$_x$ chemical families and thus influencing tropospheric ozone production and the OH budget in both the troposphere and stratosphere. The importance of PNA formation increases at temperatures below 240 K, because HO$_2$NO$_2$ is weakly bound ($\sim$ 95 kJ mol^{-1}) (Murphy *et al.*, 2003) and rapidly dissociates at higher temperature. Consequently reaction (4.1) is most important in the stratosphere and upper troposphere.

Reaction 4.1 has also been suggested to play important role in the atmospheric HO$_x$ budget through the following mechanism

$$HO_2 \quad + \quad NO_2 \quad + \quad M \quad \rightleftharpoons \quad HO_2NO_2 \quad + \quad M \qquad R.4.1$$

$$HO_2NO_2 \quad + \quad OH \quad \rightarrow \quad H_2O \quad + O_2 \ + \quad NO_2 \qquad R.4.2$$

Net: $\quad OH \ + \ HO_2 \ \rightarrow \ H_2O \quad + \quad O_2 \qquad R.4.3$

leading to the catalytic destruction of HO$_x$ (Salawitch *et al.*, 2002).

Remote sensing measurements of PNA (Rinsland *et al.*, 1996; Rinsland *et al.*, 1986 and Sen *et al.*, 1998) indicate that the PNA mixing ratio peak at 200 ppt near 27 km. However, there is little *in situ* data on PNA concentrations. Slusher *et al.*, (2001) measured surface Antarctic PNA using chemical ionisation mass spectrometry and observed mixing ratios on the order of 20 ppt. More recently, Murphy *et al.*, (2003) have measured PNA concentrations using thermal dissociation laser induced fluorescence and have estimated that PNA constitutes up to 20% of upper tropospheric NO_y in mid and polar latitudes. Recently Wennberg *et al.*, (1999) have reported that the photolysis of HO_2NO_2 is an important source of HO_x species under high latitude and high solar zenith angle conditions. Therefore, accurate measurements of $k_{4.1}[M,T]$, the effective bimolecular rate coefficient for the reaction (4.1), are vital to predict HO_2NO_2 concentrations and correctly describe the chemistry of this region of the atmosphere.

4.2. Previous Experimental Studies on the Reaction of $HO_2 + NO_2$

Previous works on reaction (4.1) is summarized in Table 4.1; there have been numerous studies of the reaction at room temperature. The studies have been performed over a wide range of pressures and are in fair agreement; therefore reaction (4.1) is well characterized at room temperature. But despite the importance of the reaction (4.1) for the upper troposphere there have only been limited experimental studies (Kurylo and Ouellette, 1987; Sander and Peterson, 1984 and Christensen *et al.*, 2004) at temperatures that pertain to the upper troposphere region. There is a clear need for a more systematic study of the reaction to be undertaken and the result of such a study will be the focus of this chapter.

Group	Temp (K).	Press. (Torr)	Method	k [M,T]
Simonaitis and Heicklen, 1974	298	0.007—0.3	FP-Dual B.	3.00×10^{-13}
Simonaitis and Heicklen, 1976	296	100—730	Chem. Det.	9.80×10^{-14}
Levine *et al.,* 1977	298	700	FTIR	1.36×10^{-13}
Howard, 1977	300	0.5—3	FT-LMR	1.62×10^{-12}
Baldwin and Golden, 1977	217—300	200	Theo.	7.05×10^{-13}
Cox and Patrick, 1979	283	25—600	FP-UV Abs.	1.50×10^{-12}
Patrick and Golden, 1983	300		Theo.	2.30×10^{-31}
Sander and Peterson, 1984	229—362	50—700	FP-UV Abs.	4.62×10^{-13}
Kurylo and Ouellette, 1986	298	25—600	FP-Kin. Abs.	5.50×10^{-12}
Kurylo and Ouellette, 1987	228—358	25, 50, 100	FP-UV Abs.	4.70×10^{-12}
Alade and Thrush, 1990	275—326	1.5—10	mIR LMR	4.83×10^{-13}
Aloisio and Francisco, 2000		200	Theo	1.8×10^{-13}
Dransfield *et al.,* 2001	230		FTIR	
Christensen *et al.,* 2004	220—298	45—200	nIR UV V. Abs	5.34×10^{-13}

Table 4.1: Summary of the previous studies has been done on reaction (4.1).

## 4.3 Experimental Set-Up for the Determination of the HO$_2$+NO$_2$ Rate Coefficient

4.3.1. Experimental Design

A schematic diagram of the apparatus is shown in Figure 4.1. The flow tube was constructed from 22 mm id Pyrex tubing, the walls of which were coated with Halocarbon wax (Halocarbon Products inc.). A large flow of nitrogen (ranging from 50 to 130 STP litre min^{-1}) was injected at the rear of the flow tube. The flow tube was pumped by a rotary pump (Varian DS 1602). Pressure in the flow tube was maintained in the range 100 – 700 Torr depending on experimental conditions. A portion of the gas in the flow tube was sampled into the ion-molecule region *via* an aperture (2 mm). The ion-molecule region was constructed from 22 mm id Pyrex tubing and was pumped by a mechanical pump (Varian, DS 402) and maintained at a pressure of 50 Torr. A quadrupole mass spectrometer (ABB, Extrel Merlin) was located at the end of the ion-molecule region. The TF-CIMS chamber pressure was maintained at around 2 Torr. The source region pressure in the mass spectrometer was 1×10^{-4} Torr and the analyser region pressure was held at around 9×10^{-6} Torr. All gas flows were monitored with calibrated mass flow meters (MKS). The pressures in the flow tube and the ion-molecule region were monitored using a 0 – 1000 Torr capacitance manometer (MKS, Baratron).

The temperature within the flow tube was maintained within 2 K by placing the flow tube into an insulated chamber that was filled with dry ice. All temperatures were monitored by type K thermocouples. The flow tube temperature was maintained with heating tape (Omega, Heavy duty) regulated by an electronic controller (Carel Universal Infrared control type W) in conjunction with a thermocouple. The flow tube has 5 thermocouples along its length to monitor the temperature of the system. The nitrogen carrier gas was pre - cooled to the by passing it through a copper coil immersed in liquid nitrogen. The carrier gas temperature was maintained with heating tape (Omega, Heavy duty) regulated by an electronic controller (Carel Universal Infrared control type W) in conjunction with a thermocouple.
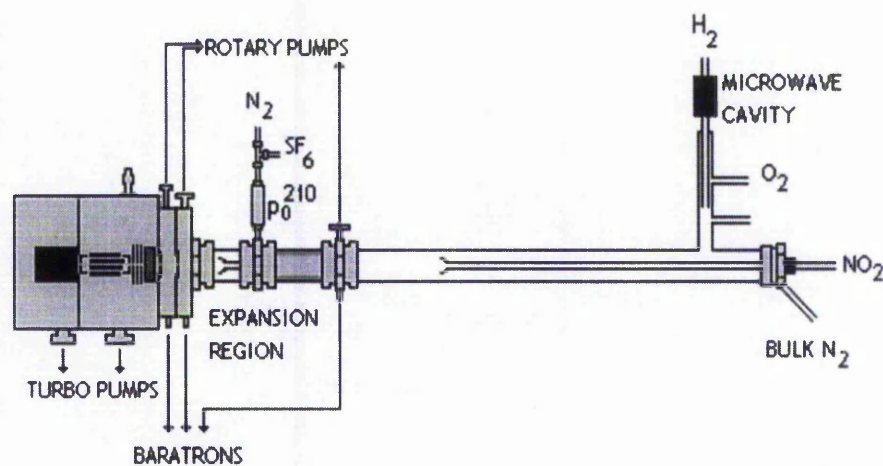
Figure 4.1: A schematic diagram of Flow Tube Chemical Ionisation Mass Spectrometry system.

4.3.2 HO$_2$ Generation

HO$_2$ was produced upstream of the flow tube *via* the reaction (4.4).

$$H \quad + \quad O_2 \quad + \quad M \quad \rightarrow \quad HO_2 \quad + \quad M \qquad R.4.4$$

Hydrogen atoms were produced by combining a 2.0 STP cm^3 min$^-$1 flow of He with a 0.1 to 3 STP cm^3 min^{-1} flow of 1% H$_2$, which was then passed through a microwave discharge produced by Sairem Surfatron cavity, operating at 75 W. To produce HO$_2$ radicals, the H atoms were injected into the flow tube *via* a side arm inlet located at the rear of the flow tube and mixed with a 1.0 STP cm^3 min^{-1}flow of O$_2$. At the pressures and flow conditions used in this study, it is calculated that the H atoms have been completely titrated before entering the flow tube.

H atoms were periodically titrated with NO$_2$ to determine the concentration of H atoms produced. In the absence of oxygen, known amounts of NO$_2$ were added. The mass spectrometer signal (at m/e 46) was monitored with the microwave turned off and then turned on. The decrease in the NO$_2$ signal observed when the microwave turned on was attributed to reaction (4.5) as shown in Figure 4.2.

$$H \quad + \quad NO_2 \quad \rightarrow \quad NO \quad + \quad OH \qquad R.4.5$$
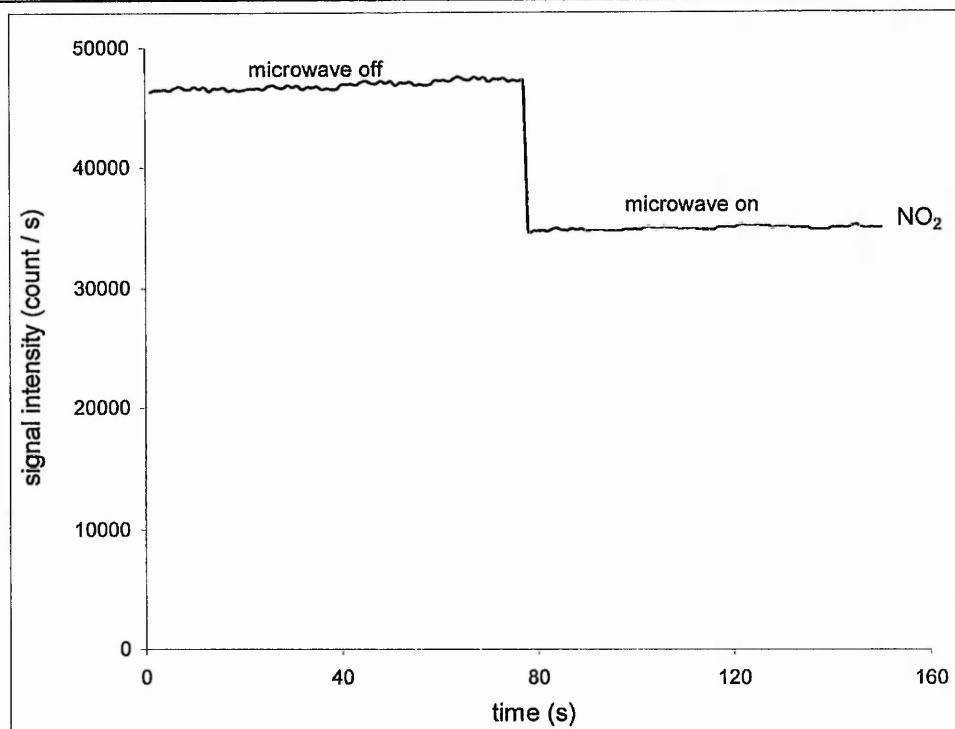
Figure 4.2: Single ion mode monitoring spectra showing the signal responses to the microwave activities

Using this method it was found that average 20% of H$_2$ was dissociated into H atoms. Under normal operating conditions the initial concentration of hydrogen atoms in the flow tube ranged from $(1 - 10) \times 10^{10}$ molecules cm^{-3}

4.3.3 Addition of NO$_2$

NO$_2$ was introduced into the flow tube *via* the moveable injector by mixing a flow of 10% NO$_2$ with a 1 STP cm^3 min^{-1} flow of nitrogen. In all cases, [NO$_2$] >> [HO$_2$] so that pseudo-first-order conditions were maintained. Blank runs (with no NO$_2$ flowing) were carried out to ensure that the HO$_2^-$ signal (m/e 140, *i.e.* SF$_4$O$_2^-$ Bardwell, *et al.*, 2003) was not affected by movement of the injector.

4.3.4 Ionisation Schemes

NO$_2$, HO$_2$ and HO$_2$NO$_2$were chemically ionised using SF$_6^-$ as the reagent ion. SF$_6^-$ was generated by passing a 10 STP cm^3 min^{-1} flow of N$_2$ through a Po ^{210} Nuclecel ionizer (NRD Inc.). The generated reagent ion was then carried into the ion molecule region through an injector constructed from 6 mm od stainless steel. A fan shaped turbulizer was attached to the end of the moveable inlet to enhance mixing of the reagent ion with the sampled flow from the flow tube. NO$_2$ and HO$_2$NO$_2$ were ionised by SF$_6^-$ *via* electron transfer enabling the species to be detected by their parent ions. HO$_2$ was detected as SF$_4$O$_2^-$ presumably through a multi step pathway, as reported by previous studies.
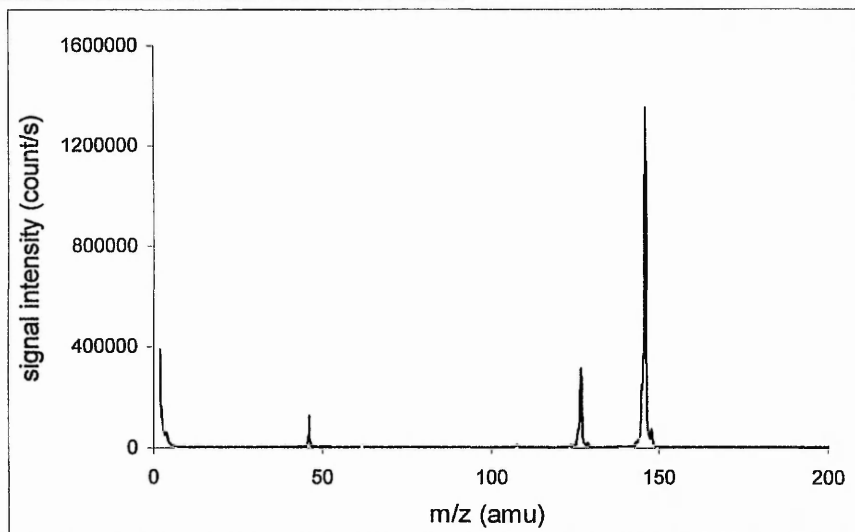
Figure 4.3: A spectral scan obtained after the addition of 1 STP cm^3 min^{-1} NO$_2$.
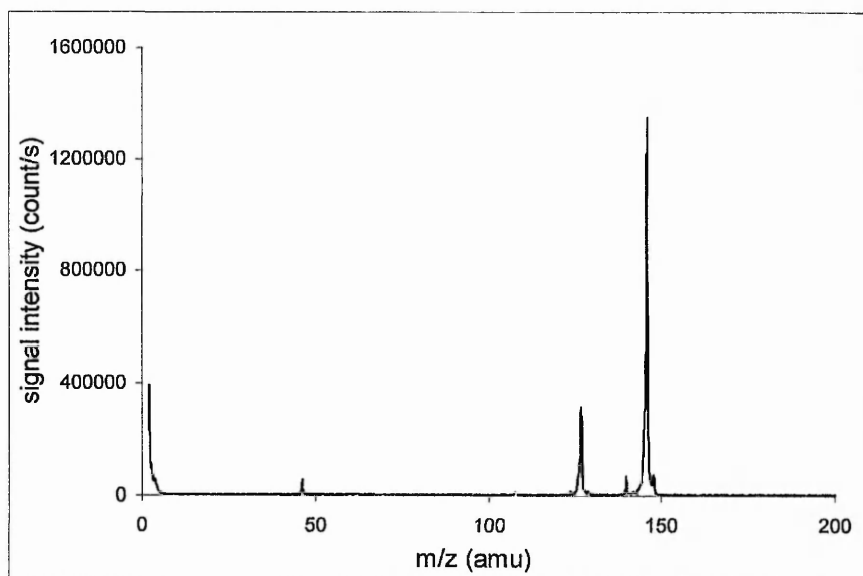
Figure 4.4: A spectral scan obtained after the creation of HO$_2$. Radical was detected as SF$_4$O$_2^-$ m/e 140 (Bardwell *et al.*, 2003).

$SF_4O_2^-$ signal only appears when H atoms, and O_2 are present. The appearance of $SF_4O_2^-$ signal was shown in Figure 4.4. As seen in figure 4.5 the $SF_4O_2^-$ signal returns to background levels when any precursor gas flows (O_2 or H_2) were turned off. This indicates that $SF_4O_2^-$ can only be attributed to the presence of HO_2 radicals.
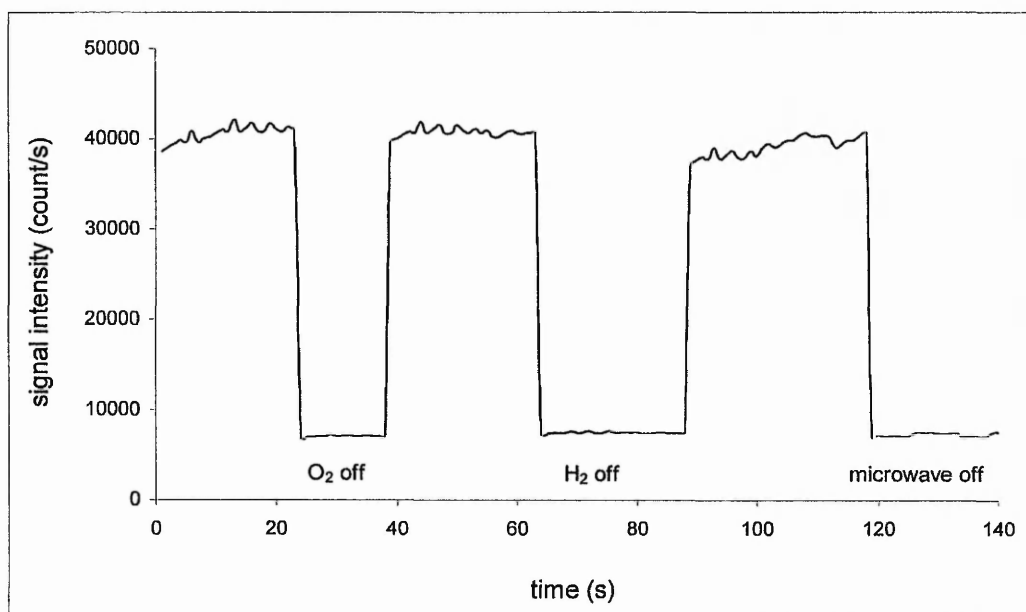
**Figure 4.5:** Single ion monitoring scan obtained during the peroxy radical identification experiments

4.3.5. Materials

Nitric Oxide (NO) (Technical grade, Air Products) was purified by freeze-pump-thaw cycles, and selective freezing of Nitrogen dioxide (NO$_2$) impurities. NO$_2$ (99.9%, BOC) was purified by freeze thaw cycles in a O$_2$ rich atmosphere to remove NO impurities and gas mixtures were generated at 760 Torr pressure. Helium (CP Grade, BOC) before entering the Surfatron cavity was first passed through a gas clean oxygen filter (Chrompak) cartridge to remove traces of oxygen and then a Gas clean moisture filter cartridge (Chrompak) to remove H$_2$O and finally a trap held at 77 K containing a molecular sieve (BDH, 4A). Hydrogen (H$_2$) (N5.0 cp grade 99.999%, BOC), Sulfurhexafluoride (SF$_6$) (99.99%, BOC) and nitrogen (N$_2$) and oxygen (O$_2$) (99.6%, BOC) were used as supplied.

4.4. Experimental Procedure

4.4.1 Detection Sensitivities

Dilute mixtures of NO$_2$ were injected *via* the moveable injector into the flow tube with no other gases present and the NO$_2^-$ signal was monitored. From a linear plot of [NO$_2$] *vs.* NO$_2^-$ signal it is estimated that the sensitivity for NO$_2$ was 2×10^7 molecule cm^{-3} for a signal to noise ratio of one and a time constant of 1 s as shown in figure 4.6.
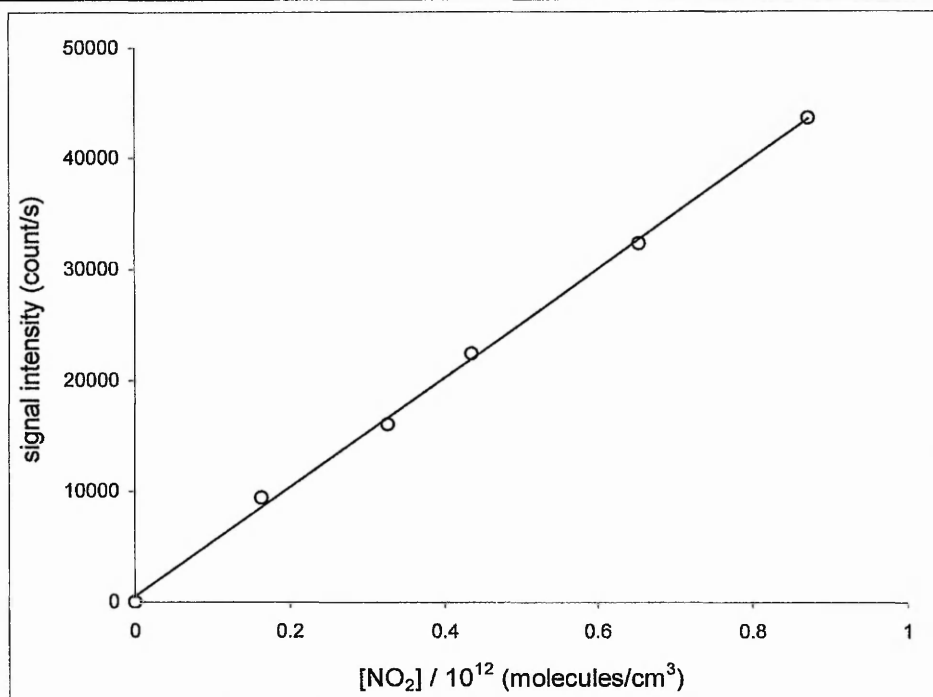
Figure 4.6: The sensitivity plot for NO$_2$ (sensitivity is equal to one over the slope).

The NO$_2$ concentrations were corrected to take into account equilibrium concentrations of N$_2$O$_4$ in the gas mixtures used (Borrel *et al.*, 1988). Under the experimental conditions the lifetime of N$_2$O$_4$ formed by the equilibrium reaction (4.6) is comparable with the time of mixing

$$NO_2 \quad + \quad NO_2 \quad + \quad M \quad \rightleftharpoons \quad N_2O_4 \quad + \quad M \qquad R.4.6$$

This assumption was collaborated by the fact that on the time scale of the experiment no change was observed in [NO$_2$].

4.4.2. Hydroperoxy Radical Calibration

Calibration of the HO$_2$ signal was achieved by adding a large excess of NO *via* the moveable injector at a constant contact time and by monitoring the resultant NO$_2$ formed by reaction with HO$_2$ as in reaction (4.7).

$$HO_2 \quad + \quad NO \quad + \quad M \quad \rightleftharpoons \quad NO_2 \quad + \quad OH \quad + \quad M \qquad\qquad R.4.7$$

Sufficient NO was added to ensure complete removal of HO$_2$, confirmed by a constant NO$_2^-$ signal with increasing [NO]. It is assumed that [NO$_2$] $_{observed}$ = [HO$_2$] as shown in figure 4.7. This procedure was repeated for several different hydrogen atom concentrations and yielded a linear plot of HO$_2^-$ signal *vs.* [NO$_2$] $_{observed}$ as shown in figure 4.8. It is estimated that the sensitivity for HO$_2$ was 1×10^7 molecule cm^{-3} for a signal to noise ratio of one and a time constant of 1 s.
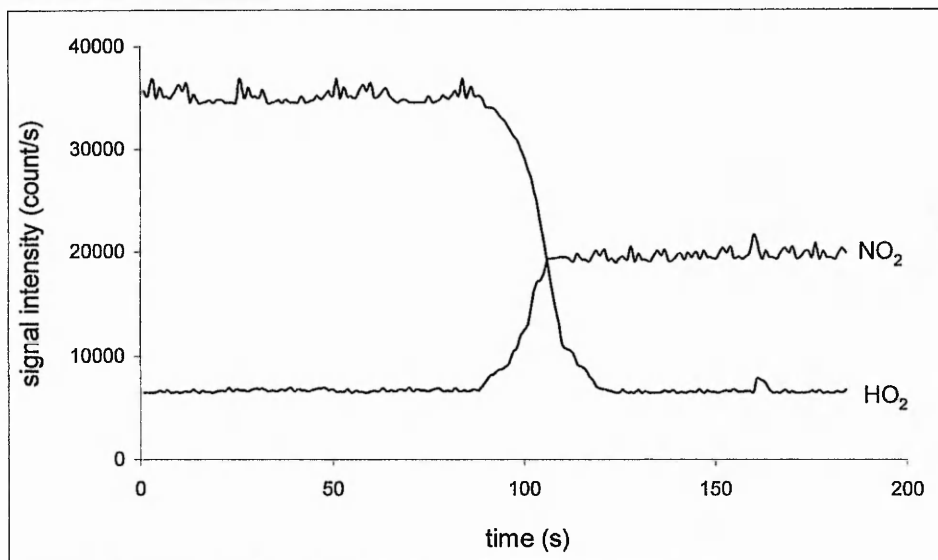
Figure 4.7: Scanning obtained in single ion monitoring mode depletion of HO$_2$ signal synchronise with NO$_2$ production *via* reaction (4.7).
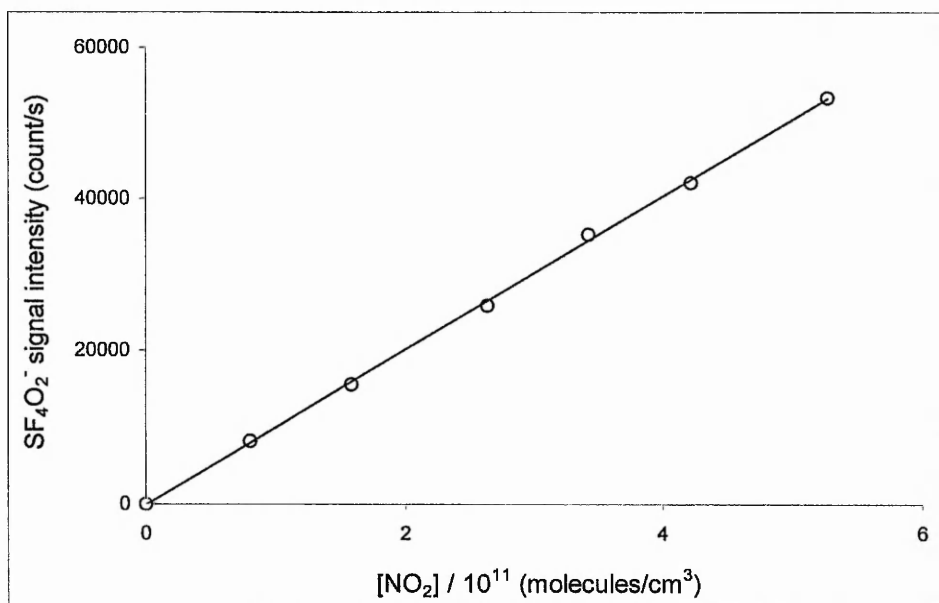
Figure 4.8: The sensitivity plot for HO$_2$ (sensitivity is equal to one over the slope).

## 4.5 Room Temperature Rate Coefficient Determination

The rate coefficient for reaction (4.1), was measured by monitoring HO$_2$ concentration profiles at m/e = 140 (as SF$_4$O$_2^-$ Bardwell *et al.*, 2003) under pseudo-first-order conditions with [HO$_2$] = $(1 - 10) \times 10^{10}$ molecule cm^{-3} and [NO$_2$] = $(1 - 12) \times 10^{12}$ molecule cm^{-3}. First order decay rates k_{1st} were obtained by a linear regression of the plots of ln (HO$_2$ signal) *vs.* contact time as shown in Figure 4.9.
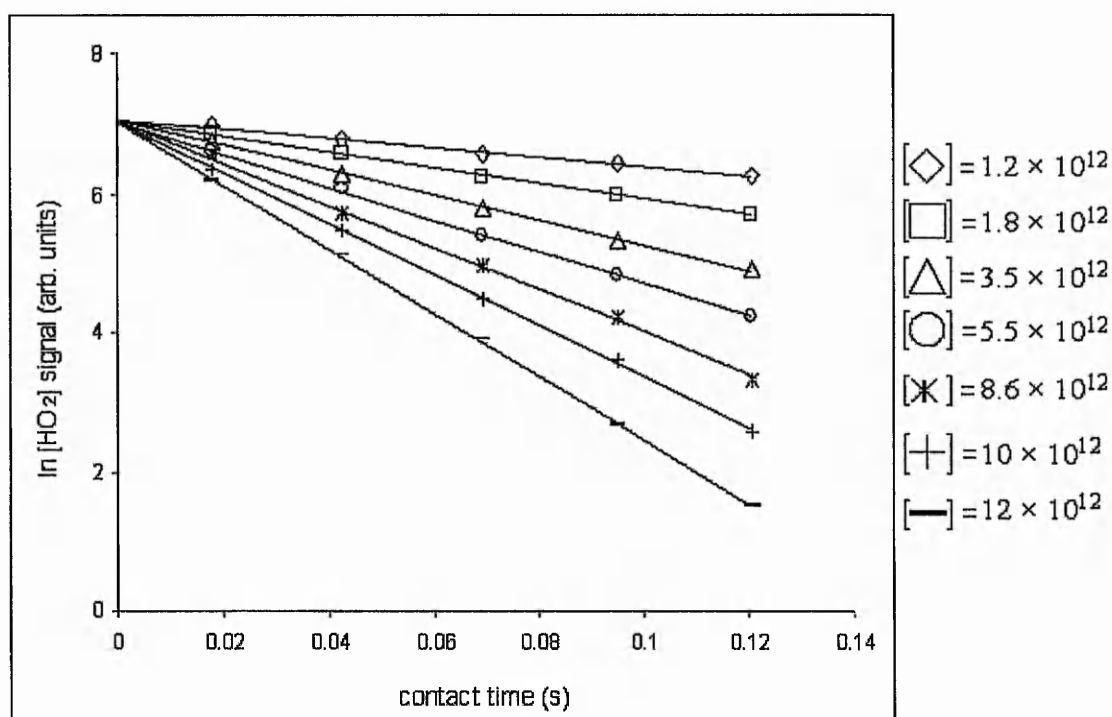
Figure 4.9: Pseudo-first-order decay profiles of SF$_4$O$_2^-$ as a function of contact time in the flow tube. Sets of decays correspond to different concentrations of NO$_2$ fit to each yield pseudo-first-order rate coefficients, k_{1st}

Each of these plots were essentially linear for all the experiments indicating the absence of any secondary chemistry effects. Non-linear fits of the plots of (HO$_2$ signal) *vs.* contact time were also carried out. Both methods yielded identical values of k_{1st} within experimental error. This process was repeated for at least ten different values of [NO$_2$] at each pressure studied. The values of k_{1st} were then plotted *vs.* [NO$_2$] as shown in figure 4.10.
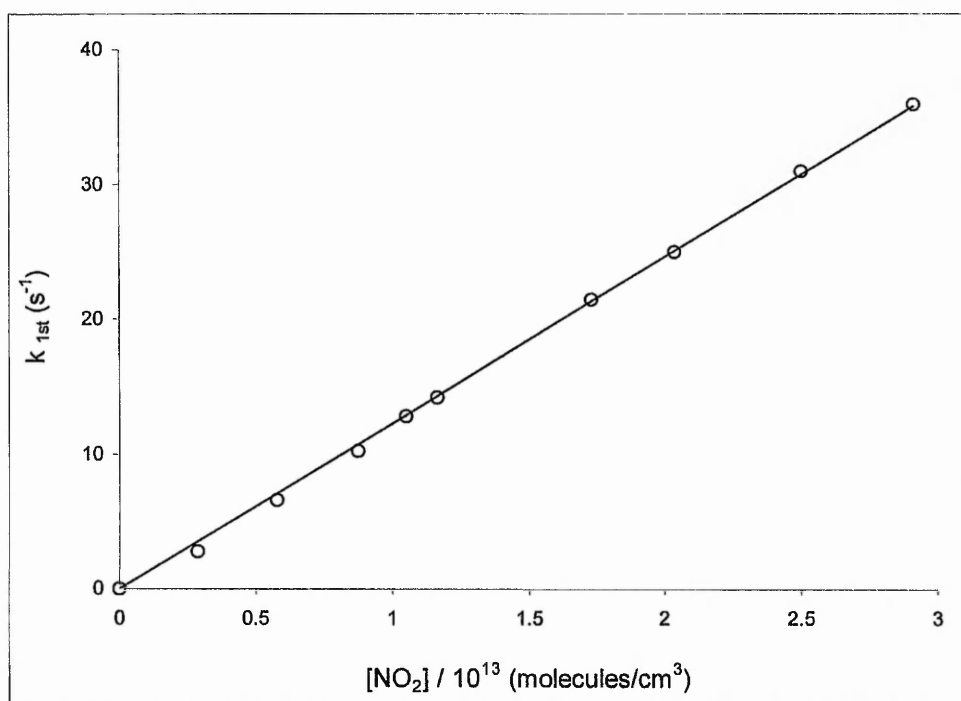
Figure 4.10: Pseudo-first-order rate coefficients plotted as a function of NO$_2$ concentration.

These data points were fitted with a linear least squares routine, the slope of which gives the effective bimolecular rate constant $k_{4.1}$, Table 4.2 lists the bimolecular rate coefficients obtained in this study. This approach for the determination of the effective bimolecular rate coefficient assumes that deviations from the plug flow approximation are negligible. Under the experimental conditions used, Seeley *et al.*, (1996) estimated that deviations from the plug flow approximation result in apparent rate coefficients that are at most 8% below the actual values. Hence, flow corrections were neglected, as they are smaller than the sum of other systematic experimental errors.

Pressure (Torr)	$k_{4.1}$ (cm^3 molecule^{-1} s^{-1})
200	$(6.32 \pm 0.15) \times 10^{-13}$
300	$(8.02 \pm 0.03) \times 10^{-13}$
418	$(9.67 \pm 0.05) \times 10^{-13}$
517	$(1.10 \pm 0.02) \times 10^{-12}$
607	$(1.21 \pm 0.06) \times 10^{-12}$
712	$(1.31 \pm 0.12) \times 10^{-12}$

Table 4.2: Second order rate coefficient obtained in different pressures at 298 K

The pressure dependence of the rate coefficient observed in this study at 298 K is shown in Figure 4.11.
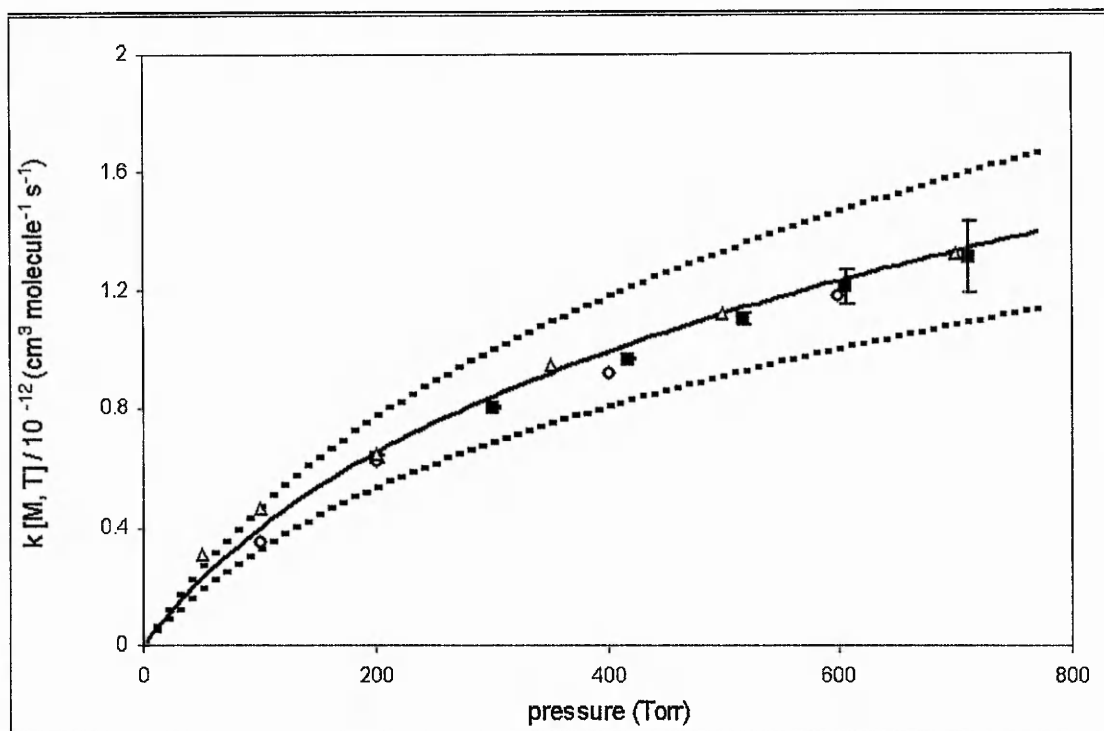
Figure 4.11: The pressure dependence of the rate coefficient as observed in this study at 298 K (■). The pressure dependence suggested by DeMore *et al.,* (1997) is also shown for comparison with a solid line. The dashed lines represent the upper and lower limits in $k(M,T)$ as associated with the quoted errors in the values of k_o and k_∞.

Also in same figure data from previous studies have shown at pressure similar to those used in this work Kurylo and Ouellette (1987) represented with (○), Sanders and Peterson (1984) represented with (△).

To obtain the second order rate constant for a given condition of temperature and pressure the following formula is used (Troe J. 1979).

$$k(M, T) = \left(\frac{k_0(T)[M]}{1 + (k_0(T)[M]/k_\infty(T))} \right) 0.6^{\left\{ 1 + \left[\log_{10}\left(k_0(T)[M]/k_\infty(T) \right) \right]^2 \right\}^{-1}}$$

E.5.1.

Where

$$k_0(T) = k_0^{300} (T/300)^{-n} \quad cm^6 \ molecule^{-2} \ s^{-1}$$

And

$$k_\infty(T) = k_\infty^{300} (T/300)^{-m} \quad cm^3 \ molecule^{-1} \ s^{-1}$$

k_0 = Low pressure rate coefficient
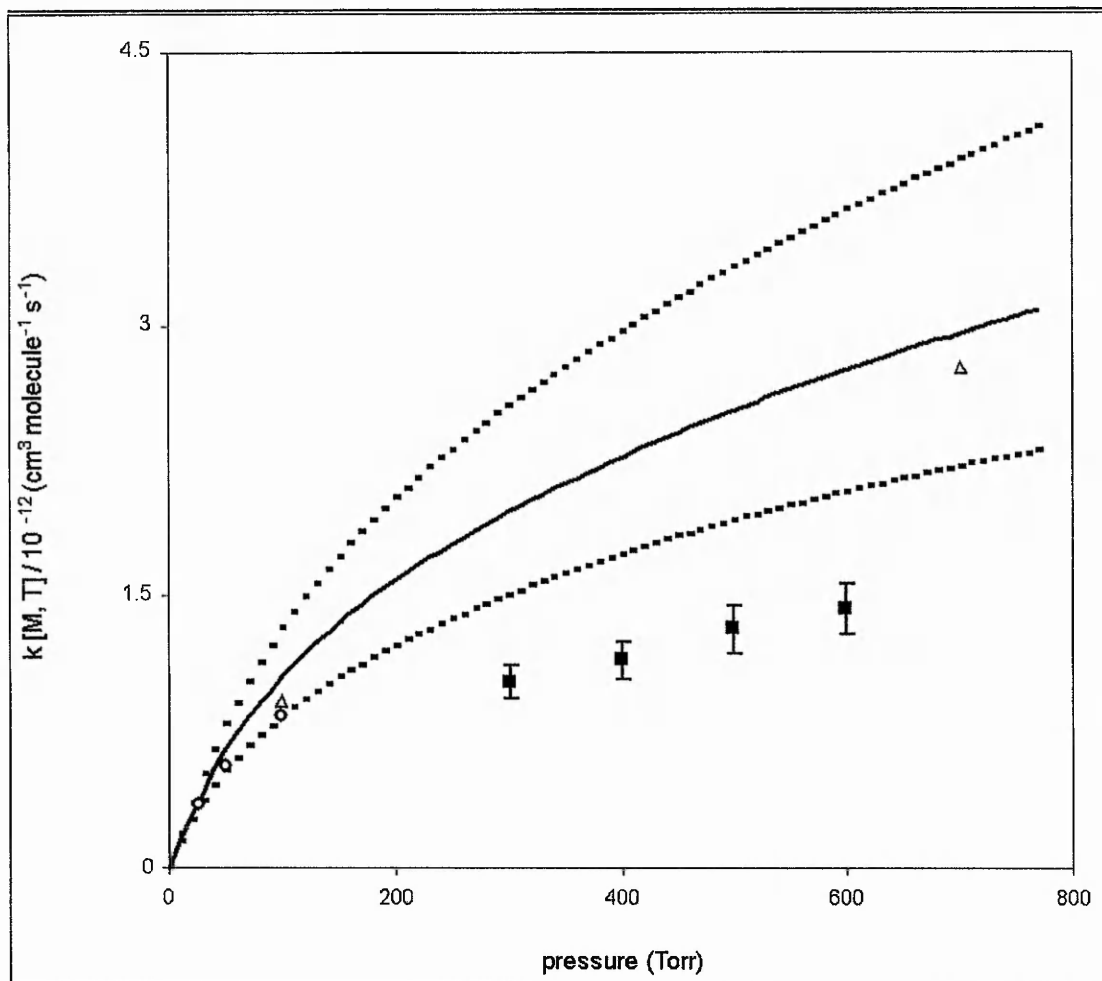
k_∞ = High pressure rate coefficient

n,m = Temperature dependence coefficients

## 4.6 Sub-Ambient Rate Coefficient Determination

After the initial experimental studies conducted at 298 K, the rate coefficient for reaction (4.1) was measured as a function of pressure and temperature. Experiments for the determination of the rate coefficient for reaction (4.1) ($k_{4.1}$) were carried out at 223 K and 200 K. The experimentally determined rate coefficients as a function of pressure are shown in Table 4.3 and Figures 4.12 and 4.13.

Pressure (Torr)	223 K	200 K
	$k_{4.1}$ (cm³ molecule⁻¹ s⁻¹)	$k_{4.1}$ (cm³ molecule⁻¹ s⁻¹)
150	Not measured.	$(7.27 \pm 0.06) \times 10^{-13}$
300	$(1.03 \pm 0.09) \times 10^{-12}$	$(1.17 \pm 0.10) \times 10^{-12}$
400	$(1.15 \pm 0.10) \times 10^{-12}$	$(1.45 \pm 0.12) \times 10^{-12}$
500	$(1.32 \pm 0.13) \times 10^{-12}$	Not measured.
600	$(1.43 \pm 0.14) \times 10^{-12}$	$(1.65 \pm 0.16) \times 10^{-12}$
700	Not measured.	$(1.78 \pm 0.18) \times 10^{-12}$

Table 4.3: Experimentally measured bimolecular rate coefficients.

Figure 4.12: The pressure dependence of the rate coefficient as observed in this study at 223 K (■). The pressure dependence suggested by DeMore *et al.,* (1997) is also shown for comparison with a solid line. The dashed lines represent the upper and lower limits in k[M,T] as associated with the quoted errors in the values of n and m.
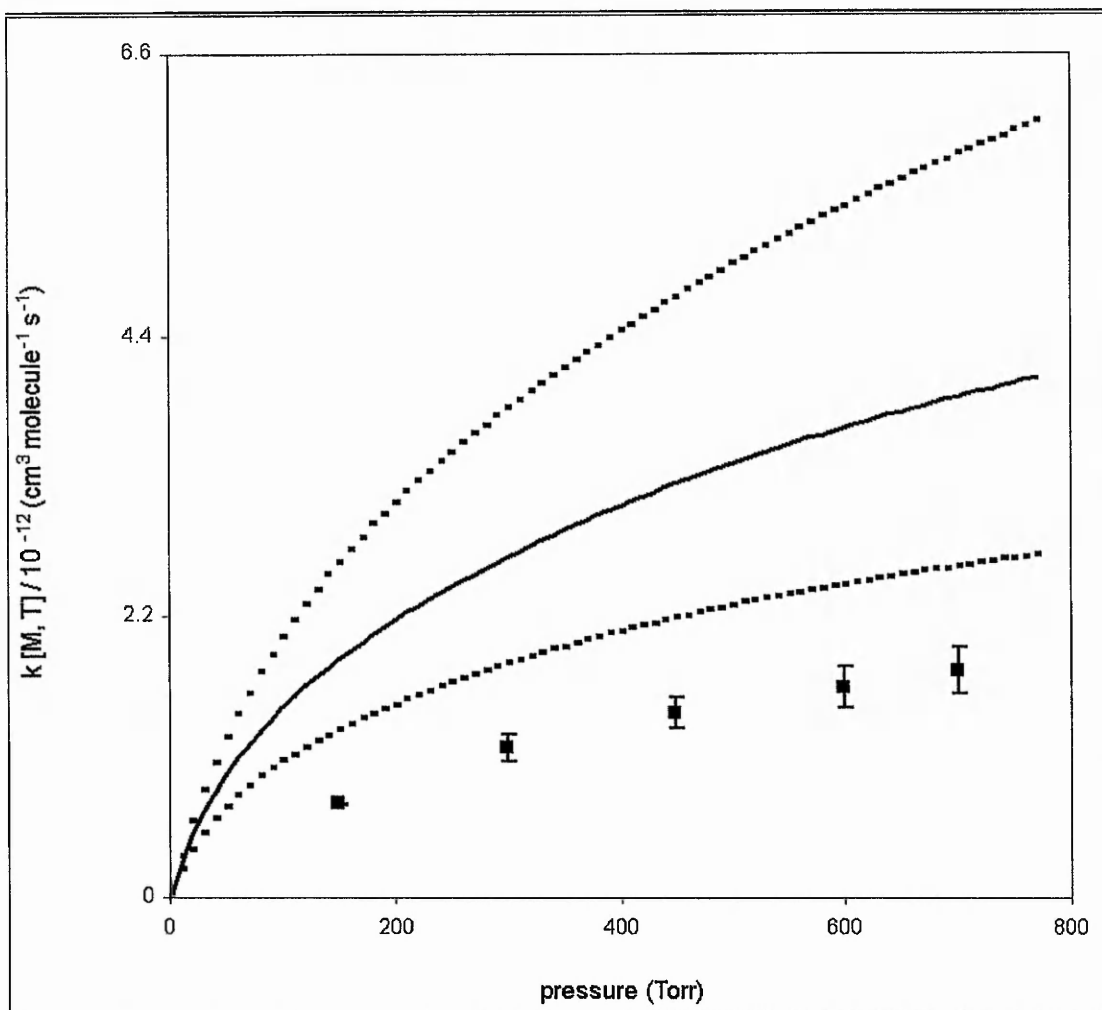
Figure 4.13: The pressure dependence of the rate coefficient as observed in this study at 200 K (■). The pressure dependence suggested by DeMore *et al.,* (1997) is also shown for comparison with a solid line. The dashed lines represent the upper and lower limits in *k*[M,T] as associated with the quoted errors in the values of n and m.

The experimentally observed data for 223 K and 200 K is presented in Figures 4.12 and 4.13. Also in Figure 4.12 data included from previous studies (○) represents Kurylo and Ouellette (1987), (△) represents Sanders and Peterson (1984). Studies that directly overlap the pressures used in this work, in Figures 4.12 and 4.13 the solid line is the pressure dependence as suggested by DeMore *et al.*, (1997) using Equation 5.1 and the dashed lines in represent the upper and lower limits in k[M,T] as associated with the quoted errors in the values of n and m. The observed temperature dependence reported in this study demonstrate significant differences with data previously reported and the suggested values proposed by De More *et al.*, (1997). The overall temperature dependence of the observed rate coefficient is defined by values of n (temperature dependence of low-pressure limiting rate coefficient) and m (temperature dependence of high-pressure limiting rate coefficient). The results presented in this thesis seem to suggest that for the temperature dependence of the reaction of HO$_2$ + NO$_2$ is much less than has been previously observed. Indeed, out results indicate that n = 0.2 ± 0.3 and m = 0.5 ± 0.3 compared to there is a much higher values of n = 3.2 ± 0.4 and m = 1.4 ± 1.4 suggested by DeMore *et al.*, (1997).

Despite the importance of reaction (4.1) in both the troposphere and stratosphere there have only been three limited experimental studies on the temperature dependence of the reaction. Table 4.5 summarises the experimental conditions employed in all of the experimental studies on the temperature dependence of reaction (4.1).

Reference	Technique	T (K)	P (T)	[X]$_0$	Rad. Generation.
Christensen *et al.,* 2004	NIR-UV absorption Spectroscopy	298	45	$[HO_2]_0 = (5\text{-}8)\times10^{13}$	$Cl_2+h\nu\rightarrow2Cl$ $Cl+CH_3OH\rightarrow CH_2OH+HCl$ $CH_2OH+O_2\rightarrow HO_2+CH_2O$
		220	200	$[NO_2]_0 = (6\text{-}50)\times10^{14}$	
Kurylo and Ouellette, 1987	FP-UV absorption Spectroscopy	358	25	$[HO_2]_0 = (2\text{-}6)\times10^{13}$	$Cl_2+h\nu\rightarrow2Cl$ $Cl+CH_3OH\rightarrow CH_2OH+HCl$ $CH_2OH+O_2\rightarrow HO_2+CH_2O$
		228	100	$[NO_2]_0 = (1\text{-}50)\times10^{14}$	
Sander and Peterson, 1984	FP-UV absorption Spectroscopy	362	50	$[HO_2]_0 = (1\text{-}4)\times10^{13}$	$Cl_2+h\nu\rightarrow2Cl$ $Cl+CH_3OH\rightarrow CH_2OH+HCl$ $CH_2OH+O_2\rightarrow HO_2+CH_2O$
		229	700	$[NO_2]_0 = (3\text{-}40)\times10^{14}$	
This work	TF-CIMS	298	150	$[HO_2]_0 = (1\text{-}10)\times10^{10}$	$H+O_2\rightarrow HO_2$
		200	700	$[NO_2]_0 = (1\text{-}12)\times10^{12}$	

Table 4.5: Summary of the previous temperature and pressure dependence studies for the reaction (4.1) and subsequent concentrations of HO$_2$ and NO$_2$.

The two earlier studies by Kurylo and Ouellette (1987) and Sander and Peterson (1984) utilised the flash photolysis technique with ultraviolet absorption at one wavelength, at ~ 228 nm, for the detection of HO$_2$. In both studies HO$_2$ was produced *via* the photolysis of Cl$_2$ in the presence of CH$_3$OH and O$_2$ and NO$_2$ was added in excess to maintain pseudo-first-order conditions. A major complication to the use UV-absorption for the detection of HO$_2$ is that N$_2$O$_4$ strongly absorbs in the range. The presence of overlapping absorbers will alter the time dependent UV-absorption spectra and this could possibly lead to significant errors in the experimentally retrieved rate coefficients. This prompted a recent re-evaluation of the temperature dependence of the rate coefficient by Christensen *et al.,* (2004).

Christensen *et al.,* (2004) employed the same chemistry for radical production, however, used Near-Infrared Wavelength modulation spectroscopy for the detection of HO$_2$.

The HO_2 was detected at 6638.2 cm^{-1} probing the Q transition of the first overtone of the O–H stretch using a diode laser. Using NIR wavelengths removes the problem of overlapping absorbers and thus enables the accurate determination of concentration time profiles. Christensen *et al.*, (2004) point out that errors associated with the retrieved rate coefficients using UV absorption technique are significant in excess of 50%, however, they are still in fair agreement with the previous studies. Christensen *et al.* (2004) suggest that this is as a result of the "fortuitous" cancellation of errors at low temperatures. The presence of overlapping absorbers would lead to an underestimation of rate coefficient and this error was offset by neglecting the enhancement of the rate coefficient by methanol *via* the chaperone mechanism.

Whilst the use of NIR spectroscopy represents a significant advancement for the study of peroxy radical kinetics using flash photolysis its absolute sensitivity is still orders of magnitude less than the CIMS employed in this study and thus much larger initial radical concentrations have to be employed, as indicated in Table 4.5. All the previous studies on the temperature dependence of reaction (4.1). use large initial [HO_2] of $(2 - 8) \times 10^{13}$ molecule cm^{-3}. Hence, data has to be corrected for the self-reaction of HO_2. Indeed, Kurylo and Ouellette (1987) show that the corrections to the observed HO_2 time profiles were as high as 25% at room temperature. Considering that the HO_2 self-reaction displays significant negative temperature dependence the correction needed would increase for the lower temperature studies. Thus all studies can potentially over estimate the temperature dependence of reaction (4.1). The lower initial [HO_2] used in this study effectively removes the contribution of the HO_2 self reaction to the observed HO_2 time profiles and could thus explain the discrepancy in the observed temperature dependence.

4.8. Atmospheric Implications

In order to asses the impact of lower value for the rate coefficient of reaction (4.1) on tropospheric chemistry model sensitivity studies have been performed, using the CiTTy CAT tropospheric trajectory model. The CiTTy CAT model was run using a methane only chemistry scheme at T = 298 and T = 200 K. For each temperature the model was integrated forward in a box model mode for five days. Two integrations were performed for each temperature utilizing the kinetic parameters for $k_{4.1}$ as recommended by DeMore *et al.*, (1997) in comparison with a 25% reduction in the value of k_∞. Comparisons between each set of integrations were then made for a range of species, including O_3, OH, HO_2, HO_2NO_2, H_2O_2, HNO_3 and CH_3O_2, NO and NO_2.

For the model runs at 298 K there was no discernable change in the concentration of the atmospheric species. This is hardly surprising as the lifetime of HO_2NO_2 with respect to thermal decomposition is so small that in effect HO_2NO_2 when formed immediately decomposes to form HO_2. However, for the model runs at 200 K there is a significant impact on HO_2NO_2 formation, as shown in Figure 4.14. The model suggests that the
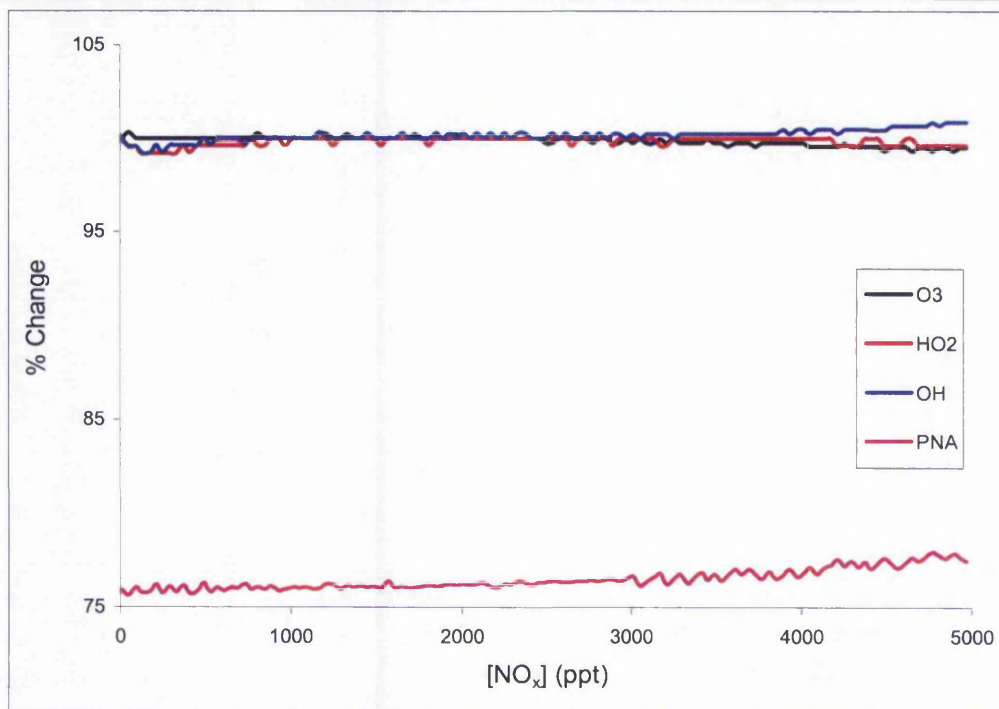
Figure 4.14: A sensitivity plot for O_3, HO_x and PNA production at 200 K

HO_2NO_2 formation will decrease by approximately 20% and yet the HO_x and O_3 does not deviate by more than 1%. At the lower temperatures HO_2NO_2 is thermally stable and the 25% reduction in $k_{4.1}$ results in significantly lower HO_2NO_2 concentrations. The lower value of $k_{4.1}$ also leads to an increase in NO_x in the system. This will result in an increase the rate of loss of peroxy radicals *via* reaction with NO as shown in reactions (4.8 and 4.9)

CH_3O_2 +   NO   → CH_3O + NO_2 R 4.8

HO_2 +   NO   →   OH   + NO_2 R 4.9

leading to a net loss of HO_x from the system. However, the reaction of the methoxy radical formed in reaction (4.9) with molecular oxygen will lead to the formation of HO_2 and thus there is no significant change in the modeled HO_x. Thus a reduction in the $k_{4.1}$ at low temperatures would lead to a decrease in the formation of PNA without having a significant impact on other species. Recently Murphy *et al.*, (2003) have measured PNA in the upper troposphere and have shown that the observed HO_2NO_2 is much lower than that described by models. From the work presented in this chapter a reduced temperature dependence in $k_{4.1}$ could explain the discrepancy between observed and modeled HO_2NO_2 profiles. However further experimental work to evaluate $k_{4.1}$ over a wider range of pressures is required in order to fully understand the role of HO_2NO_2 formation in the chemistry of the UTLS region.

4.9. Conclusion

Our results indicate that reaction (4.1) has a significant pressure dependence, as suggested by previous studies (e.g. Christensen *et al.*, 2004). Our results are in excellent agreement with previous room temperature determinations of the rate coefficient. The results presented in this chapter represent an extension in the range of temperatures over which reaction (4.1) has been studied experimentally. However, our results display a significantly reduced temperature dependence with extrapolations to 200 K based on previous higher temperature measurements extrapolated to 200 K. The pressure range over which reaction (4.1) has been studied was too narrow to enable an accurate parameterisation of the rate data using Troe type analysis. Additional studies over a wider range of pressures would be useful.

References

Aloisi, S.; Fransico, J. S., *J. Phys. Chem.* A, 2000, 104, 6212

Baldwin, A. C.; Golden, D. M., *J. Phys. Chem.*, 1978, **82**, 644

Bardwell, M.W.; Bacak, A.; Raventos, M.T.; Sanchez-Reyna, G.; Shallcross, D.E.; Percival, C.J., *Phys. Chem. Chem. Phys.*, 2003, **5**, 2381

Borrell, P.; Cobos C. J.; Luther, K., *J. Phys. Chem.*, 1988, **92**, 4377

Christensen, L. E.; Okumura, M.; Sander, S. P.; Friedl, R. R.; Miller, C. E.; Sloan, J. J., *J. Phys. Chem.* A, 2004, **108**, 80

Cox, R.A.; Patrick, K., *Int. J. Chem. Kinet.*, 1979, **11**, 635

DeMore, W.B.; Sander, S.P.; Golden, D.M.; Hampson, R.F.; Kurylo, M.J.; Howard, C.J.; Ravishankara, A.R.; Kolb, C.E.; Molina, M.J., *JPL Publication 97-4*, 1997, 1

Dransfield, T. J.; Donahue, N. M. and Anderson, J. G., *J. Phys. Chem A.* 2001 **105**, 1507

Howard, C.J., *J. Chem. Phys.*, 1977,**67**,5258

Jemi-Alade, A.A.; Thrush, B.A., *J. Chem. Soc. Faraday Trans.*, 1990, **86**, 3355

Kurylo, M.J.; Ouellette, P.A., *J. Phys. Chem.*, 1986, **90**, 441

Kurylo, M.J.; Ouellette, P.A., *J. Phys. Chem.*, 1987, **91**, 3365

Levine, S.Z.; Uselman, W.M.; Chan, W.H.; Ucdirhem, O.; Calvert, J.G.; Shaw, J.H., *Chem. Phys. Lett.*, 1977, **48**, 528

Murphy, J. G.; Thorton, J. A.; Wooldridge, P. J.; Day, D. A.; Rosen, R.S.; Cantrell, C.; Shetter, R. E.; Lefer, B.; Cohen, R. C., *Atmos. Chem. Phys. Discuss.*, 2003, **3**, 5689

Patrick, R.; Golden, D.M., *Int. J. Chem. Kinet.*, 1983, **15**, 1189

Rinsland, C. P., Zander R.; Farmer, C. B.; Norton, R. H.; Brown, L. R.; Russell, J. M.; Park, J. H., *Geophys. Res. Lett.*, 1986, **13**, 761

Rinsland, C. P.; Gunson, M. R.; Salawitch, R. J.; Michelsen, H. A.; Zander, R.; Newchurch, M. J.; Abbass, M. M.; Abrams, M. C.; Manney, G. L.; Chang, A. Y.; Irion, F. W.; Goldman, A.; Mahieu, E., *Geophys. Res. Lett.*, 1996, **23**, 2365

Salawitch, R. J.; Wennberg, P. O.; Toon, G. C.; Sen, B. and Blavier, J.F., *Geophys. Res. Lett.*, 2002, **29**, No. 16

Sander, S.P.; Friedl, R.R.; Miller, C.E.; Christensen, L.E.; Okumura, M.; Sloan, J.J.; *J. Phys. Chem. A.*, 2004, **108**, 80

Sander, S.P.; Peterson, M.E., *J. Phys. Chem.*, 1984, **88**, 1566

Sander, S.P.; Salawitch, R.J.; Toon, G.C.; Sen, B.; Blavier, J.F.; Christensen, L.E.; Okumura, M.; Jucks, W.K., *Geophys. Res. Lett.*, 2002, **29**, No. 9

Seeley, J.V.; Jayne, J.T.; Molina, M.J., *Int. J. Chem. Kinet.*, 1996, **25**, 571

Sen, B.; Toon, G. C.; Osterman, G. B.; Blavier, J. F.; Martigan, J. J.; Salawitch, R. J.; Yue, G.K., *J. Geophys. Res.*, 1998, **103**, 3571

Simonaitis, R.; Heicklen, J., *J. Phys. Chem.* 1976, **80**, 1

Simonaitis, R.; Heicklen, J., *J. Phys. Chem.*, 1974, **78**, 653

Simone A; Francisco, J. S., *J. Phys. Chem A.* 2000 **104**, 6212

Slusher, D.l.; huey, L. G.; Tanner, D. J.; Chen, G.; Davis, D. D.; Buhr, M.; Nowak, J. B.; Eisle, F. L.; Kosciuch, E.; Mauldin, R.L.; Lefer, B. L.; Shetter, R. E.; Dibb, J. E., *Geophys. Res. Lett.*, 2002, **29**, 2011
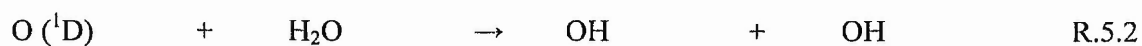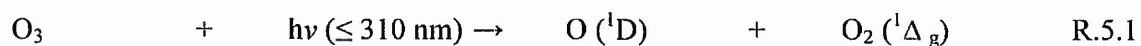
Troe, J., *J. Phys. Chem.*, 1979, **83**, 114

Chapter 5

Kinetics of the Reaction Between CH$_3$O$_2$ and NO$_2$

5.1 Introduction

Methane is the most abundant naturally produced organic compound present in the ambient atmosphere. Natural sources of methane include anaerobic bacterial fermentation in water containing organic waste such as natural wetland areas and oceans and intestinal fermentation in wild animals. Anthropogenic sources of methane include intestinal fermentation in cattle, sewer gas and combustion sources (Wayne, 2000).
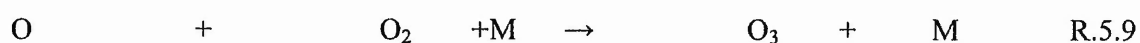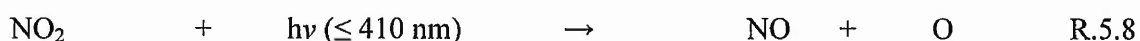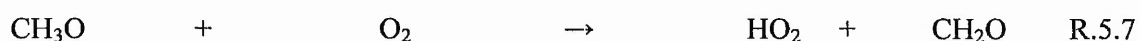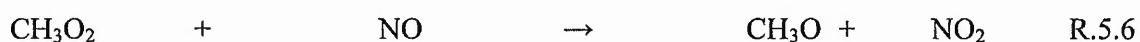
In the daytime troposphere, the dominant sink for methane is by hydrogen abstraction upon reaction with the hydroxyl radical, shown in reaction (5.3).

O_3	+	$h\nu \ (\leq 310 \ nm) \rightarrow$		$O \ (^1D)$	+	$O_2 \ (^1\Delta_g)$		R.5.1
$O \ (^1D)$	+	H_2O	$\rightarrow$	OH	+	OH		R.5.2
CH_4	+	OH	$\rightarrow$	CH_3	+	H_2O		R.5.3
CH_3	+ O_2 +	M	$\rightarrow$	CH_3O_2	+	M		R.5.4
CH_3O_2	+	HO_2	$\rightarrow$	CH_3OOH	+	O_2		R.5.5

The alkyl radical produced in reaction (5.3) then reacts almost exclusively with oxygen to form the methoxy radical reaction (5.4). In the clean troposphere the fate of the methoxy radical is by reaction with the hydroperoxy radical as shown in reaction (5.5). The methyl hydroperoxide produced can then act as a reservoir in the UT region, producing OH upon photolysis or is rained out.

In the polluted atmosphere where there are high levels of NO$_x$, CH$_3$O$_2$ can react with NO to form NO$_2$ as shown in reaction (5.6). (Finlayson-Pitts, B.J.; Pitts, J.N., 1986)

|							
CH$_3$O$_2$	+	NO	$\rightarrow$	CH$_3$O +	NO$_2$		R.5.6
CH$_3$O	+	O$_2$	$\rightarrow$	HO$_2$ +	CH$_2$O		R.5.7
NO$_2$	+	hν ($\leq$ 410 nm)	$\rightarrow$	NO +	O		R.5.8
O	+	O$_2$ +M	$\rightarrow$	O$_3$ +	M		R.5.9

Photolysis of NO$_2$ is the only known way of producing ozone in the troposphere. Reaction 5.6 achieves not only the RO$_2$ to RO radical conversions, but also the oxidation of NO to NO$_2$. They thus provide the link required for catalytic generation of O$_3$ *via* the reactions (5.8 and 5.9).

The importance of NO_x on tropospheric ozone abundance is emphasized in Figure 5.1.

(Wayne, 2000)
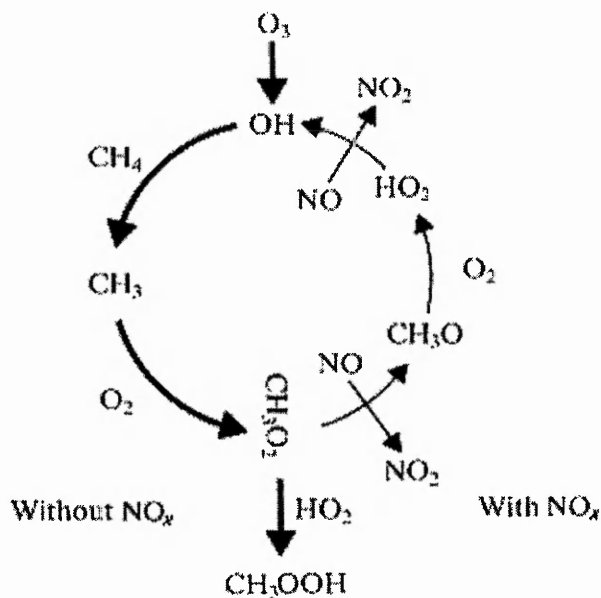
Figure 5.1: Essential steps in tropospheric methane oxidation. The heavier arrows on the left-hand side of the diagram indicate the steps that can occur in the absence of NO_x. With NO_x present, the processes on the right-hand side can close a loop, with regeneration of OH and oxidation of NO to NO_2.

5.1.2 Peroxy Radical Nitrate Formation

The reaction of peroxy radicals with NO$_2$ leads to the formation of peroxy radical nitrate species:

$$RO_2 \quad + \quad NO_2 \quad + \quad M \quad \rightleftharpoons \quad RO_2NO_2 \quad + \quad M \qquad \text{R.5.10}$$
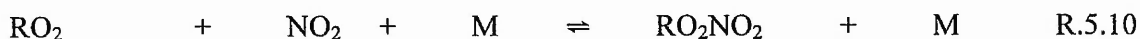
Reaction (5.10) sequesters both peroxy radicals and NO$_2$ and thus has a significant impact on tropospheric O$_3$ production. Also, peroxy nitrates can act as a temporary reservoir of NO$_x$ thermally decomposing in the planetary boundary layer releasing NO$_2$ in reaction (5.10). This means that, under favourable conditions, NO$_x$ can be transported away from source areas as peroxy radical nitrates and re-released where NO$_x$ levels would otherwise be low. The reaction of methyl peroxy radical with NO$_2$:

$$CH_3O_2 \quad + \quad NO_2 \quad + \quad M \quad \rightleftharpoons \quad CH_3O_2NO_2 \quad + \quad M \qquad \text{R.5.11}$$
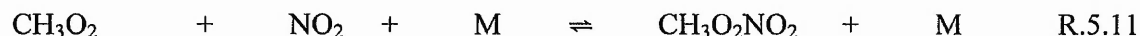
leads to the formation of methyl peroxy nitrate. Methyl peroxy nitrate is the least stable of the peroxy nitrates. However, recent model studies (Lary and Shallcross 1999) have shown that in the mid to upper troposphere CH$_3$O$_2$NO$_2$ may well constitute a significant fraction of NO$_y$ (up to even 20%). Therefore, accurate kinetic parameters for reaction (5.11) are needed to model atmospheric chemistry at these altitudes.

5.2 Previous Experimental Studies on the Reaction of CH$_3$O$_2$+NO$_2$

Previous works on reaction (5.11) are summarized in Table 2.1. As it can be seen from Table there have been numerous studies of the reaction at room temperature. The studies have been performed over a wide range of pressures and are in fair agreement; therefore it can be assumed that reaction (5.11) is well characterized at room temperature.

Despite the importance of the reaction (5.11) for the upper troposphere region, there has only been one experimental study of the reaction (Ravishankara *et al.,* 1980) at temperatures that pertain to the upper troposphere region. Furthermore, the reaction was studied at three different temperatures (298, 350 and 253K) and at two different pressures. There is a clear need for a more thorough study of the reaction to be undertaken and it will be the focus of this chapter.

Group	Temp (K).	Press. (Torr)	Method	k [M,T]
Wallington *et al.,* 1999	295	382—10644	Vis-UV Abs.	1.81×10^{-11}
Lightfoot *et al.,* 1992	253—353	0.01—760	Review	9.95×10^{-12}
Forst and Caralp, 1992	253—353		Theo.	1.02×10^{-11}
Bridier *et al.,* 1992	333—373	760	FP	4.46×10^{-12}
Destriau and Troe, 1990	233—373		RRK (M)	7.51×10^{-12}
Zabel *et al.,* 1989	273—245	7.5—600	FTIR	
Patrick and Golden, 1983	300		Theo.	1.50×10^{-30}
Bahta *et al.,* 1982	256—268	350	UV Abs.	
Sander and Watson, 1980	298	50—700	Vis-UV Abs.	8.00×10^{-12}
Ravishankara *et al.,* 1980	253—353	76—722	Pul. Laser Pho.	6.85×10^{-12}
Adachi and Basco, 1980	298	53—580	FP	9.92×10^{-11}
Cox and Tyndall, 1980	275—338	540	Mod. Spec.	1.6×10^{-12}
Niki *et al.,* 1980	298	760	FTIR	
Cox and Tyndall, 1979	275	50—540	Vis-UV Abs.	8.26×10^{-12}
Simonaitis and Heicklen 1974	298	760	FP	
Spicer *et al.,* 1973	298	97—165	MS	7.5×10^{-1}

Table 5.1: Summary of the previous studies on reaction (5.10).

# 5.3 Experimental Set-Up for the Determination of the CH$_3$O$_2$+NO$_2$ Rate Coefficient

5.3.1 Experimental Design

A schematic diagram of the apparatus is shown in Figure 5.2. The flow tube was constructed from 22 mm id Pyrex tubing, the walls of which were coated with Halocarbon wax (Halocarbon Products inc.). A large flow of nitrogen (ranging from 50 to 130 STP litre min^{-1}) was injected at the rear of the flow tube. The flow tube was pumped by a rotary pump (Varian, DS 1602). Pressure in the flow tube ranged from 100 – 700 Torr depending on experimental conditions. A portion of the gases in the flow tube was sampled into the ion-molecule region *via* an aperture (2 mm). The ion-molecule region was constructed from 22 mm id Pyrex tubing and was pumped by a mechanical pump (Varian, DS 402) and maintained at a pressure of 50 Torr. A quadrupole mass spectrometer (ABB Extrel Merlin) was located at the end of the ion-molecule region. The TF-CIMS chamber pressure was maintained at around 2 Torr. The source region pressure in the mass spectrometer was 1×10^{-4} Torr and the analyser region pressure was held at around 9×10^{-6} Torr. All gas flows were monitored with calibrated mass flow meters (MKS). The pressures in the flow tube and the ion-molecule region were monitored using a 0 – 1000 Torr capacitance manometer (MKS, Baratron).

The temperature within the flow tube was maintained within 2 K by placing the flow tube into an insulated chamber that was filled with dry ice. All temperatures were monitored by type K thermocouples. The flow tube temperature was maintained with heating tape (Omega, Heavy duty) regulated by an electronic controller (Carel Universal Infrared control type W) in conjunction with a thermocouple. The flow tube has 5 thermocouples along its length to monitor the temperature of the system. The nitrogen carrier gas was pre-cooled by passing it through a copper coil immersed in liquid nitrogen. The carrier gas temperature was maintained with heating tape (Omega, Heavy duty) regulated by an electronic controller (Carel Universal Infrared control type W) in conjunction with a thermocouple.
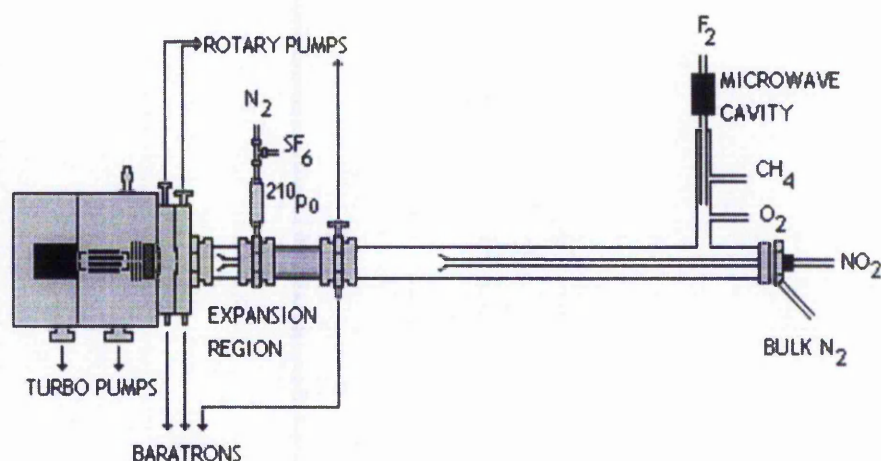
Figure 5.2: A schematic diagram of the Flow Tube Chemical Ionisation Mass Spectrometer system.

5.3.2 CH₃O₂ Generation

CH₃O₂ was produced upstream of the flow tube *via* the following reaction scheme:

CH₄	+	F	+	→	CH₃	+	HF	R.5.12

|								
CH₃	+	O₂	+	M	→	CH₃O₂	+	M	R.5.13
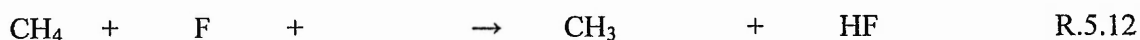
Fluorine atoms were produced by combining a 2.0 STP litre min^{-1} flow of He with a 0.1 to 3 STP cm^3 min^{-1} flow of 5% F_2, which was then passed through a microwave discharge, produced by a Surfatron (Sairem) cavity operating at 175 W. In order to produce CH₃ radicals, the F atoms were injected into the flow tube *via* a side arm inlet located at the rear of the flow tube and mixed with a 1.0 STP litre min^{-1} flow of O_2. Flow of oxygen is already containing 5% 0.1 to 2 STP cm^3 min^{-1} of CH_4. Oxygen and methane were mixed in the carrier line before they were produced into the side arm flow. At the pressures and flow conditions used in this study, it is calculated that the F atoms have been completely titrated before entering the flow tube.

5.3.3 Addition of NO_2

NO_2 was introduced into the flow tube *via* the moveable injector by mixing a flow of 10% NO_2 with a 1 STP litre min^{-1} flow of nitrogen. In all cases, $[NO_2] \gg [CH_3O_2]$ so that pseudo-first-order conditions were maintained. Blank runs (with no NO_2 flowing) were carried out to ensure that CH_3O_2 signal (m/e 52 i.e. FO_2^-) was not affected by the movement of the injector.

5.3.4 Ionisation Schemes

NO_2 and CH_3O_2 were chemically ionised using SF_6^- as the reagent ion. SF_6^- was generated by passing a 10 STP litre min^{-1} flow of N_2 through a ^{210}Po Nuclecel ionizer (NRD Inc.). The generated reagent ion was then carried into the ion-molecule region through an injector constructed from 6 mm od stainless steel. A fan shaped turbulizer was attached to the end of the inlet to enhance mixing of the reagent ion with the sampled flow from the flow tube. NO_2 was ionised by SF_6^- *via* an electron transfer reaction enabling the NO_2 to be detected by its parent ion (m/e 46) as shown in Figure 5.3. CH_3O_2 was detected as FO_2^- (m/e 52), presumably through a multi step pathway as shown in Figure 5.4.
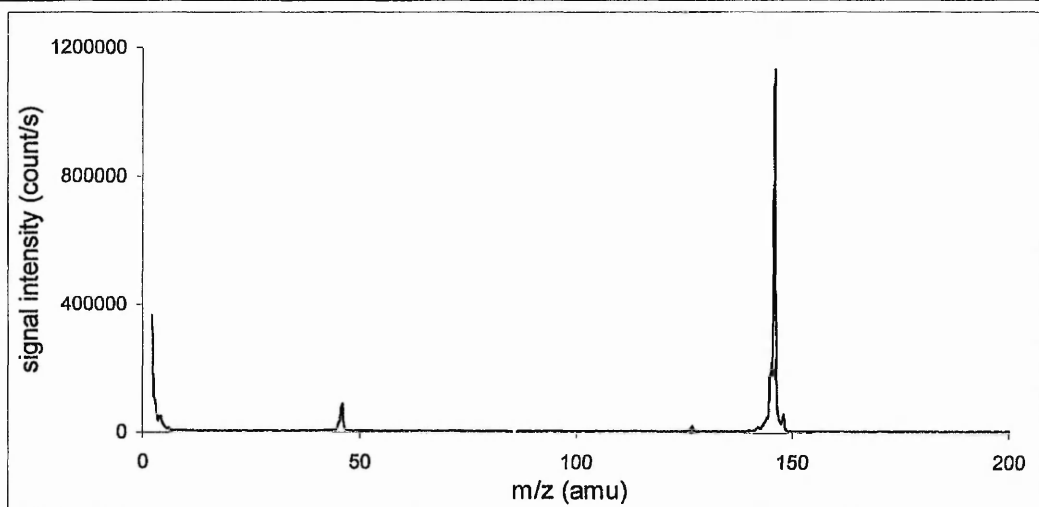
**Figure 5.3:** A spectral scan obtained after the addition of 1 STP cm^3 min^{-1} NO$_2$
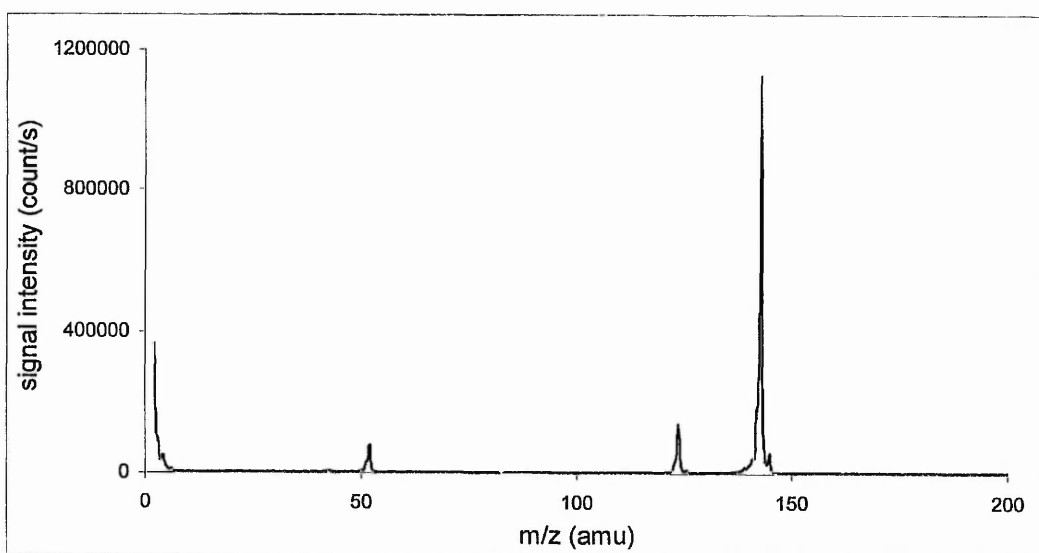
Figure 5.4: A spectral scan obtained after the creation of CH$_3$O$_2$. CH$_3$O$_2$ was detected as FO$_2^-$ (m/e 52)

131

FO$_2^-$ signal only appears when F atoms, CH$_4$ and O$_2$ are present. As shown in Figure 5.5 the FO$_2^-$ signal returns to background levels when any precursor gas flows (CH$_4$, O$_2$ or F$_2$) are turned off. This indicates that FO$_2^-$ can only be attributed to the presence of CH$_3$O$_2$ radicals.
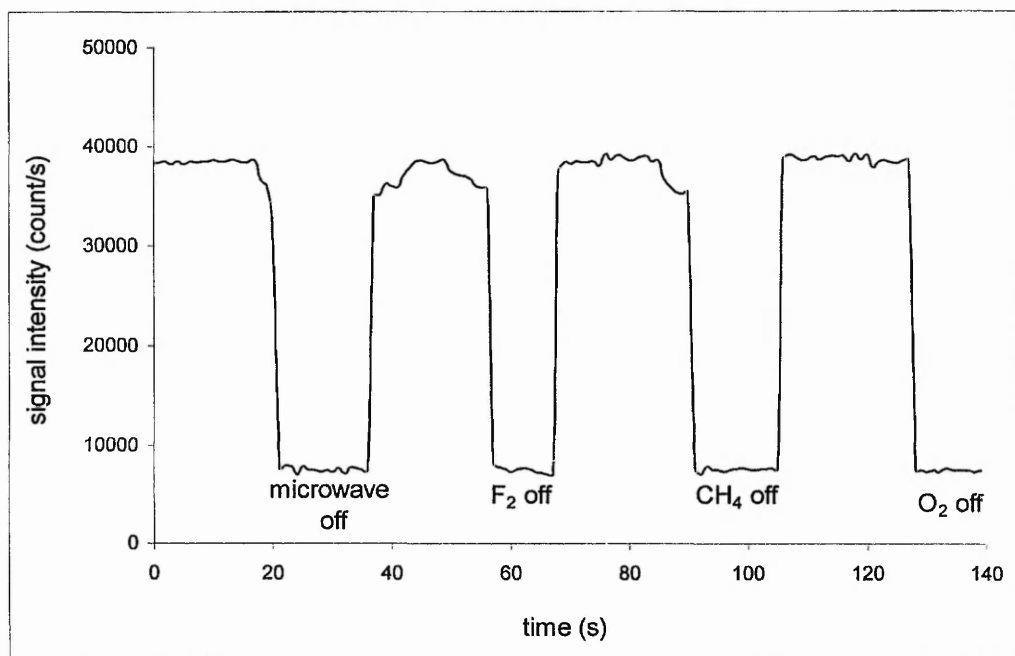
**Figure 5.5:** Single ion monitoring scan obtained during the peroxy radical identification experiments.

5.3.5 Materials

NO$_2$ (99.9%, BOC) was purified by freeze thaw cycles in a O$_2$ rich atmosphere to remove NO impurities and gas mixtures were generated at 760 Torr pressure. CH$_4$ (technical grade Air Products). Helium (BOC, CP Grade) before entering the Surfatron cavity was first passed through a gas clean oxygen filter (Chrompak) cartridge to remove traces of Oxygen and then through a Gas clean moisture filter cartridge (Chrompak) to remove H$_2$O and finally a trap held at 77 K containing a molecular sieve (BDH, 4A). Fluorine 5% balance helium (BOC), Sulfurhexafluoride (SF$_6$) electronic grade (BOC) and Oxygen (99.6%) were used as supplied.

5.4 Experimental Procedure

5.4.1 Detection Sensitivities

Dilute mixtures of NO$_2$ were injected *via* the moveable injector into the flow tube with no other gases present and the NO$_2^-$ (m/e 46) signal was monitored. From a linear plot of [NO$_2$] *vs.* NO$_2^-$ signal, it is estimated that the sensitivity for NO$_2$ was 1.6×10^7 molecule cm^{-3} for a signal to noise ratio of one and a time constant of 1 s, as shown in Figure 5.6.
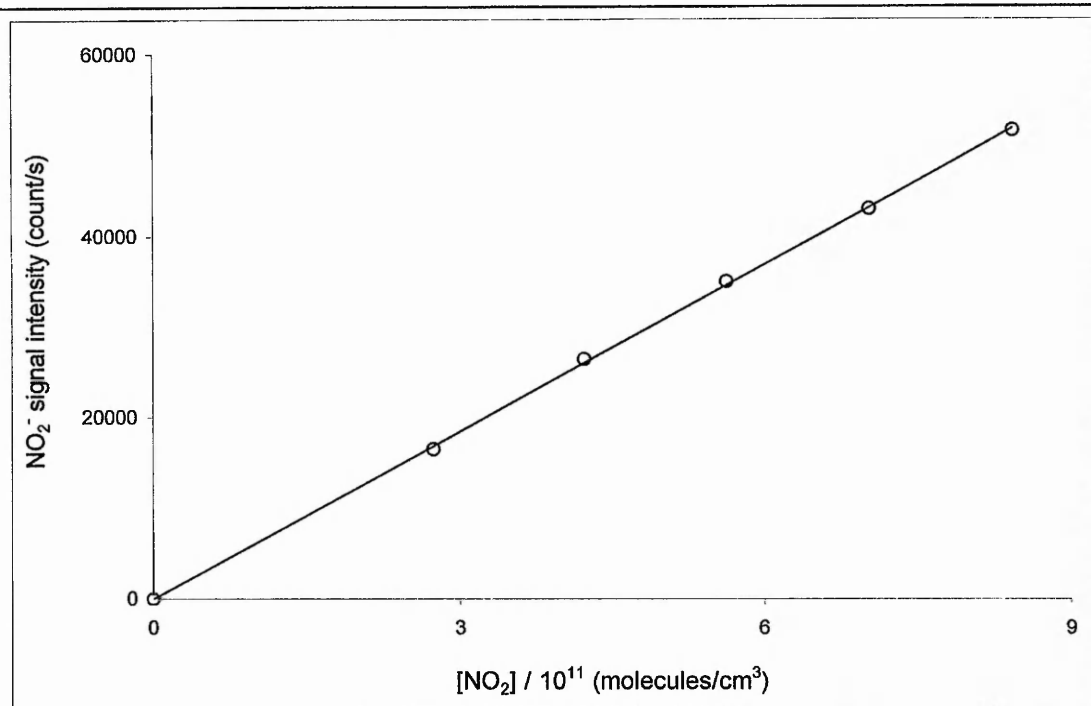
Figure 5.6: Sensitivity plot for NO$_2$ (sensitivity is equal to one over the slope).

The NO$_2$ concentrations were corrected to take into account equilibrium concentrations of N$_2$O$_4$ in the gas mixtures used. Under the experimental conditions the lifetime of N$_2$O$_4$ formed by the equilibrium

$$NO_2 \quad + \quad NO_2 \quad + \quad M \quad \rightleftharpoons \quad N_2O_4 \quad + \quad M \quad\quad\quad R.5.14$$

is comparable with the time of mixing. (Borrell *et al.*, 1988) This assumption was corroborated by the fact that on the time scale of the experiment no change was observed in [NO$_2$].

5.4.2 Methyl Peroxy Radical Calibration

Calibration of the CH_3O_2 signal was achieved by adding a large excess of $\sim$ 50% NO balance He mixture *via* the moveable injector at a constant contact time and monitoring the resultant NO_2 formed by reaction with CH_3O_2.

$$CH_3O_2 \quad + \quad NO \quad \rightarrow \quad CH_2O \quad + \quad NO_2 \qquad \text{R.5.6}$$

Sufficient NO was added to ensure complete removal of CH_3O_2 confirmed by a constant NO_2^- signal with further increases in [NO]. It is assumed that $[NO_2]_{observed} = [CH_3O_2]$ as shown in Figure 5.7. This procedure was repeated for several different fluoride atom concentrations and yielded a linear plot of FO_2^- signal vs. $[NO_2]_{observed}$ as shown in Figure 5.8. The sensitivity for CH_3O_2 was 2.03×10^7 molecule cm^{-3} for a signal to noise ratio of one and a time constant of 1 s.
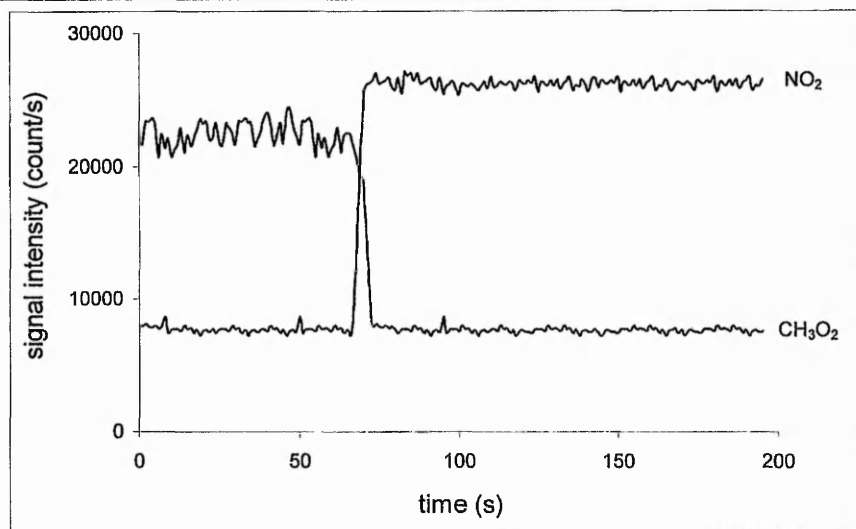
**Figure 5.7:** Scanning obtained in single ion monitoring mode depletion of CH$_3$O$_2$ signal synchronised with NO$_2$ production *via* reaction (5.6).
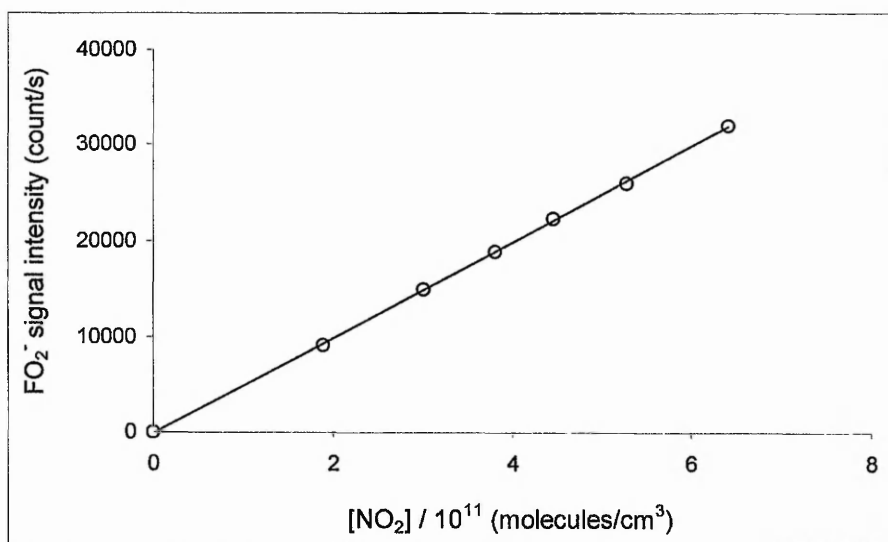
Figure 5.8: Sensitivity plot for CH$_3$O$_2$ (sensitivity is equal to one over the slope).

5.5 Room Temperature Rate Coefficient Determination

The rate coefficient for reaction (5.11) was measured by monitoring CH$_3$O$_2$ concentration profiles at m/e = 52 under pseudo-first-order conditions with [CH$_3$O$_2$] = $(1 - 10) \times 10^{10}$ molecules cm^{-3} and [NO$_2$] = $(1 - 12) \times 10^{12}$ molecules cm^{-3}. First order decay rates k_{1st} were obtained by a linear regression of the plots of ln (CH$_3$O$_2$ signal) *vs.* contact time as shown in Figure 5.9.
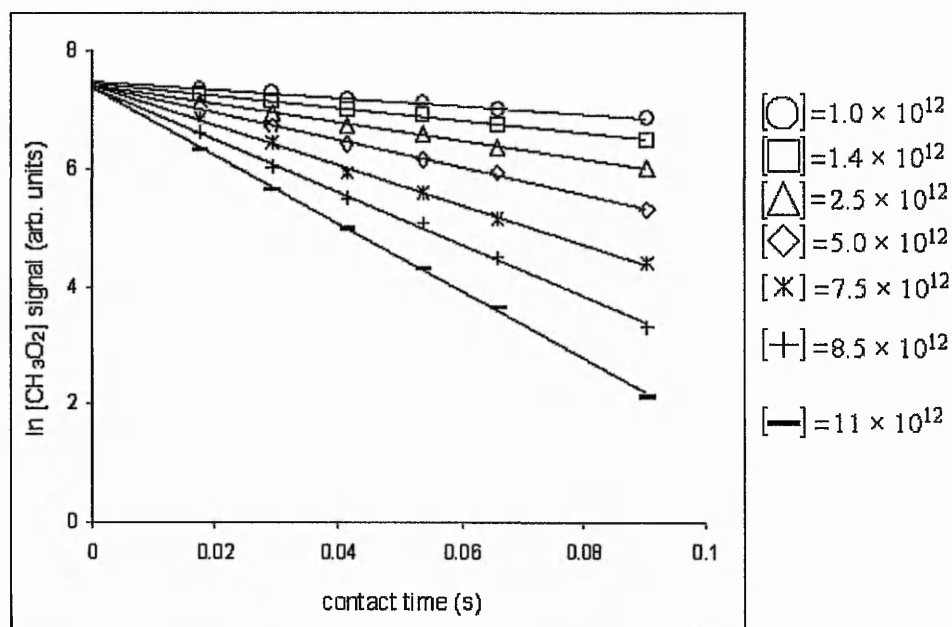
Figure 5.9: Pseudo-first-order decay profiles of CH$_3$O$_2^-$ as a function of contact time in the flow tube. Sets of decays correspond to different concentrations of NO$_2$ fit to each yield pseudo-first-order rate coefficients, k_{1st}.

Each of these plots was essentially linear for all the experiments indicating the absence of any secondary chemistry effects. Non-linear fits of the plots of (CH₃O₂ signal) *vs.* contact time were also carried out. Both methods yielded identical values of k_{1st} within experimental error. This process was repeated for number of different values of [NO₂] at each pressure studied. The values of k_{1st} were then plotted *vs.* [NO₂] as shown in Figure 5.10.
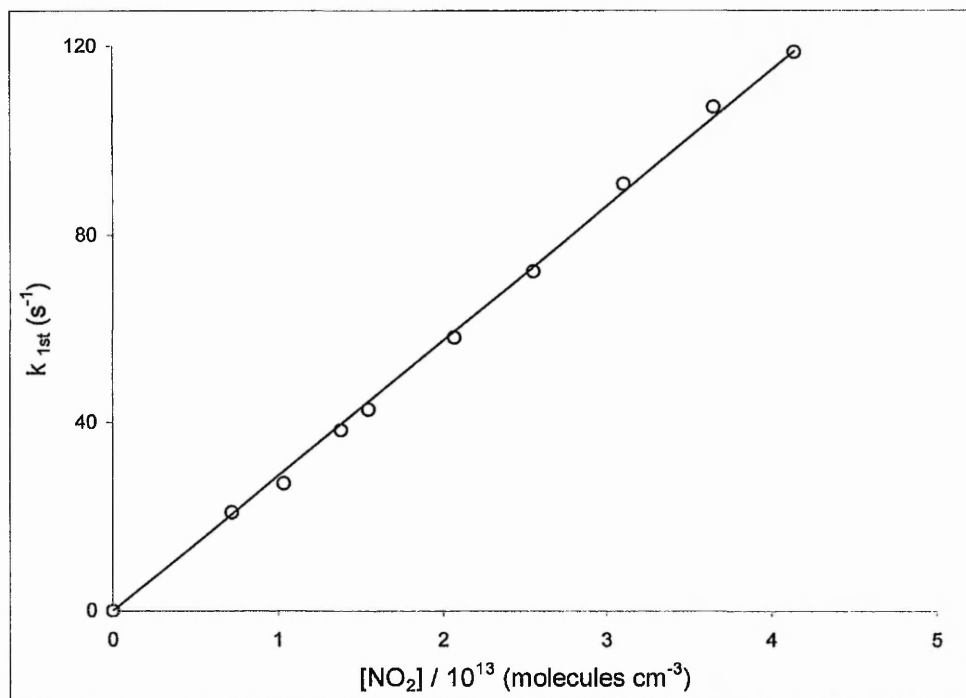
Figure 5.10: Pseudo-first-order rate coefficients plotted as a function of NO₂ concentration. These data points were fitted with a linear least squares routine, the slope that provided the effective bimolecular rate coefficient $k_{5.11}$.

These data points were fitted with a linear least squares routine, the slope of which provided the effective bimolecular rate constant, $k_{5.11}$. The Table 5.2 lists the bimolecular rate coefficients obtained in this study. This approach for the determination of the effective bimolecular rate coefficient assumes that deviations from the plug flow approximation are negligible. Under the experimental conditions used, Seeley *et al.,* (1996) estimated that deviations from the plug flow approximation result in apparent rate coefficients that are at most 8% below the actual values. Hence, flow corrections were neglected, as they are smaller than the sum of other systematic experimental errors.

Pressure (Torr)	$k_{5.11}$ (cm^3 molecule^{-1} s^{-1})
100	$(1.77 \pm 0.12) \times 10^{-12}$
200	$(2.42 \pm 0.11) \times 10^{-12}$
300	$(2.96 \pm 0.28) \times 10^{-12}$
400	$(3.36 \pm 0.29) \times 10^{-12}$
500	$(3.61 \pm 0.36) \times 10^{-12}$
700	$(3.99 \pm 0.30) \times 10^{-12}$

Table 5.2: Second order rate coefficients obtained at 298 K

The bimolecular rate coefficient was measured at room temperature as a function of pressure over the range $100 - 700$ Torr as shown in Figure 5.11.
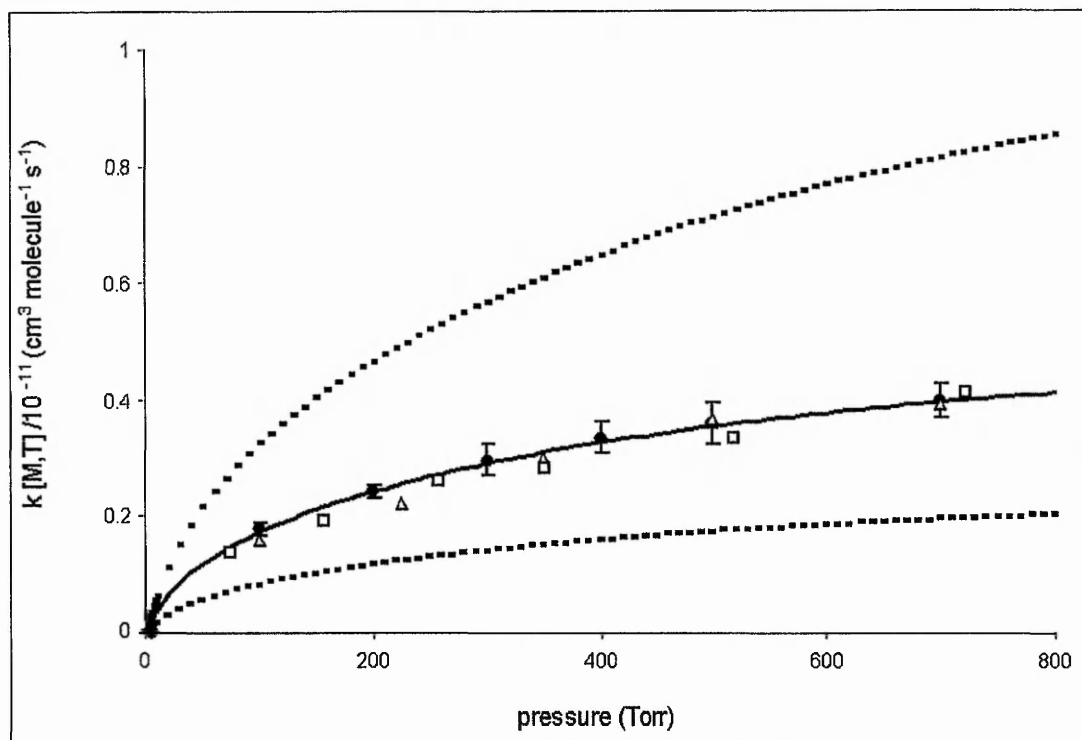
Figure 5.11: The pressure dependence of the rate coefficient as observed in this study at 298 K is represented by (●). Previous studies Sanders and Watson (1980) and Ravishankara *et al.* (1980) are represented by (Δ) and (□) respectively. The pressure dependence suggested by DeMore *et al.,* (1997) is also shown for comparison with a solid line. The dashed lines represent the upper and lower limits in k[M,T] as associated with the quoted errors in the values of k_o and k_∞.

The bimolecular rate constant recommended by DeMore *et al.,* (1997) is of the form.

$$k(M,T)=\left(\frac{k_0(T)[M]}{1+(k_0(T)[M]/k_\infty(T))}\right)0.6^{\left\{1+\left[\log_{10}\left(k_0(T)[M]/k_\infty(T)\right)\right]^2\right\}^{-1}}$$ E.5.1.

where

$$k_0(T)=k_0^{300}\,(T/300)^{-n}\ \ cm^6\ molecule^{-2}\ s^{-1}$$

and

$$k_\infty(T)=k_\infty^{300}\,(T/300)^{-m}\ \ cm^3\ molecule^{-1}\ s^{-1},$$

k_0 = Low pressure rate coefficient,

k_∞ = High pressure rate coefficient,

n,m = Temperature dependence coefficients.

Our results display significant pressure dependence and the observed pressure dependence is in excellent agreement with the values recommended by DeMore *et al.,* (1997) the work of Ravishankara *et al.,* (1980) and that of Sanders and Watson 1980. However, they are in poor agreement with that of Cox and Tyndall (1979) and Adachie and Basco (1980). It has been generally accepted that the work of Cox and Tyndall and Adachie and Basco can be discounted, as they did not observe pressure dependence. As pointed by Ravishankara *et al.,* (1980) the studies were carried out with large initial [CH$_3$O$_2$] and the observed [CH$_3$O$_2$] time profiles had a significant contribution from the CH$_3$O$_2$ self reaction and that thermal decomposition of the CH$_3$O$_2$NO$_2$ adduct also affected the observed concentration time profiles.

5.6 Sub - Ambient Rate Coefficient Determination

As already pointed out there has only been one study of the temperature dependence of reaction (5.11) at sub-ambient temperatures (Ravishankara *et al.*, 1980). However there have been no studies of the reaction at T < 253 K. Experiments were also carried out at 223 K and the measured rate coefficients as a function of pressure dependence are shown in Table 5.3 and Figure 5.12.

Pressure (Torr)	$k_{5.11}$ (cm^3 molecule^{-1} s^{-1})
200	$(6.35 \pm 0.41) \times 10^{-12}$
300	$(7.00 \pm 0.21) \times 10^{-12}$
400	$(7.60 \pm 0.60) \times 10^{-12}$
500	$(8.15 \pm 0.08) \times 10^{-12}$
600	$(8.28 \pm 0.03) \times 10^{-12}$
700	$(8.80 \pm 0.60) \times 10^{-12}$

Table 5.3: Second order rate coefficient rate constants obtained at 223 K

Once again, the agreement with the extrapolated values suggested by DeMore *et al.,* (1997) is excellent.
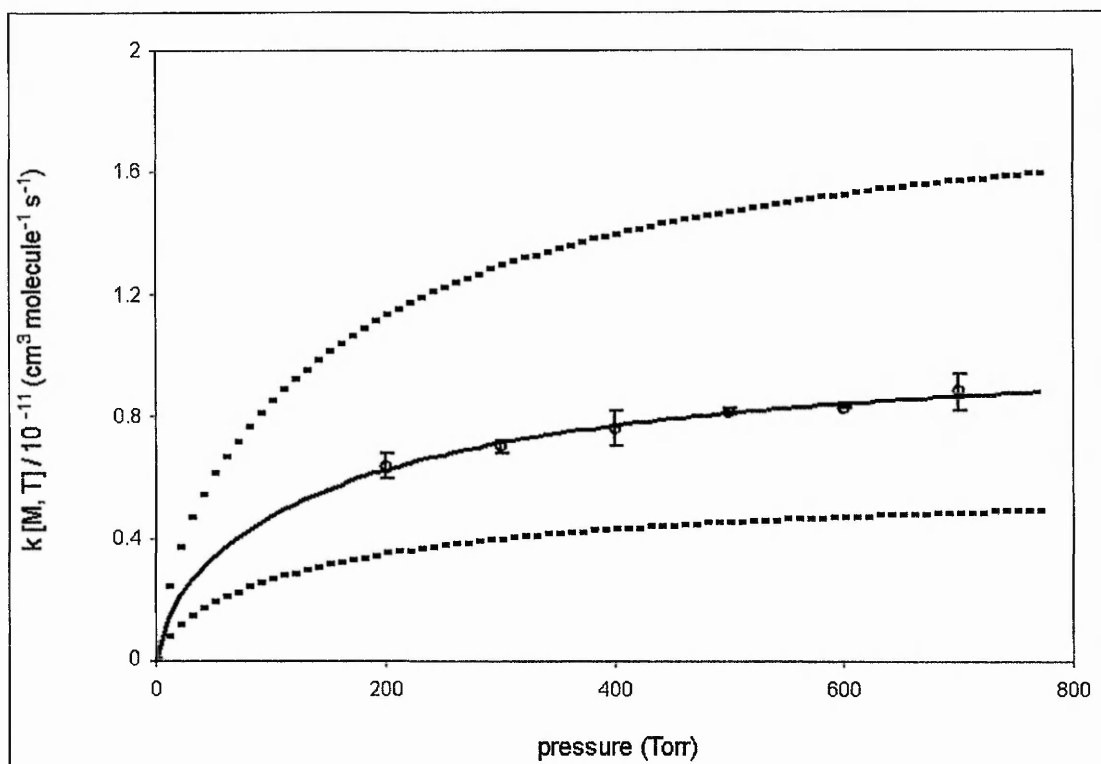
Figure 5.12: The pressure dependence of the rate coefficient as observed in this study at 223 K (○) data. The pressure dependence suggested by DeMore *et al.,* (1997) is also shown for comparison with a solid line. The dashed lines represent the upper and lower limits in k[M,T] as associated with the quoted errors in the values of n and m.

5.7 Product Studies

In order to assess the mass balance of reaction (5.10) product studies were performed at all temperatures and pressures. Figure 5.13 shows a mass spectrum (from $m/z = 2$ to $m/z = 200$) obtained using $[CH_3O_2]_0 = 1.02 \times 10^{12}$ molecule cm^{-3} and $[NO_2]_0 = 1.87 \times 10^{13}$ molecule cm^{-3} for a contact time of 0.048 ms. Under all conditions studied, even at the longest contact times, no other peaks were observed apart from SF_6^-, $SF_5^- NO_2^-$ or FO_2^-. The absence of any extra peaks suggests that the ionisation scheme used cannot detect $CH_3O_2NO_2$. Such an observation is in agreement with previous studies that have shown that the use of SF_6^- will not undergo ion-molecule reactions with similar alkyl nitrate species (Bardwell *et al.*, 2003).
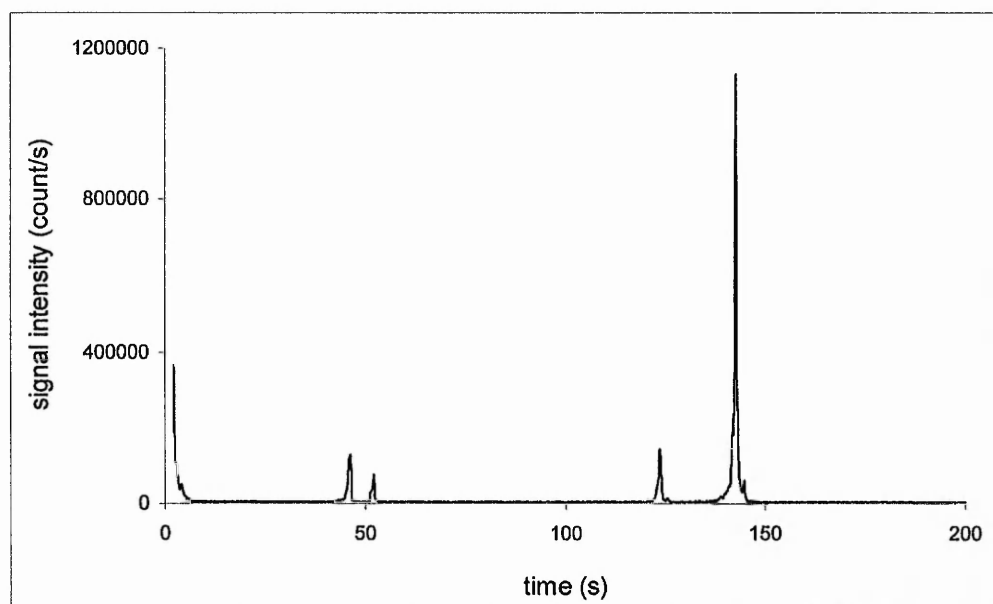
Figure 5.13: Spectral scan obtained during the product study experiments.

5.8 Conclusion

The data presented in this thesis indicates that reaction (5.11) does have the pressure dependence and negative temperature dependence suggested by previous studies. The results reported here represent an extension in the range of temperatures over which reaction (5.11) has been studied experimentally. In fact, our experiments appear to be the first ones conducted at a temperature below 253 K. Our results are in good agreement with previous higher temperature measurements extrapolated to 230 K. Hence, we believe that the rate coefficient of reaction (5.11) can be predicted reliably from the expression recommended by DeMore *et al.* for temperatures and pressures representative of the upper troposphere and lower stratosphere.

References

Adachi, H.; Basco, N., *Int. J. Chem. Kinet.*, 1980, **7**, 1

Bahta, A.; Simonaitis, R.; Heicklen, J., *J. Am. Chem. Soc.*, 1982, **86**, 1849

Bardwell, M.W.; Bacak, A.; Raventos, M.T.; Sanchez-Reyna, G.; Shallcross, D.E.; Percival, C.J., *Phys. Chem. Chem. Phys.*, 2003, **5**, 2381

Borrell, P.; Cobos C. J.; Luther, K., *J. Phys. Chem.*, 1988, **92**, 4377

Bridier, I.; Lesclaux, R.; Veyret, B., *Chem. Phys. Lett.*, 1992, **191**, 259

Cox, R.A.; Tyndall, G.S., *Chem. Phys. Lett.*, 1979, **65**, 357

Cox, R.A.; Tyndall, G.S., *J. Chem. Soc. Faraday Trans.*, 1980, **76**, 153

DeMore, W.B.; Sander, S.P.; Golden, D.M.; Hampson, R.F.; Kurylo, M.J.; Howard, C.J.; Ravishankara, A.R.; Kolb, C.E.; Molina, M.J., *JPL Publication 97-4*, 1997, 1

Destriau, M.; Troe, J., *Int. J. Chem. Kinet.*, 1990, **22**, 915

Finlayson-Pitts, B.J.; Pitts, J.N., *Atmospheric Chemistry*, John-Wiley and Sons, New York, 1986

Forst, W.; Caralp, F., *J. Phys. Chem.*, 1992, **96**, 6291

Lary, D.J.; Shallcross, D.E., *J. Geophys. Res. Lett.*, 2000, **105**, 19771

Lightfoot, P.D.; Cox, R.A.; Crowley, J.N.; Destriau, M.; Hayman, G.D.; Jenkin, M.E.; Moortgat, G.K.; Zabel, F., *Atmos. Environ.*, 1992, **26**, 1805

Niki, H.; Maker, P. D.; Savage, C. M.; Breitenbach, L. P., *Chem. Phys. Lett.*, 1980, **73**, 43

Patrick, R.; Golden, D.M., *Int. J. Chem. Kinet.*, 1983, **15**, 1189

Ravishankara, A.R.; Eisele, F.L.; Wine, P.H., *J. Chem. Phys.*, 1980, **73**, 3743

Sander, S.P.; Watson, R.T., *J. Phys. Chem.*, 1980, **84**, 1664

Seeley, J.V.; Jayne, J.T.; Molina, M.J., *Int. J. Chem. Kinet.*, 1993, **25**, 571

Simonaitis, R.; Heicklen, J, *J. Phys. Chem.*, 1974, **78**, 2417

Spicer, C.W.; Villa, A.; Wiebe, H.A.; Heicklen, J., *J. Am. Chem. Soc.*, 1973, **95**, 13

Wallington, T.J.; Nielsen, O.J.; Sehested, K., *Chem. Phys. Lett.*, 1999, **313**, 456

Wayne, R. P., *Chemistry of Atmospheres*, **3**[rd] edn., Oxford University Press, Oxford, 2000

Zabel, F.; Reimer, A.; Becker, K.H.; Fink, E.H. *J. Am. Chem. Soc.*, 1989, **93**, 5500

Chapter 6

Conclusions and Future Work

6.1 Chapter 3

Our kinetic findings on the reaction of HO_2 with NO [reaction (3.6)] are in good agreement with previous studies (Seeley *et al.*, 1996; Howard, 1979) in that we observed strong negative temperature dependence. The work presented in this thesis represents the first time that reaction (3.6) was studied at temperature below 210 K and our results are in excellent agreement with extrapolations to 193 K based on previous higher temperature measurements. Furthermore the results presented in chapter three highlights the impressive sensitivity of the TF-CIMS system; the estimated sensitivity for HO_2 was 1×10^7 molecules cm^{-3}. The utilisation of the CIMS detection technique enabled reaction (3.6) to be studied under with very low radical concentrations, typically 10^9 molecules cm^{-3}, thus minimising secondary radical chemistry. Furthermore, the research highlighted the selectivity of the CIMS detection technique, in that the CIMS system enables the reaction products to be monitored a function of contact time. OH radical formation was quantified; the sensitivity for OH was detected to be 4×10^7 molecules cm^{-3}, thus enabling the mass balance of reaction 3.6 to be assessed over the temperature and pressure range studied.

The negative temperature dependence of the rate coefficient for reaction (3.6) suggests that reaction proceeds through the formation of an energised intermediate $[HO_2NO]^*$.

Over the temperature range studied, the rate coefficient for reaction (3.6) was found to be invariant with pressure. In conjunction with product studies and theoretical calculations, our results suggest that the $[HO_2NO]^*$ intermediate is too short lived to be affected by collisions.

6.2 Chapter 4

The work presented in chapter 4 once again highlights the benefits of the use of turbulent flow technique for the study of atmospherically important reactions. In fact, it was the first study of the reaction of HO_2 with NO_2 (reaction 4.1) under UTLS conditions and the first time that radical reaction had been studied over such a large pressure range using the flow tube technique. All previous data studied the reaction using large initial $[HO_2]$ of $1 - 8 \times 10^{13}$ molecule cm^{-3} and thus the data had to be corrected for the self reaction of HO_2. The use of the TF-CIMS system enables the reaction to be studied with $[HO_2]_0 = 1 - 10 \times 10^9$ molecules cm^{-3} thus enabling the reaction to be asses directly without the use of kinetic modelling for the first time. Our results indicate that reaction (4.1) has significant pressure dependence, as suggested by previous studies (e.g. Christensen *et al.*, 2004). Our results are in excellent agreement with previous room temperature determinations of the rate coefficient, providing confidence in the TF-CIMS technique. The results presented in this chapter represent an extension in the range of temperatures over which reaction (4.1) has been studied experimentally. However, our results display significantly reduced temperature dependence with extrapolations to 200 K based on previous higher temperature

measurements extrapolated to 200 K. The pressure range over which reaction (4.1) has been studied was too narrow to enable an accurate parameterisation of the rate data using Troe type analysis. As pointed out by Kurylo and Ouellette (1986) corrections to the observed HO_2 time profiles were as high as 25% at room temperature. Considering that the HO_2 self-reaction displays negative temperature dependence the correction needed increases for the low temperature evaluations reported previously. However, additional studies over a wider range of pressures are required in order to resolve the discrepancies in the temperature dependence of the rate coefficients for reaction 4.1.

6.3 Chapter 5

The data presented in this chapter indicates that reaction (5.11) does have the pressure dependence and negative temperature dependence suggested by previous studies. The results reported here represent an extension in the range of temperatures over which reaction (5.11) has been studied experimentally. In fact, our experiments appear to be the first ones conducted at a temperature below 253 K. Our results are in good agreement with previous higher temperature measurements extrapolated to 230 K. Hence, we believe that the rate coefficient of reaction (5.11) can be predicted reliably from the expression recommended by DeMore *et al.* for temperatures and pressures representative of the upper troposphere and lower stratosphere.

6.4 Future Work

One of the most important characteristics of the TF-CIMS system is the sensitivity, which is already well ahead of other experimental systems that are employed for reaction kinetic studies in laboratories, and its selectivity. The results presented in this thesis show that it is possible to develop ionisation schemes that enable the detection of both radical and stable species. In particular the results of this work indicate that it is possible to selectively detect peroxy radicals in the ppt(v) range.

The concentrations and distribution of tropospheric ozone have important ramifications for human and plant health, and for radiative forcing. It is known that peroxy radicals are important mediators in both the production and the destruction of tropospheric ozone. Direct selective quantitative measurements of a range of organic peroxy radicals lies at the heart of understanding the photochemical production, destruction and modulation of ozone. However, currently there is no analytical device that can directly measure in real–time speciated peroxy radicals. Recent studies (Green *et al.,* 2002) reported that ambient concentrations of methyl peroxy radicals at ground level. According to PERCA measurements concentration of CH_3O_2 in ambient atmosphere is around 10^8 molecules cm^{-3}. Considering that the sensitivity of the TF-CIMS is of the order of 10^7 molecule cm^{-3} there is little doubt that the technique can be developed into analytical tool for the measurement of speciated peroxy radicals in ambient atmosphere.